7-1-2012

A computational study of the effects of adherent leukocytes on secondary recruitment

Dhananjay Subramaniam

A computational study of the effects of adherent leukocytes on secondary recruitment

by

Dhananjay Radhakrishnan Subramaniam

A Thesis Submitted in Partial Fulfillment of the Requirements for the Degree of Master of Science in Mechanical Engineering

Supervised by

Dr. David J. Gee
Department of Mechanical Engineering
Kate Gleason College of Engineering
Rochester Institute of Technology
Rochester, NY
July 2012

Approved By:

Dr. David J. Gee
Department of Mechanical Engineering _____
(Thesis Advisor)

Dr. Risa J. Robinson
Department of Mechanical Engineering _____
(Committee Member)

Dr. Kathleen A. Lamkin-Kennard
Department of Mechanical Engineering _____
(Committee Member)

Dr. Alan H. Nye
Department of Mechanical Engineering _____
(Departmental Representative)

To my family

Acknowledgements

Firstly, I would like to thank my advisor, Dr. David J. Gee for his valuable support and encouragement throughout my graduate study. His passion and dedication towards inflammation modeling has fueled my interest and appreciation towards the field of computational biology. I would like to convey my gratitude to him for his excellent guidance and this wonderful opportunity to conduct research in an interdisciplinary field of study.

Secondly, I would like to thank Dr. Sangtae Kim (Executive Director - Morgridge Institute for Research) for several discussions concerning micro-hydrodynamics, Dr. Michael R. King (Associate Professor – Biomedical Engineering, Cornell University) for his valuable suggestions related to adhesive interactions, Dr. Edward C. Hensel, Dr. Risa J. Robinson, Dr. Kathleen A. Lamkin-Kennard for backing this study, Diane Selleck, Diedra Livingston, Venessa Mitchell and Jill Ehmann of the ME Department for their help and support throughout my studies.

Finally, I would like to thank my parents Dr. S. Radhakrishnan and Ananthalakshmi Radhakrishnan, my aunt Dr. Kumari Santosh, elder sister Kirthi and cousins Sadashiv, Shrihari and Vidya for their constant support and encouragement, which has kept me cheerful and motivated during my tenure as a graduate student at RIT.

Partial support from the Office of Vice President for Research (#15651) and computational support from Research Computing at RIT are also acknowledged.

Abstract

Leukocyte rolling is known to be mediated by the selectin family of adhesion molecules and their corresponding ligands and is characterized by the formation and breakage of receptor-ligand bonds. Selectin mediated rolling is associated with the initial stages of the leukocyte adhesion cascade (LAC) in which the cell passes through several stages including chemo-attraction, rolling adhesion, tight adhesion and transmigration before moving out of the circulatory system towards the site of injury. This thesis studies the initial stages of the leukocyte adhesion cascade through a direct numerical simulation based on boundary element techniques. Besides, cell deformation during rolling is believed to further enhance rolling interactions. This feature is accounted for by implementing a constitutive model that qualitatively represents the morphology of white blood cells in the early stages of selectin mediated rolling. This research describes the contribution of contact mechanics towards modulation in the contact area for cell substrate interactions. The results predict that compliant cells could roll slower (~ 25%) as compared to their stiffer counterparts. The effect of variations in cell size and bond compression on the decrease in the translational velocity as well as the inherent noisiness in the translational velocity is investigated.

The latter part of this thesis attempts to quantify hydrodynamic recruitment of leukocytes with a view to providing insights into cell trafficking in physiological phenomena such as the homing of stem cells towards bone marrow. In vivo experimental data of leukocyte accumulations during exposure to Zymosan-Activated Serum (ZAS) in rabbits and immune response in hamster cheek pouches appears to reinforce this hypothesis. The influence of deformation on the attachment of free-stream cells through collisions and near wall interactions with adherent cells is numerically investigated. The trajectories of free-stream cells colliding

with deformed adherent cells are computed through a series of glancing collisions in order to study the influence of cell shape on secondary recruitment.

Table of Contents

List of Figures

List of Tables

Glossary

$\boldsymbol{x}, \boldsymbol{X}, \boldsymbol{X}^*$	integration variable, source point, image point
$G_{ij}(\boldsymbol{x}, \boldsymbol{X})$	Stokeslet / Kelvinlet
$\Sigma_{ijk}(\boldsymbol{x}, \boldsymbol{X})$	associated stress tensor
$K_{ij}(\boldsymbol{x}, \boldsymbol{X})$	double layer
$K^*_{ij}(\boldsymbol{x}, \boldsymbol{X})$	adjoint double layer
p	pressure
$\boldsymbol{u}$	displacement vector
$\boldsymbol{v}$	velocity vector
$\boldsymbol{t}$	surface traction
$\boldsymbol{n}$	outward normal
a	particle radius / length of semi-major axis (for spheroids)
a_s	contact radius
$\boldsymbol{F}$,F_o	force vector, parameter in repulsive force model
$\boldsymbol{T}$	torque vector, absolute temperature
k_b	Boltzmann's constant
k_r^0, k_f^0	unstressed off/on rate
r^0	reactive compliance

Greek Symbols

μ	viscosity
$\dot{\gamma}$	shear rate
η	shear modulus
ν	Poisson's ratio
α	initial particle orientation
ε	particle-particle separation
κ	aspect ratio of spheroid
ω	contact angle
τ	parameter in repulsive force model/time period of Jeffrey's orbit
λ	equilibrium bond length/principal stretch ratio

1 INTRODUCTON

1.1 *Immune Response*

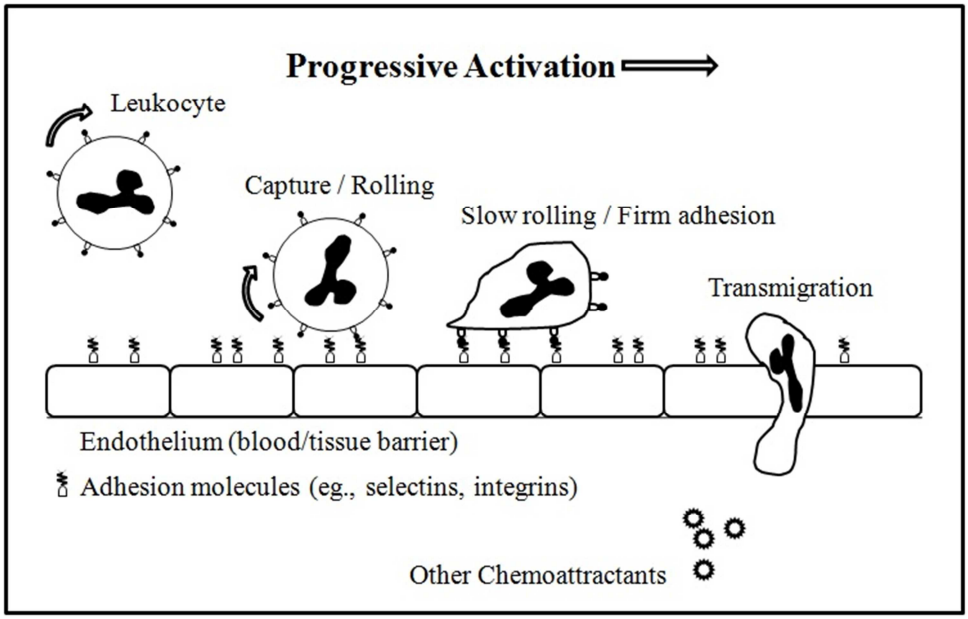

Fig. 1.1 The Leukocyte Adhesion Cascade.

The innate immune response involves the recruitment of white blood cells or leukocytes that move out of the circulatory system, towards the site of trauma. This process is known as leukocyte diapedesis and involves several stages including chemoattraction, rolling-adhesion, tight adhesion and transmigration (Ley et al. (2007)). Upon activation by inflammatory stimuli, macrophages release cytokines and prompt endothelial cells in the proximity of the infection site to express selectins. Leukocyte rolling is mediated by P- and E-Selectin (expressed on endothelial cells) and their corresponding ligands found on the tip of the leukocyte microvilli. Activated integrins bind tightly to receptors on endothelial cells and further decrease the cell's rolling velocity. Eventually, reorganization of the cytoskeleton causes it to spread over endothelial cells. The extension of pseudopodia enhances cell motility and enables the

leukocytes to pass through the endothelium and ultimately to the site of trauma (Fig. 1.1). The process is characterized by a progressive morphological change from a nearly spherical shape to a flat oblate spheroid. It is believed that deformation of rolling leukocytes enhances rolling interactions and plays a role in diapedesis (Gee and King (2010)).

Deficiencies in E- and P-Selectin can negate inflammatory response (Kunkel and Ley (1996)). Moreover, defective integrins impair the ability of leukocytes to stop and undergo diapedesis resulting in leukocyte adhesion deficiency (LAD) (Kinashi et al. (2004)).

1.2 *Mathematical Modeling of Blood Flow*

Blood consists of erythrocytes, leukocytes and thrombocytes suspended in viscous plasma. A milliliter of blood contains approximately 10^7 white blood cells. As indicated in Figure 1.2, these cells are composed of a nucleus, granules, cytoplasmic fluid, cytoskeleton, membrane and other organelles.

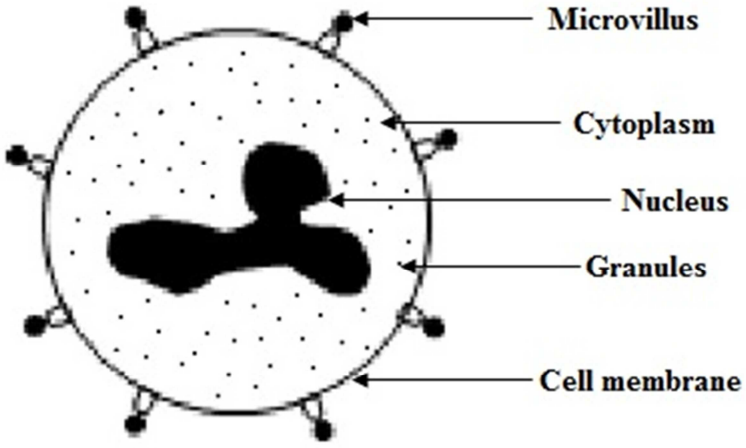

Fig. 1.2 Structure of neutrophils.

The space between the nucleus and cell-membrane is filled with cytoplasmic fluid that corresponds to nearly half the volume of the cell. While the membrane controls transport into and out of the cell, the granules play a role in lysis. The exterior surface of the membrane is covered with undulations (microvilli) which represent folds of excess membrane.

Figure 1.3 is a scanning electron micrograph which clearly illustrates the surface morphology of the leukocyte microvilli. P-Selectin ligands such as P-selectin glycoprotein

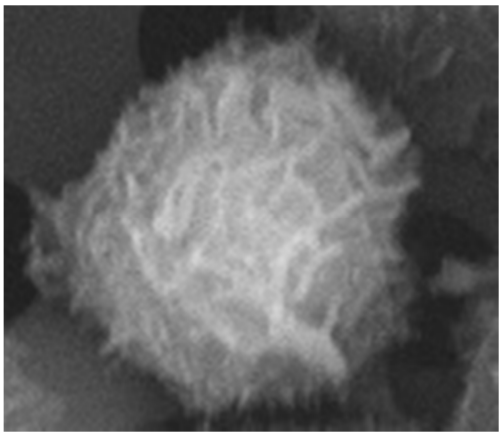

Fig. 1.3 Scanning Electron Micrograph (SEM) of a white blood cell (Courtesy: Dr. Thomas R. Gaborski (SiMPore Inc.)).

ligand-1 (PSGL-1) and L-Selectin are expressed on the tips of the microvilli and β2 integrin adhesion molecules such as Lymphocyte function-associated antigen 1 (LFA-1) and Macrophage-1 antigen (Mac-1) are preferentially located in the folds between successive microvilli.

A variety of computational techniques have evolved to solve problems involving immersed objects, following the pioneering work of Fröhlich and Sack (1946). Domain based methods including volume of fluid and the immersed boundary method (IBM) have been employed to simulate blood flow and have been coupled with finite element methods to model

cell deformation. However, such numerical schemes tend to be computationally expensive, since they necessitate a complete discretization of the flow domain. Besides, since the flow domain is confined by the bounding box, free-stream and rolling cell travels are limited. Moreover, simulations involving multiple cells required approximately 100 hours of CPU time (Jadhav et al. (2007), Hoskins et al. (2009)). The numerical strategy adopted in this thesis is based on boundary element techniques (BEM) that are ideal tools to solve problems involving suspensions. A 3D problem could be solved by surface discretization, since the problem dimensionality is reduced by one. Multi-particle simulations are thereby not as computationally intensive as the aforementioned domain based methods. For instance, King and Hammer (2001a) simulated an array of 14 adherent cells as opposed to 6 cells tested by Pappu et al. (2008), to estimate stable rolling of leukocytes. Furthermore, the cell travel is not limited by the size of the flow domain. Our method involves a range completion of the double layer and is known as the Completed Double Layer Boundary Integral Equation Method (CDL-BIEM) (Phan-Thien and Fan (1996), Phan-Thien et al. (1992)).

The origins of biological cell modeling can be traced back to the fundamental fluid dynamics problem of the deformation and dislodging of liquid drops. The complex nature of the leukocyte structure has generated considerable debate regarding the appropriate constitutive model. Lim et al. (2006) summarize several constitutive models proposed for living cells and discuss the advantages and limitations of each model. While Dong et al. (1999) modeled the cell as a Hookean ring surrounding an incompressible fluid, N'Dri et al. (2003) hypothesized that the cell could be modeled as a two-dimensional compound liquid drop. These ideas have been extended to 3D by Jadhav et al. (2005), Pappu and Bagchi (2008) and Pappu et al. (2008) via a Neo-Hookean elastic membrane that describes the non-linearity in material response.

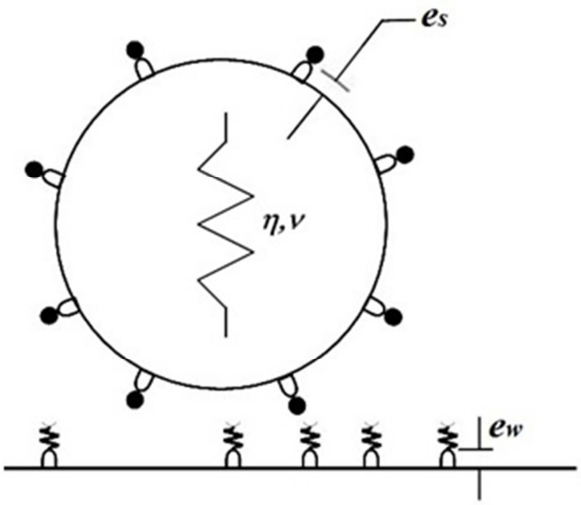

Fig. 1.4 Leukocyte modeled as a linear elastic solid.

The ability of leukocytes to undergo large deformations has also been modeled using compound viscoelastic drop models proposed by Khismatullin and Truskey (2012). The present study accounts for cell deformation by approximating the leukocyte as a Hookean solid with material parameters η, v_p (Fig. 1.4). This constitutive material model has been adopted previously by Wankhede et al. (2006) and suitably represents the small deformations associated with selectin-mediated rolling.

1.3 *Modeling Biochemistry*

Leukocyte rolling is characterized by the formation and breakage of receptor-ligand bonds, thereby making the behavior noisy. A probabilistic model formulated by Bell (1978) has been frequently employed in prior studies to model adhesive interactions between the cell and the substrate and the same is adopted in this work.

1.4 *Leukocyte Trafficking*

The necessity to quantify factors leading to cell trafficking arises from the accumulation of multiple cells to combat an infection. King and Hammer (2001a,b) described a “hydrodynamic recruitment” mechanism through which a firmly adherent rigid cell could recruit circulating cells. This has been supported by experimental evidence in cell-free assays (King et al. (2001)) and measurements of leukocyte capture *in vivo* using hamster cheek pouch (Lee and King (2006)). The multi-particle adhesive dynamics simulation was employed by King and Hammer (2001b) to model this phenomenon.

1.5 *Novelties in Proposed Research*

The role of contact forces for deformable leukocytes modeled has not been thoroughly investigated for tethered cells in static equilibrium (Smith et al. (1999)). Besides, Wankhede et al. (2006) assume a constant, time-independent contact area that arises from the wall reaction. Moreover, the existing bio-chemistry subroutine computes the number of receptors available for bond formation based on the proximity of the cell to the reactive substrate. The proposed formulation supplements this algorithm by including a dynamically evolving interfacial contact based on the theoretical model formulated by Hertz for an elastic sphere in contact with a rigid wall (Villaggio (1996)).

Secondary recruitment studies conducted by King and Hammer (2001b) comprise of spherical adherent or slowly rolling cells interacting with free-stream cells. However, in an actual physiological scenario, the free-stream leukocytes could potentially encounter adherent

cells at varying stages of the adhesion cascade. The influence of adherent cell deformation on cell accumulation is thereby accounted for and forms the central theme of this thesis.

Additionally, the integration of the adjoint double layer kernel over the singular element was achieved by subtracting the contribution of the corresponding integrals over the remaining elements. In this thesis, this integration is achieved by subtracting the integration of the double layer kernel over the non-singular elements as proposed by Phan-Thien and Fan (1996). Moreover, validation of the modified kernel functions for the half-space are investigated through a series of test cases involving non-spherical deformable inclusions in the proximity of the rigid substrate.

Unlike previous studies conducted with the multi-particle adhesive dynamics algorithm, that elucidated the ability of lubrication forces to induce cell deformation, the proposed work accounts for these short range non-adhesive interactions. From a programming viewpoint, the source code has been modified to input different meshes within the same simulation. The accuracy of the numerical scheme that was limited to 2^{nd} order Gaussian quadrature has been supplemented with the higher order quadrature schemes.

1.6 *Statement of Work*

"To simulate the deformations of rolling white-blood cells adhering to the endothelium in order to study effect of deformation on recruitment of WBC's to sites of injury or infection with a view to reduce the dependency on extensive experimentation."

1.7 *Thesis Objectives and Scope*

- The probabilistic bond-kinetics algorithm is appropriately modified to account for cell deformation and its effect is assessed on the rolling velocity of the cell.
- The hydrodynamic recruitment of free-stream leukocytes is investigated using the steady-state morphologies of deformed, adherent cells.
- The research only accounts for infinitesimal to moderate deformation of the leukocytes. Non-linear material response is beyond the scope of this thesis.
- Dynamic deformation and mobility simulations have been restricted to solitary cell rolling studies.
- This thesis addresses secondary recruitment through hydrodynamic interactions between adherent and free-stream leukocytes. Other modes of secondary recruitment stemming from binary interactions between free-stream WBCs or L-selectin mediated cell-cell adhesion are only briefly introduced.

Chapter 2 discusses the theoretical model including the numerical methodology, its implementation and results from several fundamental test cases. Short-range adhesive interactions such as electrostatic repulsion and lubrication are reported in Chapter 3. A formulation for computing the interfacial contact area stemming from cell compression and its subsequent effects on adhesive interactions is addressed through a series of rolling simulations for solitary cells of varying sizes and compliances in Chapter 4. Chapter 5 discusses the primary goal of this thesis: the phenomenon of secondary recruitment of free-stream leukocytes through binary interactions with firmly adherent deformed cells.

2 THEORETICAL MODEL

2.1 Problem Formulation

We use the parallel plate flow chamber to study cell-substrate adhesion. The flow domain is bounded by two infinite parallel plates (the lower surface of which is functionalized with adhesion molecules to simulate the inflamed endothelium) and the channel height is much greater than the radius of the rolling cell. The flow domain is representative of 2D flow and is a reasonable model for leukocytes in microcirculatory flow. The velocity profile near the surface is assumed to be linear and the motion of a leukocyte in the proximity of the substrate can be described as a treading motion for the inclusion in a semi-infinite shear flow, as indicated in Figure 2.1.

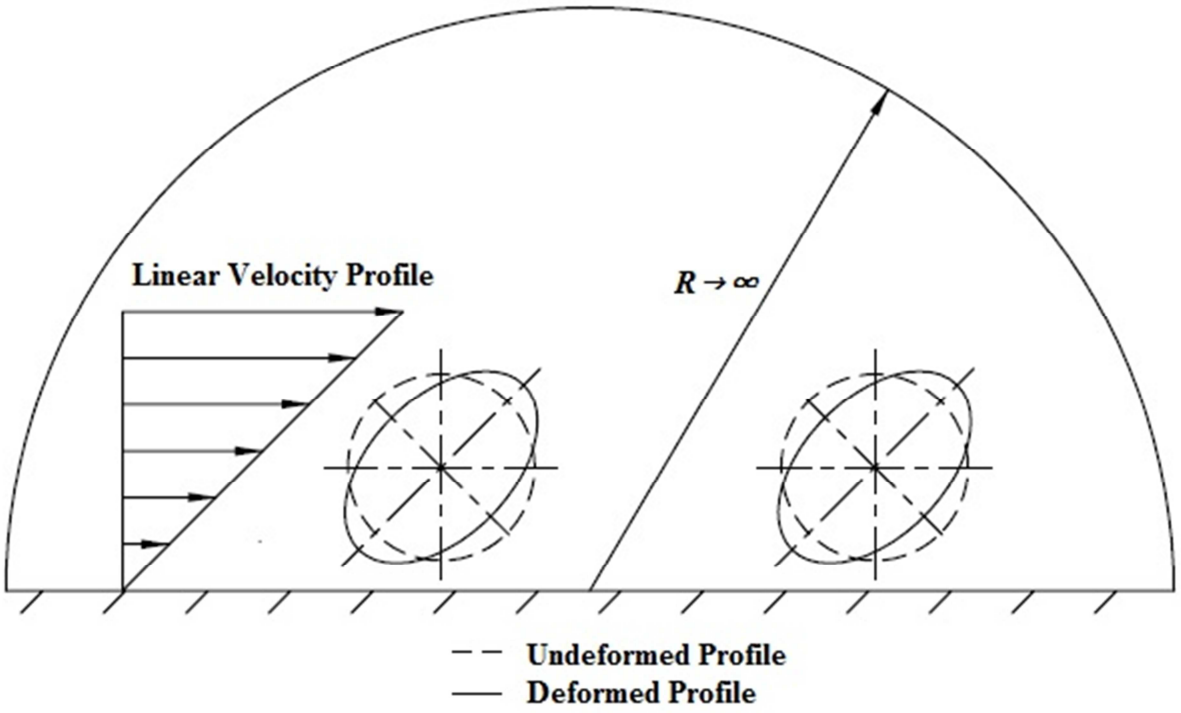

Fig. 2.1 Elastically deformable particles in wall bounded shear (Couette) flow.

Moreover, the Reynolds number associated with the flow in these experiments is << 1 and the Navier-Stokes equations reduce to Stokes equations.

$$\nabla \cdot \boldsymbol{v} = 0\,,\ -\nabla p + \mu \nabla^2 \boldsymbol{v} = \boldsymbol{0} \qquad (2.1)$$

where $\boldsymbol{v}$, p are velocity and pressure, respectively. No slip boundary conditions are enforced at the planar interface at all times. Particles immersed in the flow are subjected to stresses arising out of intercellular collisions, adhesive interactions and fluid shear. For a deformable particle, the deformation is computed by first determining the traction distribution over the cell surface. Small displacements in an isotropic, homogenous elastic solid are governed by Navier's equation,

$$\frac{1}{1-2\nu_{\boldsymbol{p}}} \nabla \nabla \cdot \boldsymbol{u} + \nabla^2 \boldsymbol{u} = \boldsymbol{0} \qquad (2.2)$$

where $\boldsymbol{u}$, ν_p are displacement and Poisson's ratio, respectively. The three problems of interest have been termed mobility (translation and rotation), exterior (surface traction), and interior (deformation). The following section discusses the formulation of boundary element techniques employed to solve these three problems.

2.2 Boundary Element Method

A. *Mobility Problem*

The CDL-BEM is employed to solve the mobility problem of the inclusion. The starting point is the integral representation of the Stokes equations, derived using the Lorentz reciprocal theorem.

$$v_j(\boldsymbol{X}) + \int_{S_p} n_k(\boldsymbol{x}) \Sigma_{\boldsymbol{ijk}}(\boldsymbol{x}, \boldsymbol{X}) v_i(\boldsymbol{x}) dS(\boldsymbol{x}) = \int_{S_p} G_{ij}(\boldsymbol{x}, \boldsymbol{X}) \sigma_{\boldsymbol{ki}}(\boldsymbol{x}) n_k(\boldsymbol{x}) dS(\boldsymbol{x})\,,\ \boldsymbol{X} \in D \qquad (2.3)$$

where G_{ij} (Oseen-Burger tensor or Stokeslet) is the i-component of velocity due to a point force acting at $\boldsymbol{X}$ in the j-direction, $\Sigma_{ijk}(\boldsymbol{x},\boldsymbol{X})$ is the associated stress, $S = \cup S_p$, where $p = 1,2\ldots M$ and M is the number of particles. Here, $\boldsymbol{n}$ represents the outward normal and $\boldsymbol{\sigma}$ is the fluid stress tensor given by

$$\boldsymbol{\sigma} = -p\boldsymbol{I} + \mu(\nabla \boldsymbol{v} + (\nabla \boldsymbol{v})^t) \qquad (2.4)$$

The integrals on the right and left hand side of Eq. (2.3) are known as the single and double layer potentials, respectively, in analogy with potential theory. Decoupling the mobility problem from the traction and displacement problems permits the mobility calculation of the particle as a rigid body (Phan-Thien and Fan (1996)). The velocity representation using only the single layer potential results in an ill-conditioned Fredholm integral equation of the first kind. This problem is circumvented by dropping the single layer term and expressing the velocity integral as a Fredholm integral equation of the second kind with an unknown surface density $\boldsymbol{\varphi}$,

$$v_j(\boldsymbol{\xi}) = \varphi_j(\boldsymbol{\xi}) + \int_{S_p} K_{ij}(\boldsymbol{x},\boldsymbol{\xi})\varphi_i(\boldsymbol{x})dS(\boldsymbol{x}),\ \boldsymbol{\xi} \in S_p \qquad (2.5)$$

where K_{ij} is the double layer kernel and is given by,

$$K_{ij}(\boldsymbol{x},\boldsymbol{\xi}) = 2n_k(\boldsymbol{x})\Sigma_{ijk}(\boldsymbol{x},\boldsymbol{\xi}) \qquad (2.6)$$

A factor of two is included in the above expression in order to achieve a spectral radius of unity. The eigenvalues Γ of the double-layer are real such that $|\Gamma| \leq 1$ (Phan-Thien and Tullock (1993)). For $\Gamma = -1$, there are six null solutions to the double layer kernel, each corresponding to a rigid body mode of the particle. Thereby, for every particle one needs to impose six linearly independent constraints in order to render a unique solution. Power and Miranda (1987)

recognized this and sought to complete the double-layer representation by using velocity fields of point forces and torques and associated them with the null solutions on the particle surface

$$F_l^p = \left\langle \boldsymbol{\varphi}^{(p,l)}, \boldsymbol{\varphi} \right\rangle \tag{2.7}$$

$$T_l^p = \left\langle \boldsymbol{\varphi}^{(p,l+3)}, \boldsymbol{\varphi} \right\rangle \tag{2.8}$$

where (l=1,2,3) represents translation, ((l+3)=4,5,6) represents rotation of particle p, and $\langle \cdot, \cdot \rangle$ denotes the natural inner product

$$\left\langle \boldsymbol{\varphi}^{(p,i)}, \boldsymbol{\varphi}^{(q,j)} \right\rangle = \delta_{pq}\delta_{ij} \tag{2.9}$$

The null solutions are normalized with respect to the inner product and are given by

$$\boldsymbol{\varphi}^{(p,l)} = \frac{\boldsymbol{e}_l}{\sqrt{S_p}} \tag{2.10}$$

$$\boldsymbol{\varphi}^{(p,l+3)} = \frac{1}{\sqrt{I_l}} \boldsymbol{e}_l \times \boldsymbol{\rho} \tag{2.11}$$

where $\{\boldsymbol{e}_l\}$ are the unit vectors along the $\boldsymbol{x}_l$ directions, $\boldsymbol{\rho} = \boldsymbol{\xi} - \boldsymbol{x}_c^{(p)}$ is the position vector from the center of S_p to a point $\boldsymbol{\xi}$ on the surface (i.e., $\boldsymbol{\xi} \in S_p$) and I_l are the normalized constraints expressed as

$$I_1 = \int_{S_p} (\rho_2^2 + \rho_3^2) dS \tag{2.12}$$

$$I_2 = \int_{S_p} (\rho_3^2 + \rho_1^2) dS \tag{2.13}$$

$$I_3 = \int_{S_p} (\rho_1^2 + \rho_2^2) dS \tag{2.14}$$

Equations (2.10)-(2.14) are applicable to spherical inclusions. A Gram-Schmidt orthonormalization technique is essential for non-spherical inclusions; previously incorporated in the formulation by Mody and King (2005) to simulate the mobility of oblate spheroids. The aforementioned procedure that maps the eigenvalue of -1 to zero without affecting the rest of the spectrum is known as the Wielandt's deflation scheme and will be employed in the exterior and interior problems as well. In order to ensure that the problem could be solved iteratively, the eigenvalue of +1 is also deflated by introducing orthonormalized eigenvectors $\boldsymbol{\psi}^p$, of the adjoint K^* such that

$$\boldsymbol{\psi}^{\boldsymbol{p}}(\xi) = \frac{\boldsymbol{n}}{\sqrt{S_p}}, \ \boldsymbol{\xi} \in S_p \qquad (2.15)$$

The final integral expression is given by

$$\varphi_j(\boldsymbol{\xi}) + \int_{S_p} K_{ij}(\boldsymbol{x},\boldsymbol{\xi})\varphi_i(\boldsymbol{x})dS(\boldsymbol{x}) + \varphi_{\mathrm{j}}^{(p,l)}(\boldsymbol{\xi})\left\langle \boldsymbol{\varphi}^{(p,l)}, \boldsymbol{\varphi} \right\rangle - \psi_{\mathrm{j}}^{(p)}(\boldsymbol{\xi})\left\langle \boldsymbol{\psi}^{(p)}, \boldsymbol{\varphi} \right\rangle = b_j(\boldsymbol{\xi}) - \frac{1}{2}\psi_j^{(p)}(\boldsymbol{\xi})\left\langle \boldsymbol{\psi}^{(p)}, \boldsymbol{b} \right\rangle$$

where

$$b_j(\boldsymbol{\xi}) = -v_j^{\infty}(\boldsymbol{\xi}) + \sum_{p=1}^{M}(F_i^{(p)} - \frac{1}{2}(T_i^{(p)} \times \nabla)_{\boldsymbol{i}})G_{ji}(\boldsymbol{\xi}, \boldsymbol{x}_c^p) \qquad (2.16)$$

Once $\boldsymbol{\varphi}$ is computed, the velocity is determined using the following expression

$$v_j(\boldsymbol{\xi}) = -\varphi_j^{(p,l)}(\boldsymbol{\xi})\left\langle \boldsymbol{\varphi}^{(p,l)}, \boldsymbol{\varphi} \right\rangle \qquad (2.17)$$

The Stokeslet must be supplemented with image and extra terms in order to account for the half space (Fig. 2.2) (Tran-Cong and Phan-Thien (1986), Phan-Thien et al. (1992)); (Appendix A). This method of reflections (Ainley et al. (2008), Blake (1971), Blake and Chwang (1974)) implies that the container surface does not require discretization.

B. *Exterior Problem*

The traction based Completed Adjoint Double Layer Boundary Element Method (CADL-BEM) (Phan-Thien and Fan (1995)) is adopted for the traction distribution on the cell surface. The single layer representation of the velocity field is:

$$v_j(\boldsymbol{X}) = v_j^{\infty} - \int_{S_p} G_{ij}(\boldsymbol{x}, \boldsymbol{X}) t_i(\boldsymbol{x}) dS(\boldsymbol{x}) \qquad (2.18)$$

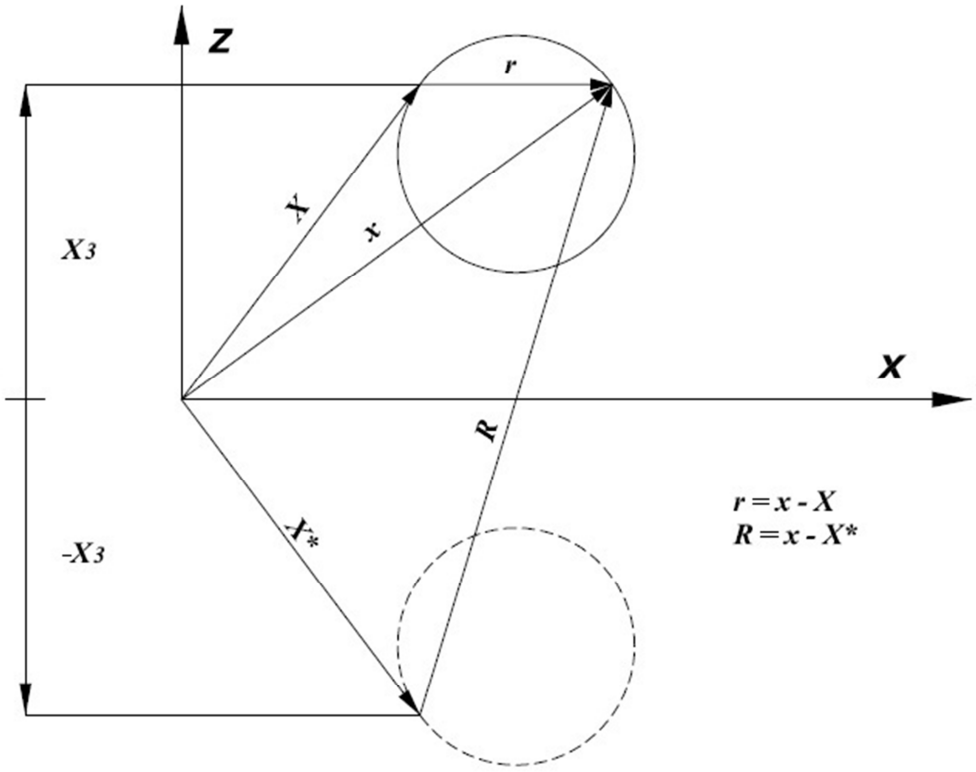

Fig. 2.2 Method of reflections to satisfy boundary conditions of no-slip and no-displacement boundary conditions at rigid substrate.

The traction at domain point $\boldsymbol{X}$, with unit normal $n_k(\boldsymbol{X})$, generated by the velocity field is

$$2t_j(\boldsymbol{X}) = 2t_j^{\infty}(\boldsymbol{X}) - \int_{S_p} K_{ij}^{*}(\boldsymbol{x}, \xi) t_i(\boldsymbol{x}) dS(\boldsymbol{x}) \quad (2.19)$$

where t_j^{∞} is the ambient traction and K_{ij}^{*} is the associated traction of G_{ij}, also known as the adjoint double layer kernel.

$$K_{ij}^{*}(\boldsymbol{x},\boldsymbol{X}) = -2n_k(\boldsymbol{X})\Sigma_{\boldsymbol{jik}}(\boldsymbol{x},\boldsymbol{X}) \qquad (2.20)$$

Phan-Thien and Tullock (1993) and Phan-Thien and Kim (1994) discuss the spectral properties of the double layer and its adjoint in depth. When the domain point $\boldsymbol{X}$ approaches the particle surface, the adjoint double layer suffers a jump discontinuity equivalent to $-t_j$. Hence, (2.19) can be re-arranged to give

$$t_j(\boldsymbol{\xi}) + \int_{S_p} K_{ij}^{*}(\boldsymbol{x},\boldsymbol{\xi}) t_i(\boldsymbol{x}) dS(\boldsymbol{x}) = 2t_j^{\infty}(\boldsymbol{\xi}) \ , \ \boldsymbol{\xi} \in S_p \qquad (2.21)$$

The spectral radius of the adjoint double layer is equal to unity. The eigenvalue $\Gamma = -1$ is associated with six eigenfunctions representing the rigid body motions of the particle (as discussed in the previous section). In order to generate a unique solution, six independent constraints in the form of forces and torques are specified on the particles. For spherical inclusions,

$$\sum_{l=1}^{3} \boldsymbol{\varphi}^{(p,l)} \left\langle \boldsymbol{\varphi}^{(p,l)}, \boldsymbol{t} \right\rangle = \frac{1}{S_p} \sum_{l=1}^{3} \boldsymbol{e}_l \boldsymbol{e}_l \cdot \int_{s_p} \boldsymbol{t} dS = \frac{1}{S_p} F^{(p)} \qquad (2.22)$$

$$\begin{aligned} \sum_{l=1}^{3} \varphi_j^{(p,l+3)} \left\langle \boldsymbol{\varphi}^{(p,l+3)}, \boldsymbol{t} \right\rangle &= \sum_{l=1}^{3} \varepsilon_{ijk} \frac{\delta_{il} r_k^{(p)}}{I_l^{(p)}} \int_{S_p} \boldsymbol{e}_l \times \boldsymbol{r}^{(p)} \cdot \boldsymbol{t} dS \\ &= \varepsilon_{jlk} \frac{T_l^{(p)}}{I_l^{(p)}} r_k^{(p)} \end{aligned} \qquad (2.23)$$

For non-spherical inclusions, the RHS of Eqs. (2.22-23) are linear combinations of the external forces and torques on the particle.

Equations (2.22) and (2.23) are linearly combined with Eq. (2.21) to give the final boundary integral equation for the traction problem:

$$t_j(\boldsymbol{\xi}) + \int_{S_p} K_{ij}^*(\boldsymbol{x},\boldsymbol{\xi}) t_i(\boldsymbol{x}) dS(\boldsymbol{x}) + \sum_{p,l} \boldsymbol{\varphi}^{(p,l)}(\boldsymbol{\xi}) \left\langle \boldsymbol{\varphi}^{(p,l)}, \boldsymbol{t} \right\rangle = b_j(\boldsymbol{\xi}) \quad (2.24)$$

where

$$b_j(\boldsymbol{\xi}) = 2t_j^{\infty} + \sum_p \left\{ \frac{1}{S_p} F^{(p)} + \varepsilon_{jlk} \frac{T_l^{(p)}}{I_l^{(p)}} r_k^{(p)} \right\} \qquad (2.25)$$

Unlike for the double layer, the Wielandt deflation scheme is employed to map only the eigenvalue of -1 to zero. As reported by Phan-Thien and Fan (1996), the deflation of the eigenvalue of +1 is not necessary for the exterior problem.

C. *Interior Problem*

Cell rolling deformations at low to intermediate stresses ($\leq$ 5 dyne/cm^2) are relatively small and can be approximated by a linear elastic model. Evans et al. (2005) showed that for compressive deformations of the order of hundreds of nanometers, neutrophil response is well approximated as a Hookean solid. Using Betti's reciprocal theorem, the integral equation for the displacement $\boldsymbol{u}$ is given by

$$u_j(\boldsymbol{\xi}) = -\int_{S_p} K_{ij}(\boldsymbol{x},\boldsymbol{\xi}) u_i(\boldsymbol{x}) dS(\boldsymbol{x}) + \int_{S_p} 2G_{ij}(\boldsymbol{x},\boldsymbol{\xi}) \sigma_{\boldsymbol{ki}}(\boldsymbol{x}) n_k(\boldsymbol{x}) dS(\boldsymbol{x}) \qquad (2.26)$$

where each particle is assumed to be Lyapunov smooth (i.e., having well-defined unit normal vector). $G_{ij}(\boldsymbol{x},\boldsymbol{\xi})$ gives the i-component of displacement due to a point force acting at $\boldsymbol{\xi}$ in the j-direction and is known as the Kelvinlet. Since the spectral radius of the elastic double layer is unity, the eigenvalue Γ = -1 has six independent eigenfunctions, each corresponding to a rigid body motion of the particle (i.e., $\boldsymbol{e_1}$, $\boldsymbol{e_2}$, $\boldsymbol{e_3}$, $\boldsymbol{e_1}$ x $\boldsymbol{r}$, $\boldsymbol{e_2}$ x $\boldsymbol{r}$, $\boldsymbol{e_3}$ x $\boldsymbol{r}$, where $\{\boldsymbol{e_k}\}$ is the Cartesian unit

vector and $\boldsymbol{r} = \boldsymbol{x} - \boldsymbol{x}^{(p)}$ is the position vector from the particle center $\boldsymbol{x}^{(p)}$). The corresponding orthonormalized eigenfunctions for a sphere are

$$\boldsymbol{\varphi}^{(p,k)} = \frac{\boldsymbol{e}_k}{\sqrt{S_p}} \quad (k = 1, 2, 3) \tag{2.27}$$

$$\boldsymbol{\varphi}^{(p,k+3)} = \frac{1}{\sqrt{I_k^p}} \boldsymbol{r}^p \times \boldsymbol{e}_k \tag{2.28}$$

where

$$I_k^p = \int_{S_p} \left[\boldsymbol{r}^p \cdot \boldsymbol{r}^p - (r_k{}^p)^2 \right] dS \tag{2.29}$$

The six linearly independent constraints imposed on the solution are of the form

$$\left\langle \boldsymbol{\varphi}^{(p,l)}, \boldsymbol{u} \right\rangle = 0 \quad l=1,2\ldots6 \tag{2.30}$$

and are linearly combined with Eq. (2.26) to give the final integral expression,

$$u_j(\boldsymbol{\xi}) + \int_{S_p} K_{ij}(\boldsymbol{x}, \boldsymbol{\xi}) u_i(\boldsymbol{x}) dS(\boldsymbol{x}) + \sum_{p,l} \boldsymbol{\varphi}^{(p,l)}(\boldsymbol{\xi}) \left\langle \boldsymbol{\varphi}^{(p,l)}, \boldsymbol{u} \right\rangle = \int_{S_p} 2G_{ij}(\boldsymbol{x}, \boldsymbol{\xi}) \sigma_{\boldsymbol{ki}}(\boldsymbol{x}) n_k(\boldsymbol{x}) dS(\boldsymbol{x}) \tag{2.31}$$

The traction solution from the exterior problem serves as an input to the right hand side of Eq. (2.31), using which the displacement is solved for iteratively. The Wielandt deflation maps the eigenvalue of -1 to zero, while retaining the rest of the spectrum. Moreover, unlike the mobility problem, deflation of the eigenvalue of +1 is not necessary for the interior problem (Phan-Thien and Fan (1996)).

2.3 Numerical Validation

The validity of the BEM formulation was determined through a series of simulations involving the translation and rotation of deformable spherical and spheroid inclusions in the proximity of the substrate. The surfaces of the particles are discretized using QUAD9 Lagrangian elements (Fig. 2.3).

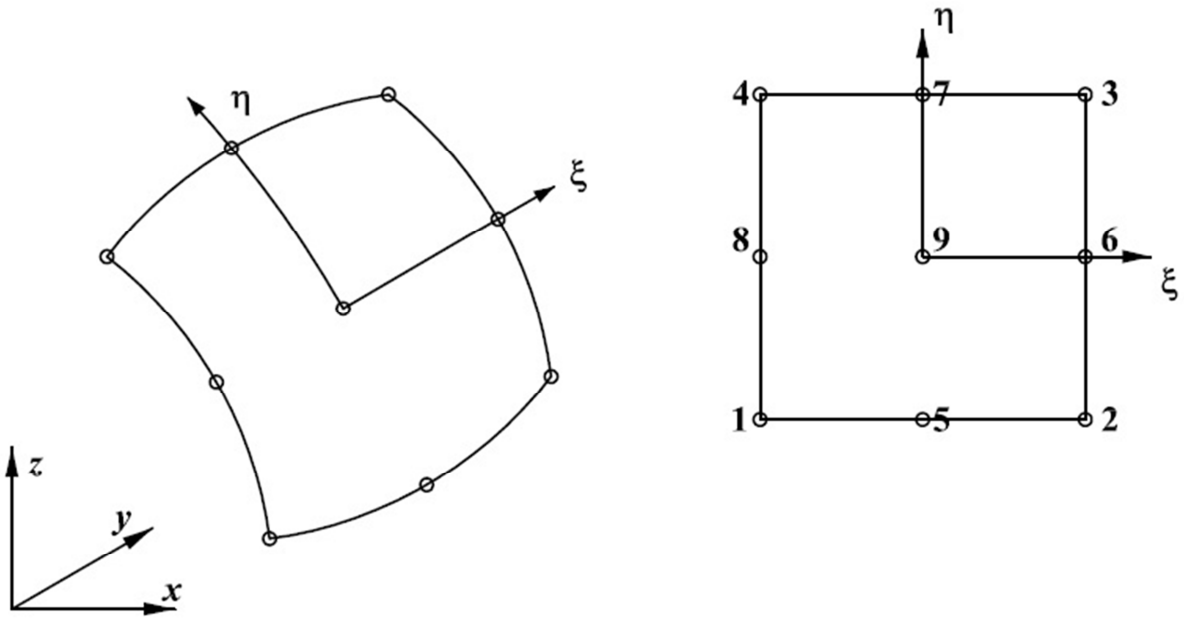

Fig. 2.3 QUAD9 Lagrangian element.

Super-parametric elements are employed where the unknown is assumed piece-wise constant. Numerical integration is performed using up to 3x3 Gaussian quadrature. The six faces of a cube are subdivided into 96 elements and projected onto the surface of a sphere (Fig. 2.4a). The sphere maybe compressed along an axis to generate oblate spheroids of several aspect ratios (Fig. 2.4b). The shear modulus η ranges from 0.5 – 23 Pa (Rosenbluth et al. (2006)), while a constant Poisson's ratio of 0.33 is maintained in all simulations. The positions of all the material points are advanced in each time step using Euler's integration rule. The source code is written in

double precision FORTRAN 95 and the output files post-processed in MATLAB. A maximum of 1000 iterations for solution convergence per unit time step is adopted with the tolerance being set at 10^{-4}. All simulations are performed on Sun X4600M2 servers with 2.3GHz AMD Quad Core processors at a time step size of 10^{-4} for a period of 1 s.

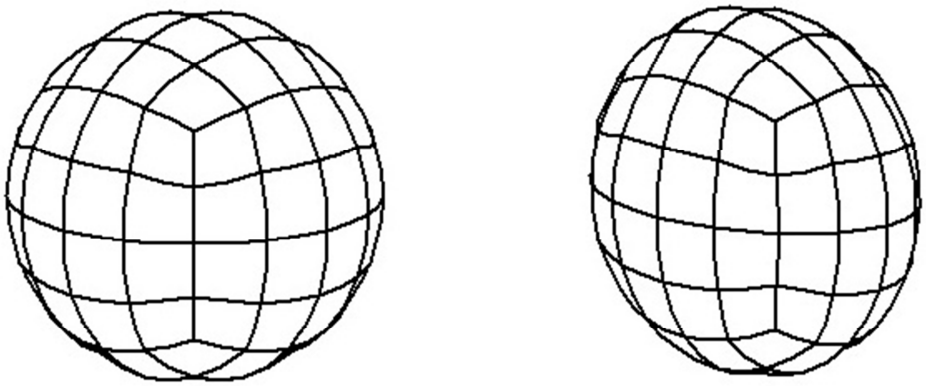

(a) **(b)**

Fig. 2.4 96 element discretization of (a) sphere (b) oblate spheroid.

A. EFFECT OF SUBSTRATE ON PARTICLE TRAJECTORIES

In a zero gravity field, micro-spheres almost move parallel to the wall without crossing the streamlines (Bretherton (1962), Goldman et al. (1967a,b)). Vis-à-vis, dense inclusions are found to sediment or drift towards the wall (Decuzzi and Ferrari (2006)). On the other hand non-spherical particles such as spheroids exhibit a more complicated behavior. The Stokes number of a particle *St* is expressed in terms of the Reynolds number *Re*, particle density ρ_g and density of the surrounding medium ρ as follows:

$$St = \frac{\rho_g}{\rho} Re \qquad (2.32)$$

The particle drift was found to increase with increasing *St* (Lee et al. (2009)). For the simulations

discussed in this section *Re*, *St* << 1 and the particle follows a periodic motion predicted analytically by Jeffery (1922). The variation in the centroidal position of the particle is plotted with respect to nondimensional time *t* that is defined as follows:

t = Simulation running time (s) / {Time step (s) x Frequency of data save}

Therefore for a running time of 1 s, a step size of 10^{-4} s and data saved every 10 time steps, the non-dimensional time is 1000. The same definition is adopted for all simulations described in current and subsequent chapters.

The trajectories of a neutrally buoyant and dense deformable spherical inclusion at shear rates of 100 and 200 s^{-1} are indicated in Figure 2.5. As can be seen, in the absence of gravity, the

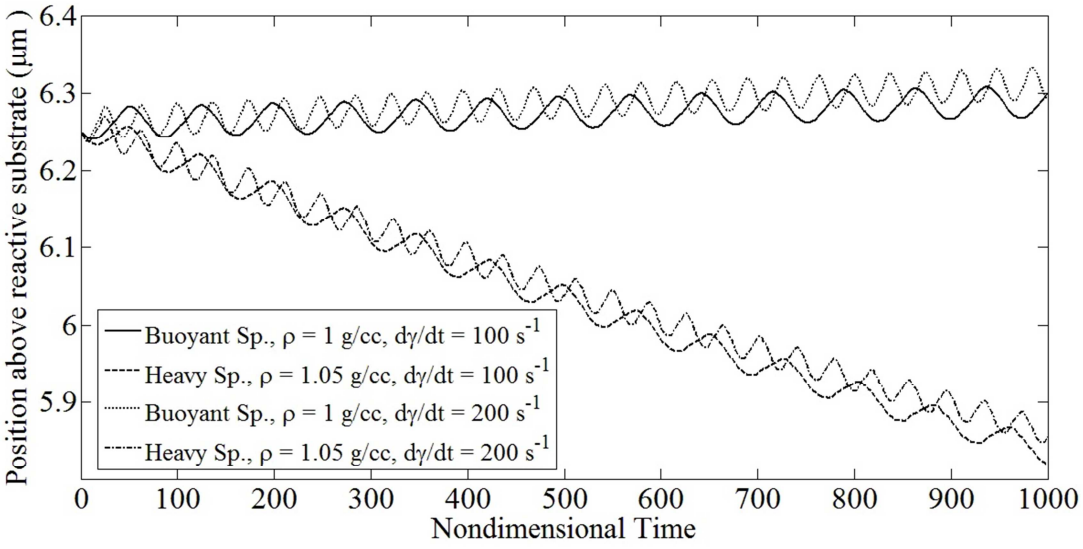

Fig. 2.5 Comparison between the trajectories of a buoyant and dense spherical inclusion (a = 5 μm, η = 1 Pa, v = 0.33, $\dot{\gamma}$ = 100, 200 s^{-1}).

inclusion appears to move almost parallel to the wall. On the other hand, dense inclusions drift towards the wall. Moreover, doubling the shear rate moderately alters the trajectories since the *Re* and *St* numbers only marginally increase. The particle trajectories for oblate spheroids with aspect ratios 0.75 and 0.5 are indicated in Figure 2.6-7.

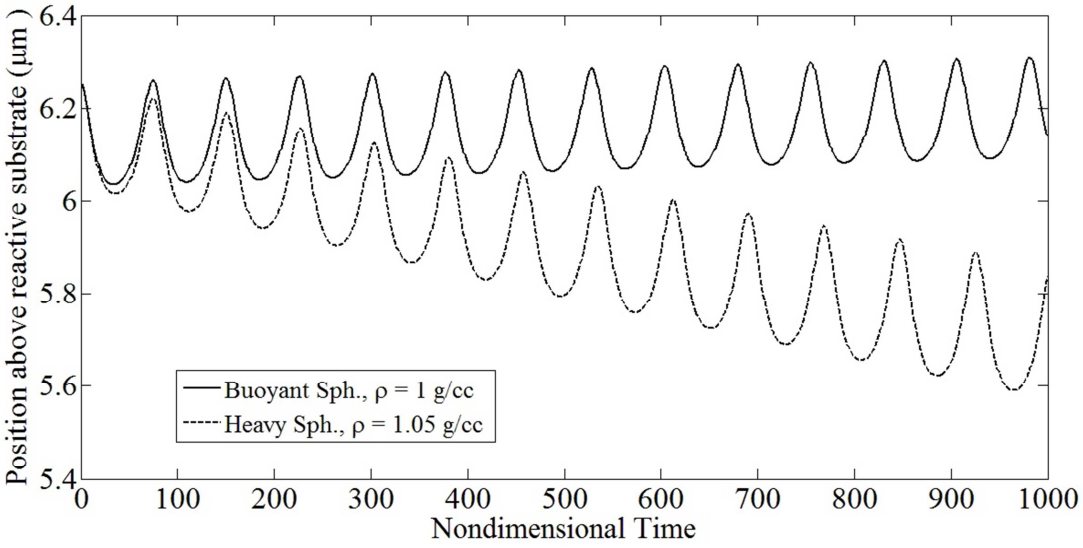

Fig. 2.6 Comparison between the trajectories of a buoyant and dense oblate spheroid inclusion (a = 5 μm, η = 1 Pa, ν = 0.33, α = π/2, κ = 0.75, $\dot{\gamma}$ = 100 s^{-1}).

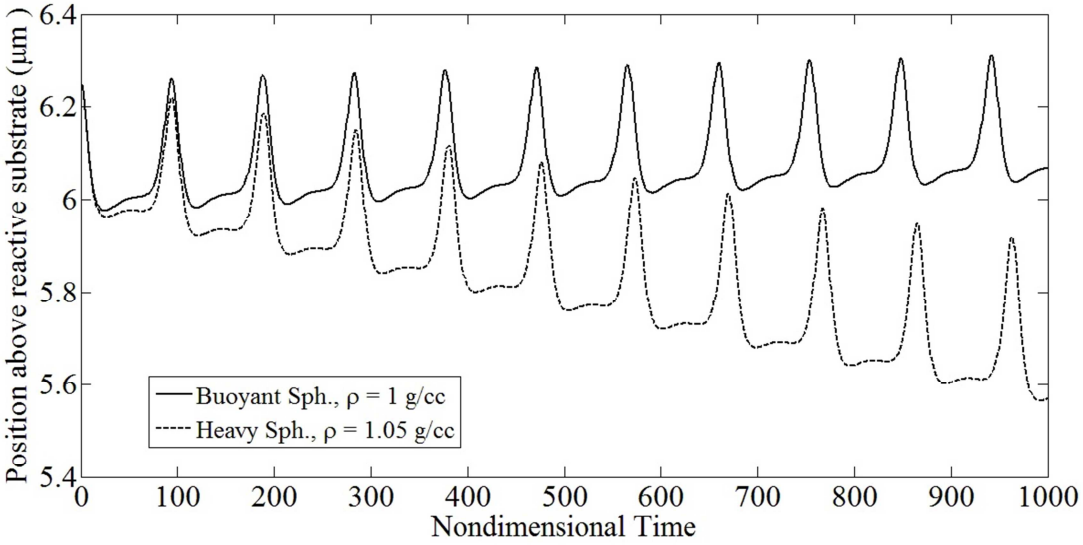

Fig. 2.7 Comparison between the trajectories of a buoyant and dense oblate spheroid inclusion (a = 5 μm, η = 1 Pa, ν = 0.33, α = π/2, κ = 0.5, $\dot{\gamma}$ = 100 s^{-1}).

The analytical expression for the time period τ for the Jeffrey's orbit of a spheroid inclusion with aspect ratio κ in an unbounded shear flow (shear rate $\dot{\gamma}$) is given by

$$\tau = \frac{2\pi}{\dot{\gamma}}\left(\kappa + \kappa^{-1}\right) \qquad (2.33)$$

For an oblate spheroid with $\kappa = 0.75$, $\tau \sim 13/\dot{\gamma}$ and for $\kappa = 0.5$, $\tau \sim 16/\dot{\gamma}$. The numerical values for these time periods are $\tau \sim 15/\dot{\gamma}$ for $\kappa = 0.75$ (Fig. 2.6), $\tau \sim 19/\dot{\gamma}$ for $\kappa = 0.5$ (Fig. 2.7) and represent a modified Jeffrey's orbit in a wall bounded shear flow (Mody and King (2005)). Figure 2.8 indicates that by doubling the shear rate, this time period is halved. The results for the mobility of both spherical and spheroid inclusions appear to be in good agreement with those reported by Lee et al. (2009).

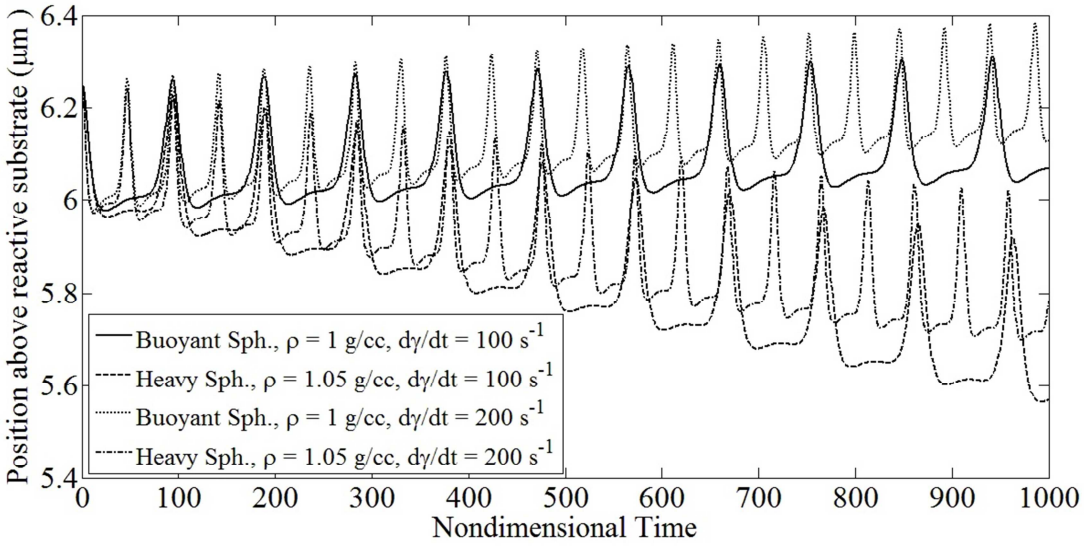

Fig. 2.8 Comparison between the trajectories of a buoyant and dense oblate spheroid inclusion (a = 5 μm, η = 1 Pa, ν = 0.33, $\alpha = \pi/2$, κ = 0.5, $\dot{\gamma}$ = 100, 200 s^{-1}).

B. SHAPE DYNAMICS

A deformable spherical inclusion placed in a linear shear flow deforms into an ellipsoidal shape (Fig. 2.9) in a manner similar to the shearing of a square block into a rhomboidal shape. Moreover, the aspect of ratio of the deformed profile is governed by the compliance of the material and the fluid shear rate. Steady state profiles for inclusions of varying shear moduli at different times are indicated in Figure 2.10.

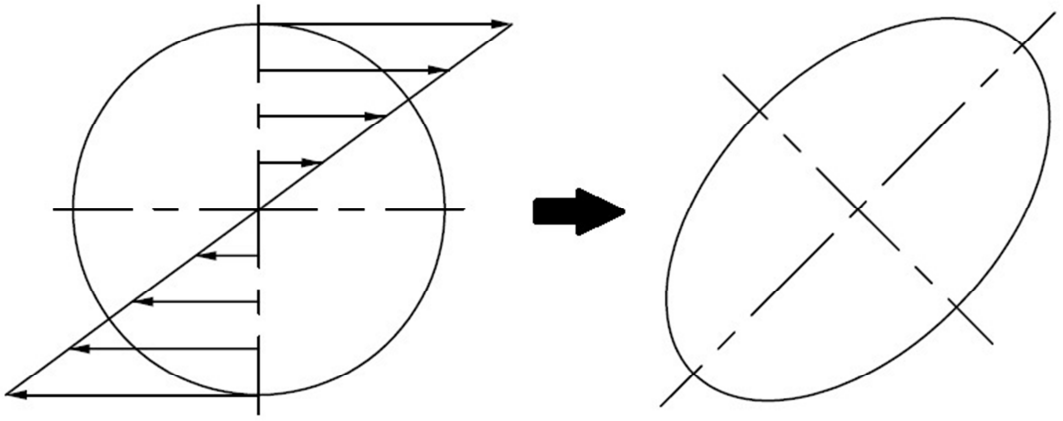

Fig. 2.9 Deformed shape of a spherical inclusion in a shear flow.

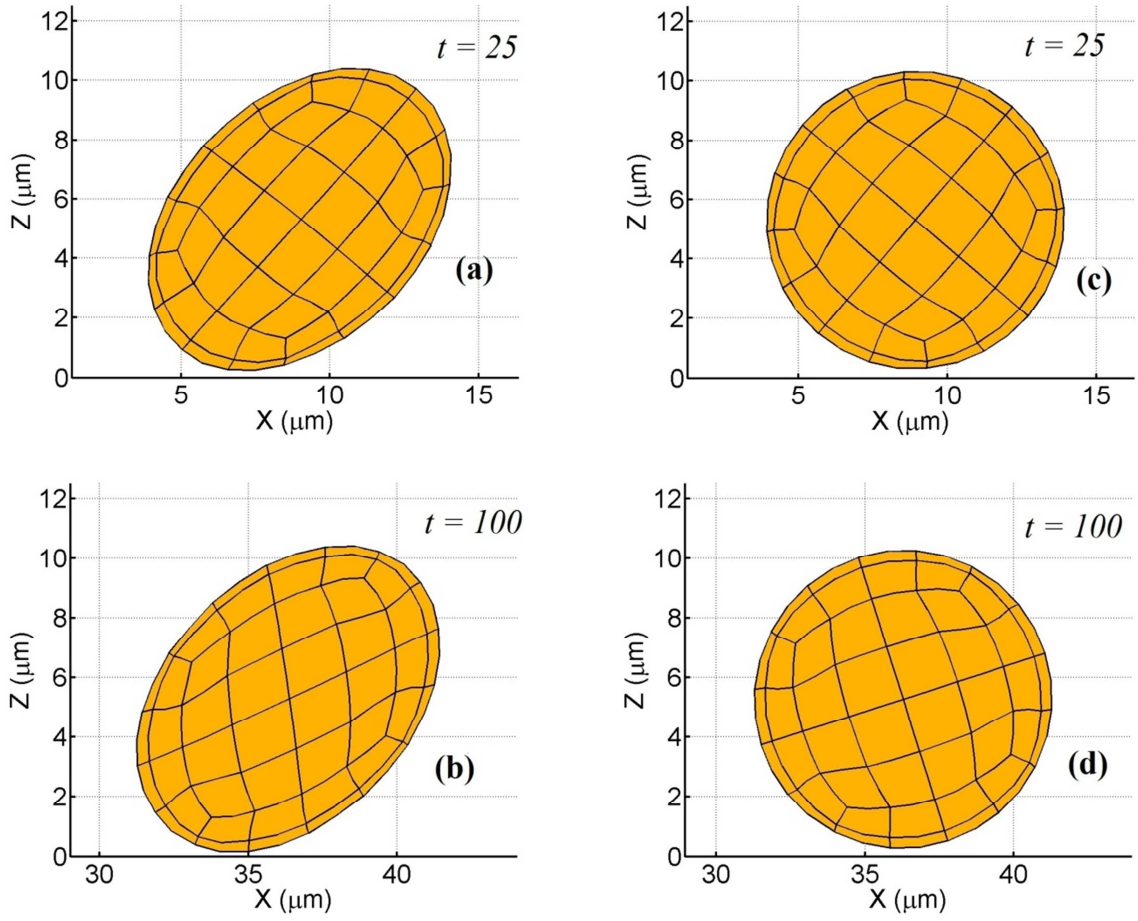

Fig. 2.10 Steady state shapes of a deformable spherical inclusion in the proximity of a rigid wall. For both simulations a = 5 μm, $\dot{\gamma}$ = 100 s^{-1}, v = 0.33: (a), (b) η = 0.5 Pa (c), (d) η = 23 Pa.

In Figure 2.10a-b, the shear modulus of the cell is relatively small compared to the fluid shear stresses and the sphere deforms into an ellipsoid. On the other hand, in Figure 2.10c-d, the shear modulus of the cell is much higher in comparison to the fluid shear stress. The inclusion thereby retains its spherical profile. The deformed shapes predicted here are in good agreement with those reported for Neo-hookean solids (Gao and Hu (2009)) and elastic capsules (Pozrikidis (1995)). Besides, the steady state shapes remain unchanged throughout the simulation (Fig. 2.11).

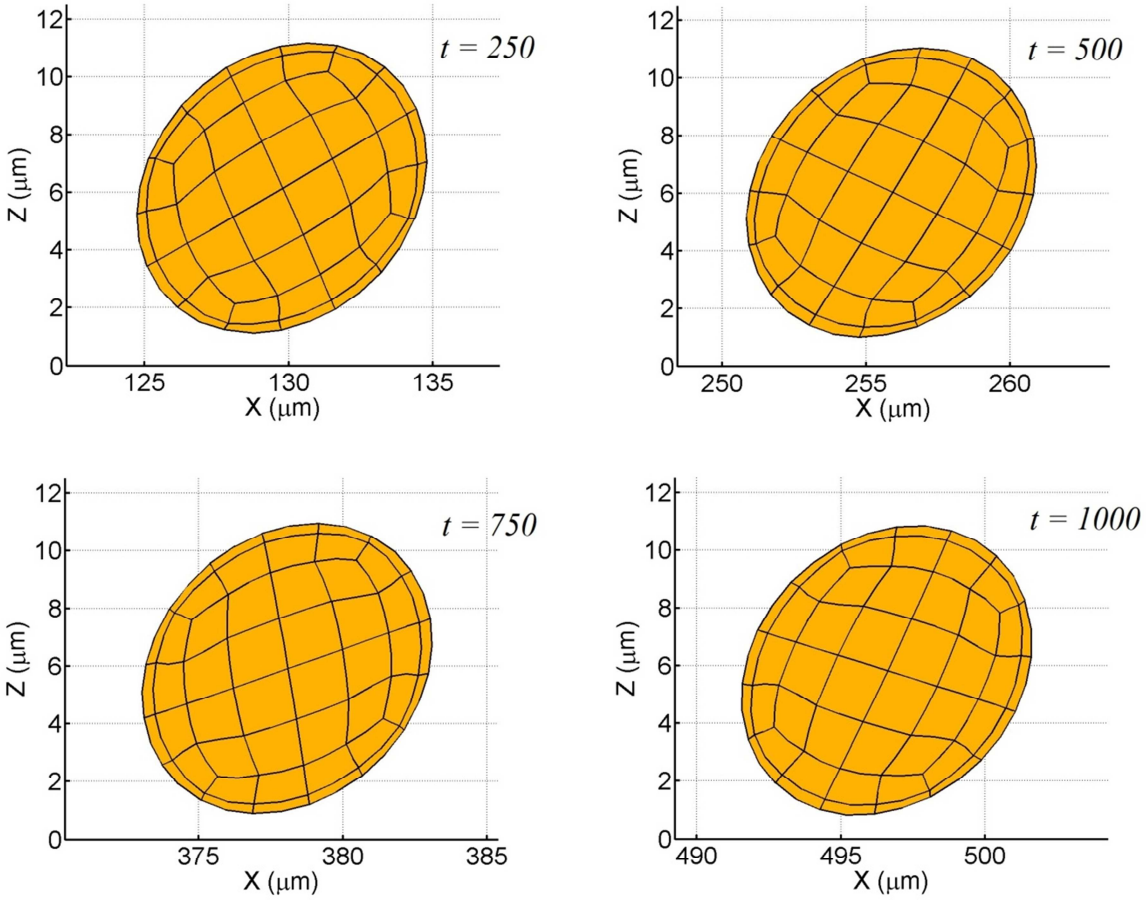

Fig. 2.11 Tank treading sequence of a deformable spherical inclusion in the proximity of a rigid wall (a = 5 μm, η = 1 Pa, v = 0.33, $\dot{\gamma}$ = 100 s^{-1}).

The particle exhibits a 'tank-treading' motion in which the particle appears to tumble in place and follows the elliptical profile of the deformed shape (Fig. 2.12). This behavior is characterized by

the inability of the major-axis of the deformed profile to complete a full revolution comprising of 2π radians with the minor axis taking its place in every cycle.

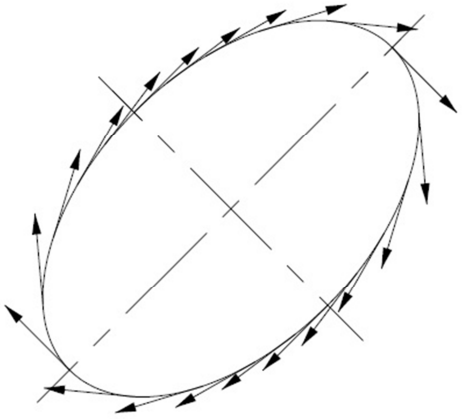

Fig. 2.12 Advection of material points along the perimeter of an ellipse.

The deformation of deformable, initially spheroid particles are similar in nature to their spherical counterparts, with the exception that the shape dynamics depends on the aspect ratio of these inclusions. Unlike spherical inclusions, a steady state shape is never achieved (Gao et al. (2012)). The ratio of the hydrodynamic to the elastic forces is expressed in terms of a dimensionless number known as the viscous number *Vi*.

$$Vi = \frac{\mu\dot{\gamma}}{\eta} \qquad (2.34)$$

Based on the dimensions of the spheroid prior to insertion into the shear flow and the viscous number, two forms of shape oscillations are observed – tumbling and trembling. The competition between the hydrodynamic shearing forces to deform the material lying along the maximum stretch axis ($\alpha = \pi/4$) and the elastic forces to restore the deformation generates a condition where the long axis in the deformed configuration does not always remain as the reference axis. When the hydrodynamic shearing forces are weak as compared to the restoring forces that tend to

preserve the shape, the inclusion is said to “tumble.” On the other hand, when the shearing forces are comparable in magnitude to the elastic forces, the particle shape deviates from its original configuration and is considered to “tremble.” This mode has been observed experimentally by Kantsler and Steinberg (2006) and is synonymous to the breathing mode identified by Misbah (2006) or the swinging mode described by Noguchi and Gompper (2007).

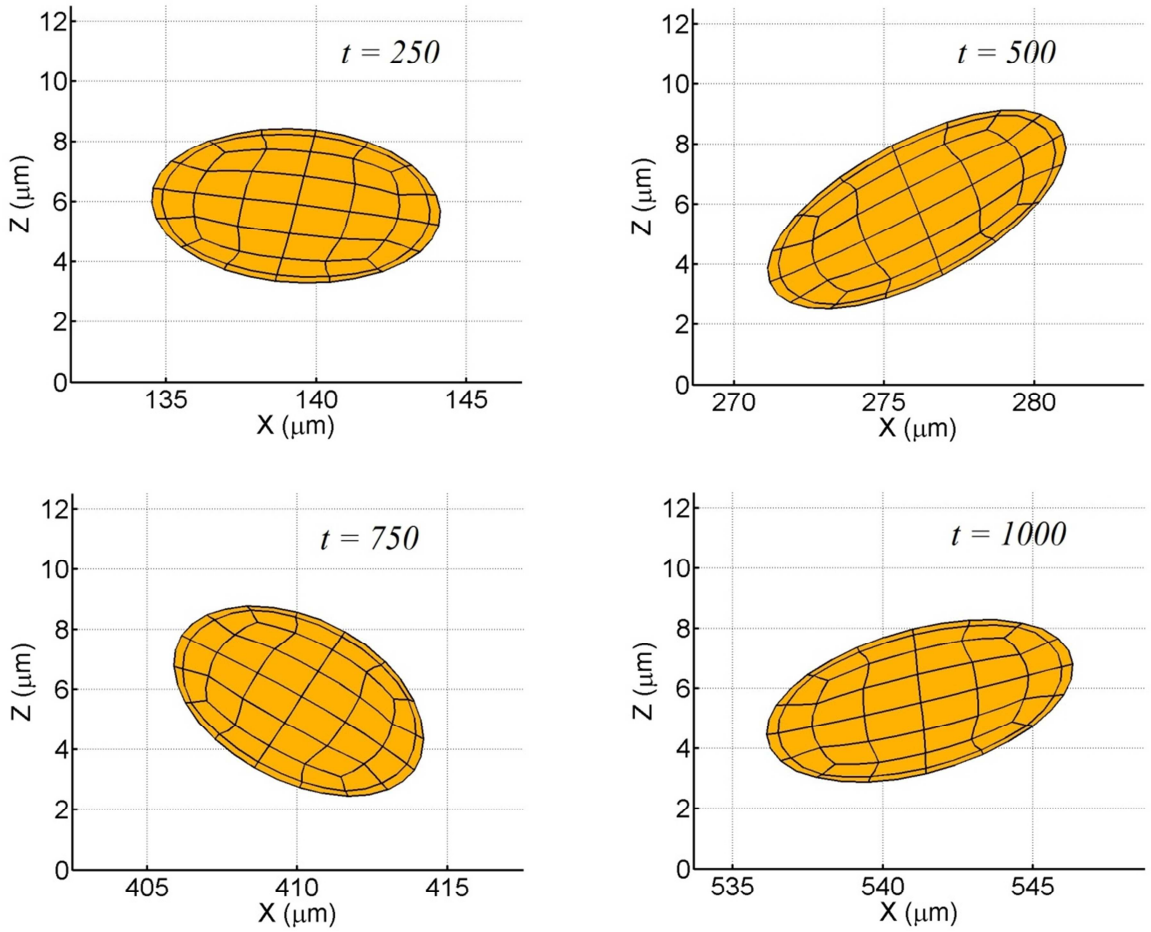

Fig. 2.13 Tumbling sequence of a deformable oblate spheroid in the proximity of a rigid wall (a = 5 μm, η = 1 Pa, ν = 0.33, $\alpha = \pi/2$, κ = 0.5, $\dot{\gamma}$ = 100 s^{-1}).

In the “tumbling” mode, the major axis makes a complete revolution as observed in Figure 2.13 for an oblate spheroid with aspect ratio 0.5. A single revolution is characterized by small oscillations in the aspect ratio. Unlike tank-treading, where the shape remained stationary,

tumbling is associated with a periodic flipping of the particle in the shear plane (Lebedev et al. (2007)). On the other hand, in the "trembling" mode, the long axis never completes a full revolution with the minor axis taking its place prior to the completion of 2π radians. In Figure 2.14, for non-dimensional time t = 750, for the oblate spheroid whose initial aspect ratio was 0.75, the deformed configuration is nearly spherical, thereby indicating that a "tumbling" mode transitions into a "trembling" mode with an increasing aspect ratio.

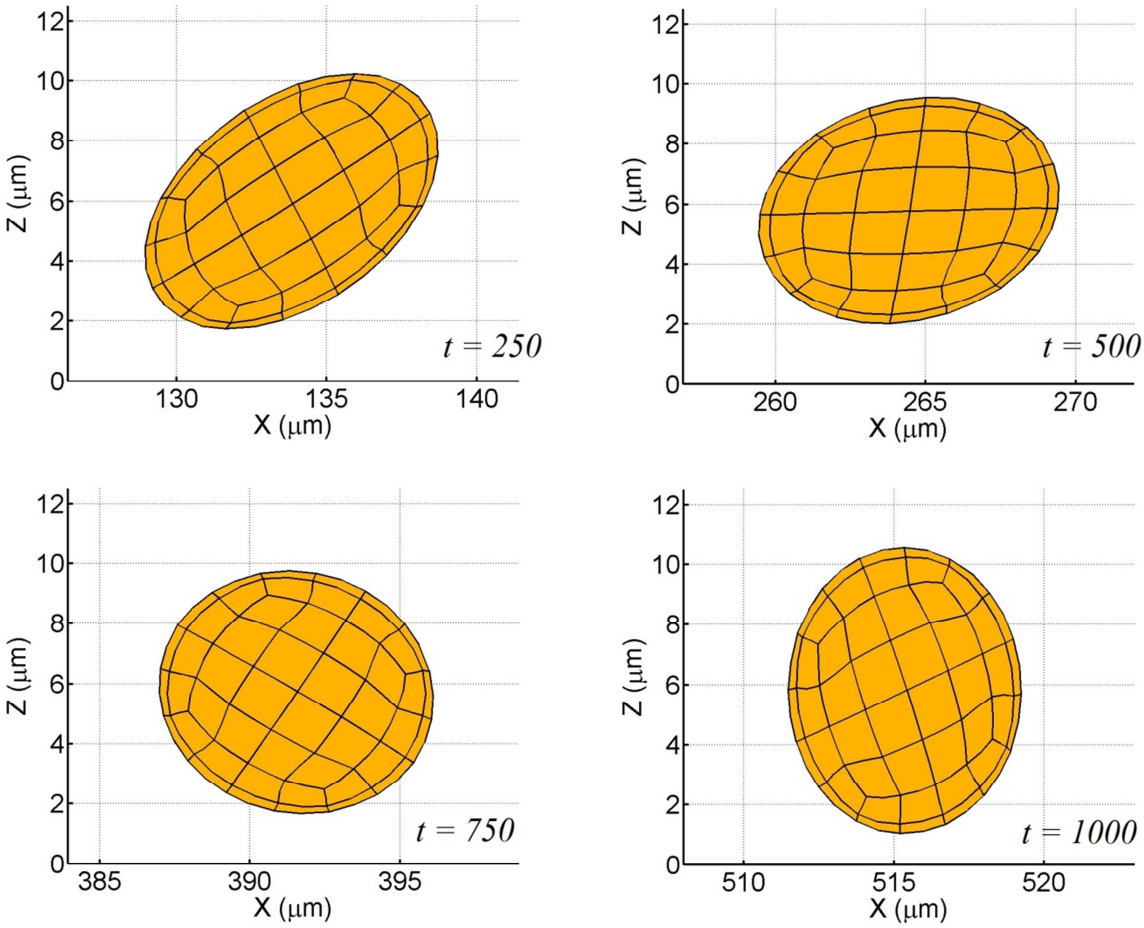

Fig. 2.14 Tumbling sequence of a deformable oblate spheroid in the proximity of a rigid wall (a = 5 μm, η = 1 Pa, v = 0.33, $\alpha = \pi/2$, κ = 0.75, $\dot{\gamma}$ = 100 s^{-1}).

At a viscous number of 0.1, the present study predicts the transition to occur at an aspect ratio in between 0.85 and 0.91. However, at a viscous number of 0.2, the transition occurred at a

lower aspect ratio (between 0.5 and 0.75), implying that the strength of the hydrodynamic forces equally influenced the trembling or tumbling modes (Appendix B).

A similar observation was made by Gao et al. (2012) for ellipsoidal inclusions that were modeled as a Neo-Hookean solids. For a viscous number of 0.2, the transition from the tumbling to the trembling regime was reported to occur at an aspect ratio of 0.681. Moreover, the stress-strain relation for Neo-Hookean materials can be expressed in terms of the principal stretch ratio λ as follows

$$\sigma = E\left(\lambda - \frac{1}{\lambda^2}\right) \qquad (2.34)$$

where $\lambda = \varepsilon + 1$, ε is the infinitesimal strain. For $\varepsilon << 1$, the term $\lambda^2 \sim 1$. Thus Eq. (2.34) reduces to

$$\sigma = E\varepsilon \qquad (2.35)$$

Equation (2.35) represents Hooke's Law of linear elasticity for infinitesimal deformations. Although the non-linear hyperelastic model potentially predicts larger deformations during the alternate stretching and compression of the material points, the transition from tumbling to trembling as predicted by the linear elastic model is in good agreement with that predicted for finite strain models at low hydrodynamic shear forces.

The computational scheme based on boundary element methods presented here is employed in all the simulations in forthcoming chapters including short-range non-adhesive interactions between free-stream cells, adhesive interactions for solitary cells and hydrodynamic interactions between free-stream and firmly adherent cells. Oblate spheroid shapes have been specifically simulated in order to assess the accuracy of the Gram-Schmidt orthonormalization introduced into the source code by Mody and King (2005). While Chapters 3 & 4 would involve

simulations comprising of spherical cells, this orthonormalization would be crucial to deformed cells, whose profiles deviate from a spherical morphology.

3 SHORT RANGE NON-ADHESIVE INTERACTIONS

Collisions between neighboring cells are unavoidable in mathematical modeling of dense suspensions of blood cells. Such collisions could potentially lead to membrane overlap of the interacting cells. However, in an actual physiological scenario, cells do not overlap or pass through the reactive substrate during adhesive interactions. Moreover, the presence of asymptotic short-range forces prevents such interferences. While some of these forces arise from the electric potential associated with the cells, others prevail due to the pressure buildup stemming from the shearing or squeezing of the surrounding viscous plasma. The inclusion of Van Der-Waal's and lubrication forces is to primarily prevent cells from overlapping with each other and interfering with the substrate.

3.1 Van Der-Waal's Interactions

At cell membrane separations of 50 - 250 Å, electrostatic repulsive forces prevail since the net charge on both cells has the same sign. The magnitude of this force is expressed as

$$F_{rep} = \frac{F_o \tau e^{-\tau\varepsilon}}{1 - e^{-\tau\varepsilon}} \qquad (3.1)$$

where $1/\tau$ – length scale and ε – surface-to-surface separation distance. For cell-cell interactions, F_{rep} is directed along the line joining the centers of the two particles and induces perturbations in the translation of the interacting particles. For cell-substrate interactions, this force is directed normal to the substrate. The value of τ is set at 2000 μm^{-1}, while F_o varies between 10^6 - 10^9 pN. In order to simplify the modeling, these forces are assumed to not produce any deformation in cells in the case of near touching and only affect particle mobilities.

The presence of microvilli on the surface of the cell and a steric layer on the wall is modeled as a uniform roughness indicated by e_s and e_w, respectively (Fig. 1.4). The values for these two parameters were set to 175 and 50 nm, respectively. Both adhesive and non-adhesive interactions occur at the tips of these roughness elements. Moreover, since the dimensions of these elements are much smaller in comparison with the dimensions of the cell, their effect on the flow-field is neglected.

3.2 Lubricated Collisions

A thin film of plasma separates interacting cells that are in close contact to one another (Goddard (1977)) and the Poisseulle theory of elastohydrodynamic lubrication is applicable to the current study where deformations are considered to be infinitesimal. The theoretical background for cell-cell lubrication is based on the works of Nasseri et al. (2000) and Rognon and Gay (2009). The ability of a cell to deform is expressed in terms of the dimensionless elasticity number $\in$ given by

$$\in = \frac{4\theta\mu u_0 a^{1.5}}{\varepsilon_0^{2.5}} \qquad (3.2)$$

where u_0 - initial velocity, ε_0 - initial separation, $\theta = \frac{1-\nu^2}{\pi E}$, E-Young's modulus, a-particle radius and μ-viscosity of medium. For leukocytes, $\in$ typically ranges between 10^{-6} - 10^{-2} (Chang and Wang (1998)), indicating that the cells are reasonably compliant. Although the Poiseulle theory of lubrication is synonymous with small deformation theory, the same has been introduced to highlight its influence on modulating the intercellular contact area.

For pairwise interactions, the force inducing deformation F_{elas} is expressed as a sum of fluid shear and lubrication forces,

$$F_{elas} = F_{shear} + F_{lubr} \tag{3.3}$$

The lubrication theory has been strictly applied to the deformation of spherical cells with identical radii and its effect on particle mobilities has been excluded. Moreover, this study adopts a minimum film thickness and assumes that the film is stable with negligible variations in film-thickness arising from cell deformation. For two equal sized spherical cells '*A*' and '*B*' moving relative to one another in a viscous medium, the force exerted by particle '*B*' on '*A*' is given by,

$$F_{lubr} = F^{sh}_{lubrAB} + F^{sq}_{lubrAB} \tag{3.4}$$

where the subscripts *sh* and *sq* indicate shearing and squeezing, respectively (Nasseri et al. (2000)). A unit vector $\boldsymbol{l}_{AB}$ is introduced to define the line joining the centers of particles *A* and *B*. Additionally, vectors $\boldsymbol{p}_{AB}$ and $\boldsymbol{q}_{AB}$ are defined as follows

$$\boldsymbol{p}_{AB} = \frac{l^x_{AB} \cdot l^z_{AB}}{\sqrt{l^{x\ 2}_{AB} + l^{y\ 2}_{AB}}}\boldsymbol{i} + \frac{l^y_{AB} \cdot l^z_{AB}}{\sqrt{l^{x\ 2}_{AB} + l^{y\ 2}_{AB}}}\boldsymbol{j} - \sqrt{l^{x\ 2}_{AB} + l^{y\ 2}_{AB}}\boldsymbol{k} \tag{3.5}$$

$$\boldsymbol{q}_{AB} = -\frac{l^y_{AB}}{\sqrt{l^{x\ 2}_{AB} + l^{y\ 2}_{AB}}}\boldsymbol{i} + \frac{l^x_{AB}}{\sqrt{l^{x\ 2}_{AB} + l^{y\ 2}_{AB}}}\boldsymbol{j} \tag{3.6}$$

where superscripts *x*, *y*, *z* represent global Cartesian co-ordinate system and $\boldsymbol{i}$, $\boldsymbol{j}$, $\boldsymbol{k}$ are unit vectors in the respective directions. The squeezing and shearing components are given as

$$F^{sq}_{lubrAB} = \frac{3\pi\mu a^2}{2\varepsilon}\boldsymbol{u}_{AB} \cdot \boldsymbol{l}_{AB}\boldsymbol{l}_{A\boldsymbol{B}} \tag{3.7}$$

$$F^{sh}_{lubrAB} = \pi\mu a \ln\left(\frac{a}{\varepsilon}\right)\boldsymbol{u}_{AB} \cdot \left(\boldsymbol{p}_{AB}\boldsymbol{p}_{A\boldsymbol{B}} + \boldsymbol{q}_{AB}\boldsymbol{q}_{A\boldsymbol{B}}\right) \tag{3.8}$$

where $\boldsymbol{u}_{AB} = \boldsymbol{u}_A - \boldsymbol{u}_B$ is the relative velocity of cell '*A*' with respect to '*B*'. Note that the squeeze component arises due to the cells approaching each other, while the shear component is generated by the cells moving past one another. The right hand side of Eq. (2.25) is suitably augmented as per the traction on local elements to compute a converged traction distribution on the cell surface.

3.3 Numerical Validation

The numerical code has been appropriately modified to account for non-adhesive interactions. An adaptive time step of 10^{-4} - 10^{-5} is employed based on the proximity of the colliding cells. The integration of the double layer and the adjoint double layer over the singular element is carried out as per the strategy proposed by Phan-Thien and Fan (1996) with the exception that the adaptive discretization of the singular elements has not been included in this thesis.

The combined effect of colloidal and lubrication forces are illustrated through numerical simulations for equal sized cells with a = 5 μm, η = 8 kPa, ν = 0.33 for the first case and a = 5 μm, η = 4 kPa, ν = 0.33 for the second case. Figure 3.1 indicates the lubrication gap for the two cases at the same time instant. Figure 3.1b indicates a larger lubrication gap stemming from the compressive deformation of the more compliant cells (η = 4 kPa). The deformed profiles have a distinct parabolic profile (Fig. 3.2) (Davis et al. (1986)) and the consequence of the deformation is an increased intercellular contact area. Similar cases involving elastic capsules (Jadhav et al. (2007)) and droplets (Loewenberg and Hinch (1997)) have been studied previously.

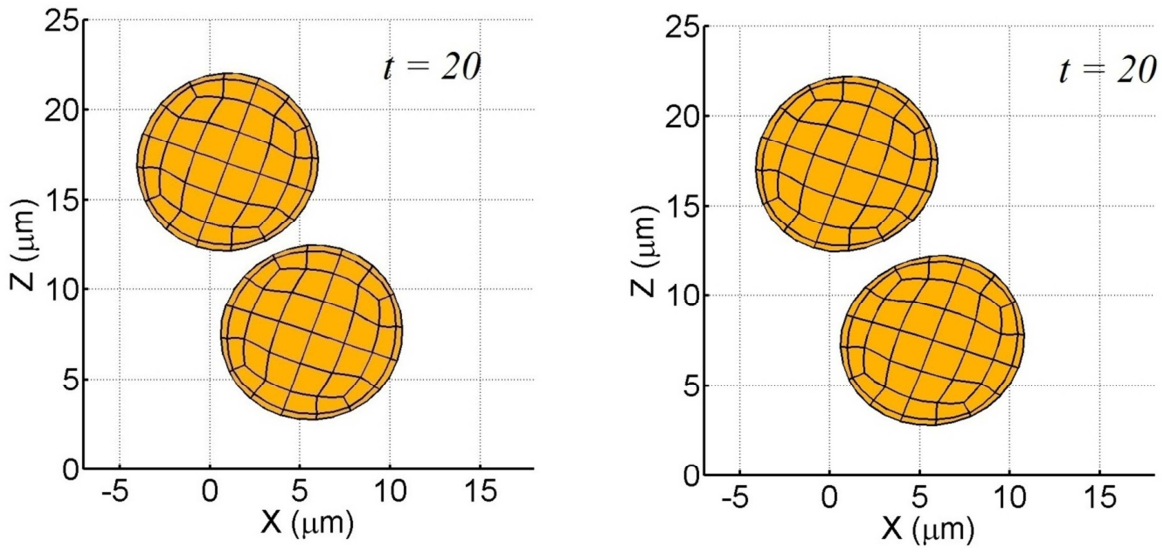

(a) **(b)**

Fig. 3.1 Lubricated collisions between two spherical cells in the proximity of the reactive substrate. For both simulations a = 5 μm, $\dot{\gamma}$ = 100 s^{-1}, ν = 0.33: (a) stiff particles, η = 8 kPa (b) relatively more compliant particles, η = 4 kPa.

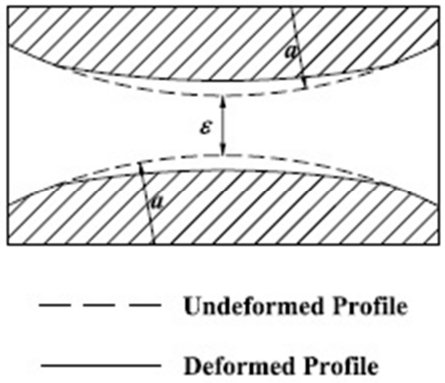

Fig. 3.2 Lubricated collisions between elastic spheres.

Such deformations between colliding neutrophils have been observed in vitro by Kadash et al. (2004) in order to understand the influence of the inter-cellular contact area on the shear thresholding of leukocytes. The asymptotic variations in the shear and squeeze components with surface separation is indicated in Figure 3.3.

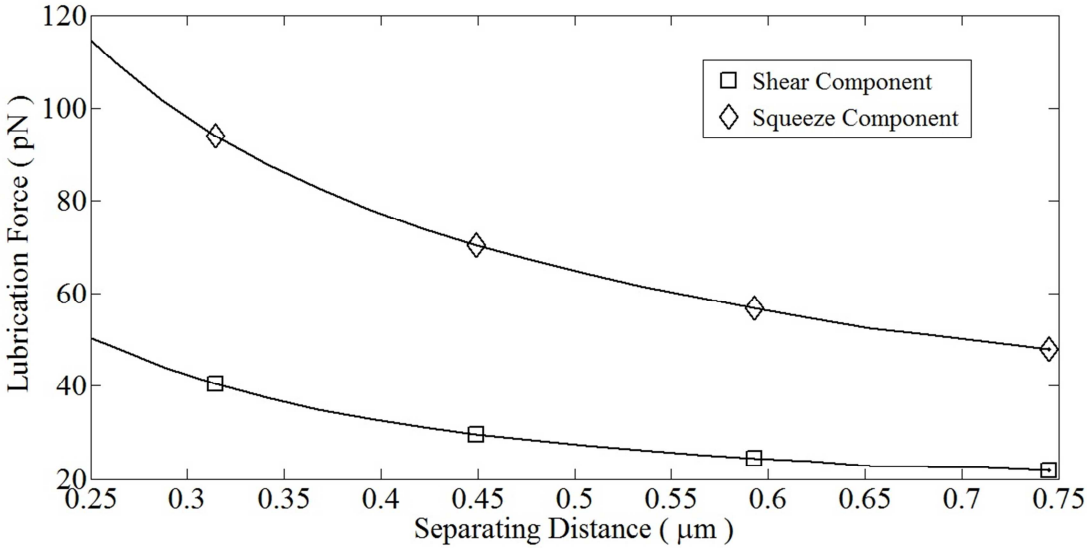

Fig. 3.3 Variation in shear (□) and squeeze components (◊) of lubrication with increasing cell-cell separation.

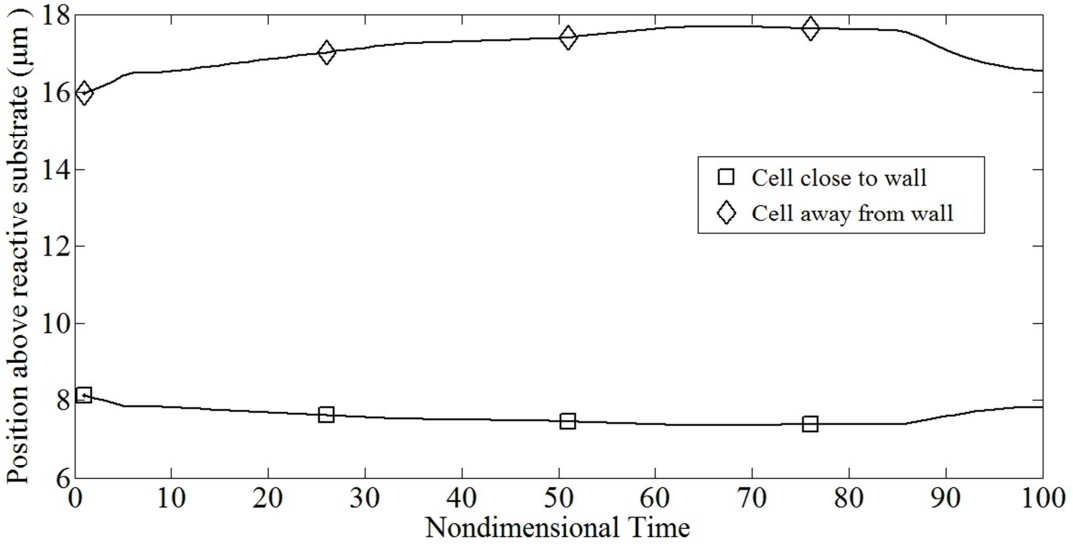

Fig. 3.4 Trajectories of free-stream cells undergoing binary collisions in the proximity of the reactive substrate.

Owing to its position above the wall, the upper cell experiences a lower resistance and translates at a higher velocity as compared to its lower counterpart. Eventually, upon catching up with the lower cell, the short-range repulsive forces push the cells apart and the lower cell is nudged closer to the wall where adhesive interactions are possible (Fig. 3.4). This idea of driving

cells towards a reactive substrate via binary collisions has been demonstrated previously (Melder et al. (1995, 2000)). Electrostatic repulsion forces introduced in this chapter are also employed in simulations involving single cell rolling as this prevents membrane substrate overlap. Moreover, the presence of lubrication forces between colliding cells is also acknowledged through the aforementioned test cases.

4 ADHESIVE INTERACTIONS

4.1 Modeling Biochemistry

When a leukocyte is in close proximity to inflamed endothelium, there exists the possibility of an antigen on one cell interacting with an antibody on the other cell thereby generating an adhesive bond. Bell (1978) studied such adhesive interactions and formulated a theoretical model that describes these types of interactions. The model depends on the rates of bond formation and breakage, number of receptors per unit area, and the current bond forces.

The present study models adhesive bonds as Hookean springs and associates the rate of bond dissociation k_r with the magnitude of the bond force F_{bond} as

$$k_r = k_r^0 \exp\left(\frac{r^0 F_{bond}}{k_b T} \right) \qquad (4.1)$$

where k_r^0, r^0 have been determined experimentally, k_b is Boltzmann's constant, and T is absolute temperature (King and Hammer (2001a)). Similarly, the rate of bond formation k_f follows from the Boltzmann distribution for affinity as

$$k_f = k_f^0 \exp\left(\frac{\sigma \left| \boldsymbol{x}_b - \lambda \right| \left(r^0 - 0.5 \left| \boldsymbol{x}_b - \lambda \right| \right)}{k_b T} \right) \qquad (4.2)$$

where σ is the spring constant, λ the equilibrium bond length, $\left| \boldsymbol{x}_b - \lambda \right|$ is the deviation bond length. Unlike the studies conducted by Dong and Lei (2000) and Ward et al. (1994), the spring constant remains unchanged throughout the simulation.

The transient nature of selectin mediated leukocyte rolling has been described as a stop-and-go motion (Chen and Springer (1999), Kim and Sarelius (2004), Schmidtke and Diamond (2000) and Yago et al. (2002)). This stochastic formation and breakage of adhesive bonds is modeled using a Monte-Carlo technique.

The position vector of the microvillus tip $\boldsymbol{x}_m = \{x_m\, y_m\, z_m\}$ is tracked as the cell rolls on the substrate, while the same for the surface attachment point $\boldsymbol{x}_o = \{x_o\, y_o\, z_o\}$ remains fixed. The time varying vector describing each bond $\boldsymbol{x}_b = \boldsymbol{x}_o - \boldsymbol{x}_m$ is used to determine the force and torque on each bond as follows:

$$\boldsymbol{F}_{bond} = \sigma\left(|\boldsymbol{x}_b| - \lambda\right)\left(\frac{\boldsymbol{x}_o - \boldsymbol{x}_m}{|\boldsymbol{x}_b|}\right) \tag{4.3}$$

$$\boldsymbol{T}_{\boldsymbol{bond}} = \left(\boldsymbol{x}_o - \boldsymbol{x}_c\right) \times \boldsymbol{F}_{bond} \tag{4.4}$$

where $\boldsymbol{x}_c$ is the position vector of the centroid of the spherical cell. The bond forces and torques, as well as the colloidal forces, serve as an input to Equation 2.16 to determine the particle mobility, from which the length and orientation of the bonds are updated.

4.2 Interfacial Compression

A rolling leukocyte may encounter contact stresses along the interface and deform as a result of the interaction. Interfacial compression can increase the contact area (Subramaniam DR (2012)) and thereby enhance adhesive interactions (Fig. 4.1). The theory of contact mechanics is revisited with a view to explain the modulation of the cell-substrate interface. The distances separating the cell and substrate are of the order of 100 nm, thereby permitting a dry contact formulation (Rognon and Gay (2008) and Villaggio (1996)).

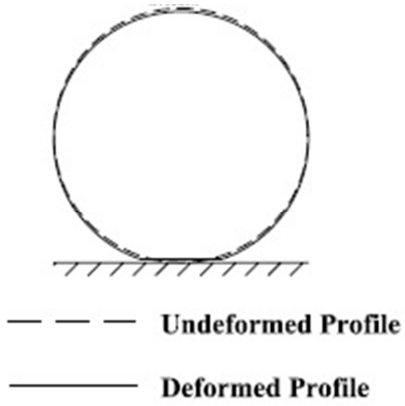

Fig. 4.1 Interfacial compression of an elastic sphere contacting a rigid wall.

The forces acting on a tethered cell are indicated in Figure 4.2 and for static equilibrium, $\Sigma \boldsymbol{F} = \mathbf{0}$, $\Sigma \boldsymbol{T} = \mathbf{0}$ (Alon et al., 1995)).

For equilibrium,

$$F_{bond}^{x} = \boldsymbol{F}_{bond} \cos\theta = F_{shear} \qquad (4.5)$$

$$F_{bond}^{z} = \boldsymbol{F}_{bond} \sin\theta = F_{hertz} \qquad (4.6)$$

$$F_{bond}^{x} \left(a + e_s\right) \sin\theta + T_{shear} = F_{bond}^{z} \left(a + e_s\right) \cos\theta \qquad (4.7)$$

where θ is the inclination of the bond, e_s is the cell roughness. The vertical component of the bond force F^{z}_{bond} tends to restrain the cell against the solid wall. The resulting reaction force (Chen and Springer (1999), Smith et al. (1999)) produces a compressive deformation. Similar ideas have been proposed by King et al. (2005) and Wankhede et al. (2006) in relation to leukocytes modeled as elastic spheres.

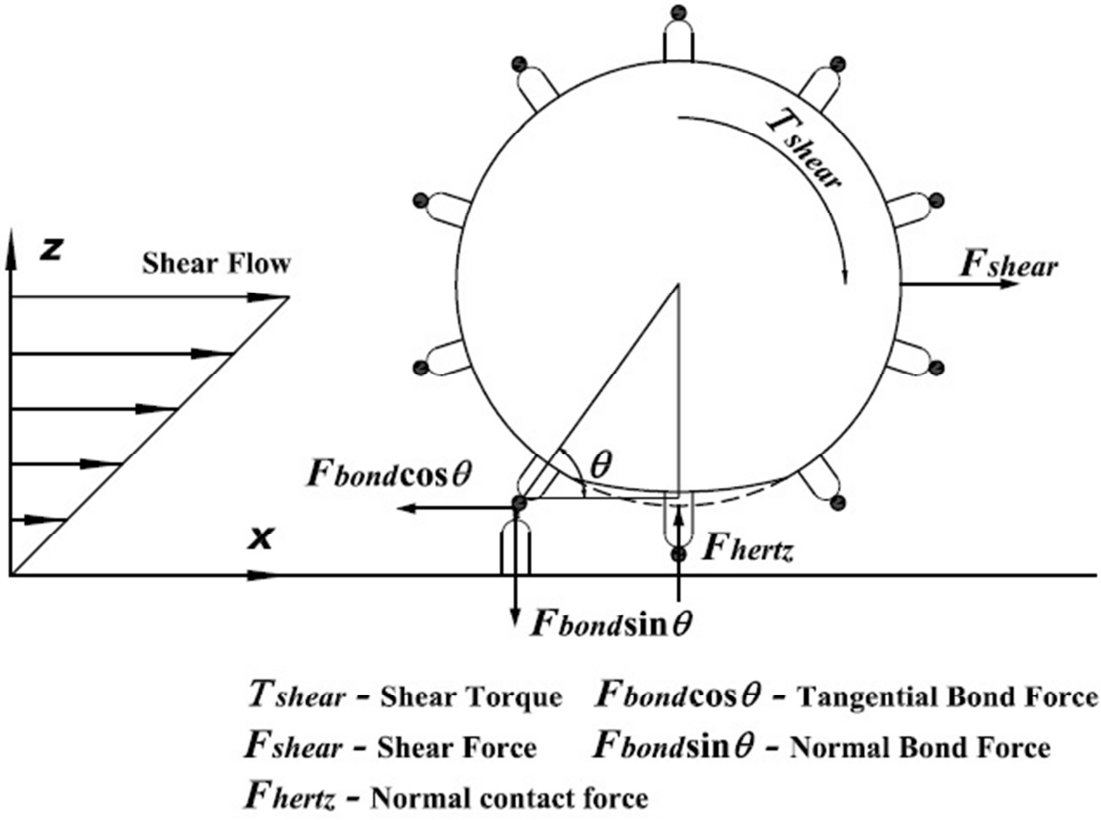

Fig. 4.2 Force and torque balance on a tethered cell.

In the absence of tangential traction, using Bondareva's equation for small contact angles, the normal traction distribution on the bottom face is given by Villaggio (1996),

$$t_0 = -\frac{3F_{hertz}}{2\pi a_s^2} \tag{4.8}$$

where a_s is the contact radius, and F_{hertz} is the normal reaction. The contact radius is expressed in terms of the cell radius a, the normal reaction and the corrected Young's modulus $E_{correct}$ (Chang and Wang (1998)),

$$a_s = \sqrt[3]{\frac{3F_{hertz}a}{4E_{correct}}} \tag{4.9}$$

where $E_{correct} = E / (1-\nu^2)$. Equation (4.8) is used to supplement the right hand side of Eq. (2.25) as a traction on local elements to compute a converged traction distribution on the cell surface. The area of the interface is then calculated as a circular disk which serves as an input to the bio-chemistry loop. The logic of the simulation proceeds as follows:

1. In the first time step, the number of receptors available for bond formation is calculated based on the area of a hemispherical cap in the proximity of the substrate (Cozens-Roberts et al. (1990)). This step serves to "anchor" the cell to the substrate.

2. In the subsequent time steps, the sum of the normal components of all surviving bonds is computed in order to determine the interfacial traction and the contact radius given by Eq. (4.8)-(4.9). The resulting contact area is multiplied by the receptor density to determine the number of potential bonds that could form in subsequent time steps.

4.3 Numerical Validation

Solitary cell rolling simulations were conducted to assess the efficiency of the modified contact area logic. The time steps for adhesive interactions were maintained in the range of 10^{-8} to 10^{-6}, while the number of iterations employed for pairwise interactions between free-stream cells were adopted in this study. The parameters employed in these simulations are given in Table 4.1.

PARAMETER	DEFINITION	VALUE
a	Cell Radius	3-5 μm
$\dot{\gamma}$	Shear Rate	100 s^{-1}
μ	Viscosity	1 cP
ρ	Fluid Density	1 gm/cc
ρ_g	Cell Density	1.05 gm/cc
e_s	Cell Roughness	175 nm
e_s	Substrate Roughness	50 nm
σ	Spring Constant	0.5-100 dyn/cm
λ	Equilibrium Bond Length	30 nm
k_r^0	Unstressed Off-Rate	2.4 s^{-1}
r^0	Reactive Compliance	0.39 Å
k_f^0	Intrinsic On-Rate	365 s^{-1}
n_r	Receptor Density	20 molec/ μm^2
η	Shear Modulus	0.5-10 kPa
v	Poisson's Ratio	0.33

*Note, some values of shear moduli have been determined using atomic force microscopy (AFM) for non-adherent HL-60s, PMNs, and Jurkat cells with v = 0.5 (Rosenbluth et al. (2006)).

4.3.1. Preliminary Run

A series of simulations were performed to demonstrate the ability of the area modulation sub-routine to predict more receptors for deformable cells as compared to their rigid counterparts. Adhesive interactions involving two compliant cells with a = 5 μm, η = 0.508 - 1 kPa and v = 0.33, and a third rigid cell of the same radius were run for 2000 time steps with σ = 100 dyn/cm. Figure 4.3 indicates the effect of the normal reaction on two cells of varying compliance. The compliant cell (Fig. 4.3a) is substantially deformed with a flat interface as compared to its rigid counterpart (Fig. 4.3b).

The contact area was found to increase sharply for the most compliant cell, and gradually for its stiffer counterparts (Fig. 4.4). Moreover, Figure 4.5 illustrates the direct proportionality between the contact area and the normal reaction. Furthermore, the inverse relationship between

contact area and compliance is also highlighted in this plot. The average contact area for the highly deformable and moderately deformable cell was 6.2 and 1.9 μm^2, respectively. The increased contact area could result in more receptors being available for bond formation, and subsequently slower rolling velocities for more compliant cells.

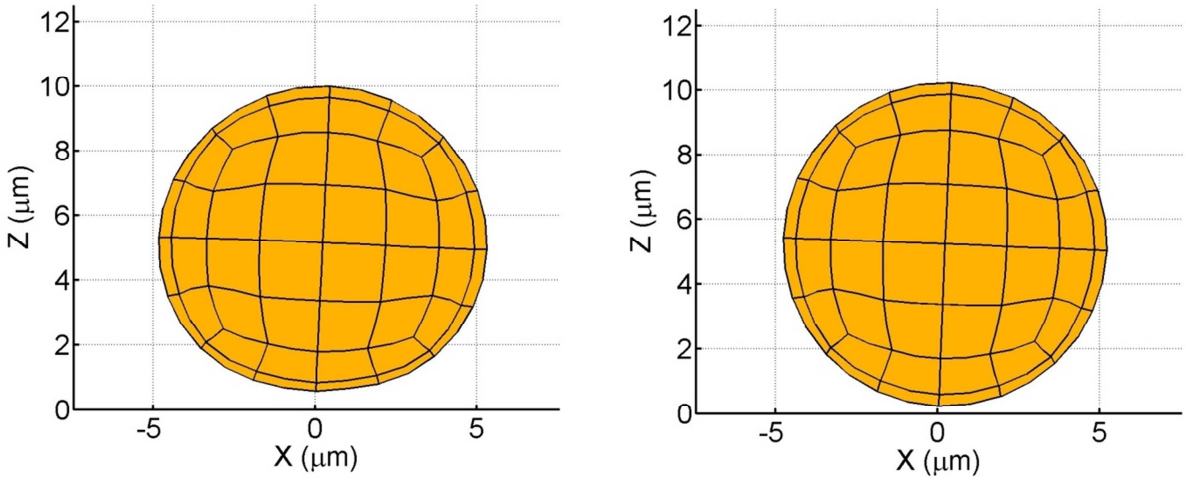

(a) (b)

Fig. 4.3 Tethered cells (a) compressed, compliant (η = 0.508 kPa, ν = 0.33) (b) rigid, a = 5 μm.

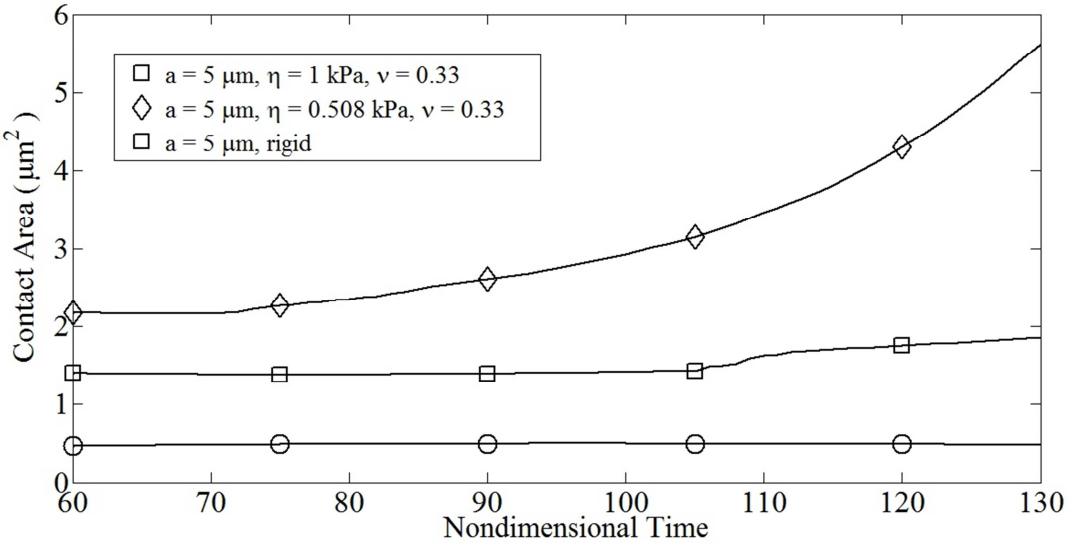

Fig. 4.4 Variation in contact area of compliant (◊) and stiff (□) cells with time.

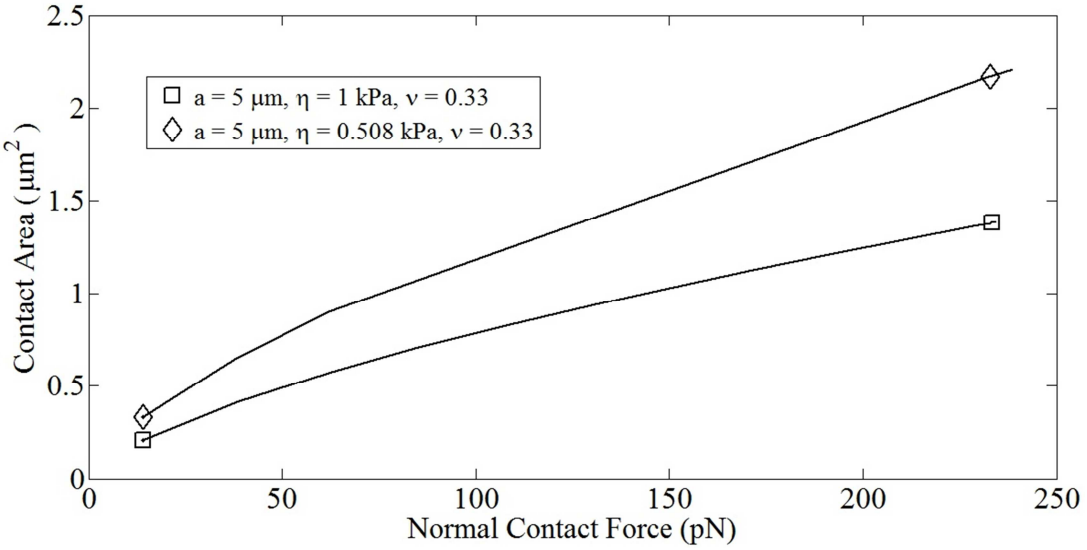

Fig. 4.5 Variation in contact area of compliant (◊) and stiff (□) cells with normal contact force.

Besides, the translational velocities dropped to 130 and 140 μm/s from a free-stream velocity of 350 μm/s; for the compliant and stiff cells, respectively (Fig. 4.6). This implies that compliant cells could roll considerably slower than their stiff counterparts (Jadhav et al. (2005)).

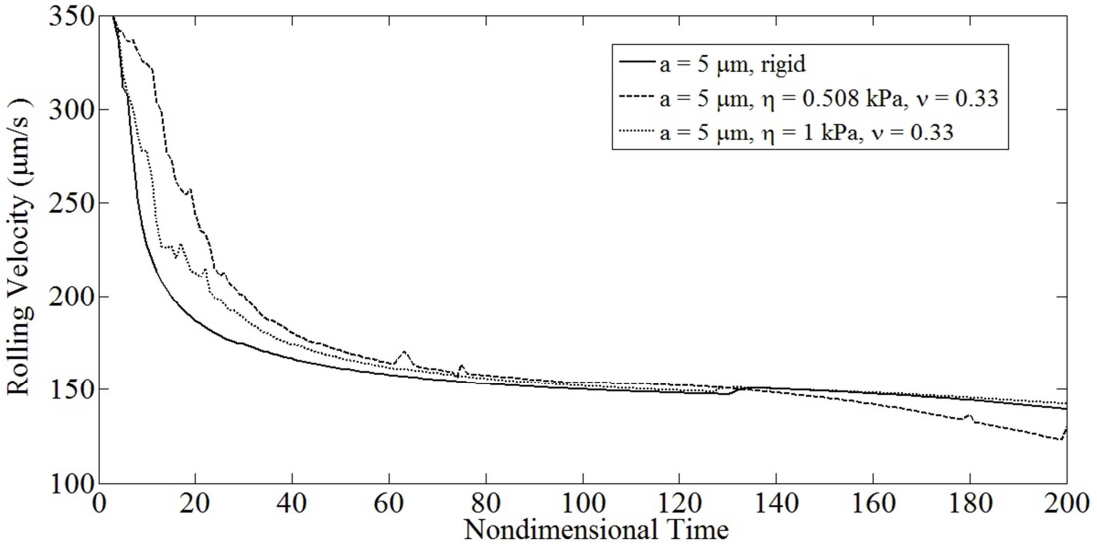

Fig. 4.6 Drop in the translational velocities of stiff and compliant cells with time. For all simulations a = 5 μm, $\dot{\gamma}$ = 100 s^{-1}, ν = 0.33: cell compliance η = 0.508, 1 kPa.

4.3.2. Refinement of Results

Although cell membranes do not possess a yield point, the deformations resulting from these simulations were large and may violate the theory of linear elasticity, as well as the Hertzian theory for small contact angles. One of the reasons for this 'large' deformation appeared to stem from the stiffness of the bond in relation to the membrane elasticity. In order to circumvent this problem, a series of simulations involving a much smaller bond stiffness (σ = 0.5 dyn/cm) (Hammer and Apte (1992)) was run for cells with varying radii (a = 3 - 5 μm) and lower compliance (η = 4 - 10 kPa). Besides, this parameter matching was introduced in order to generate more stable and longer running simulations.

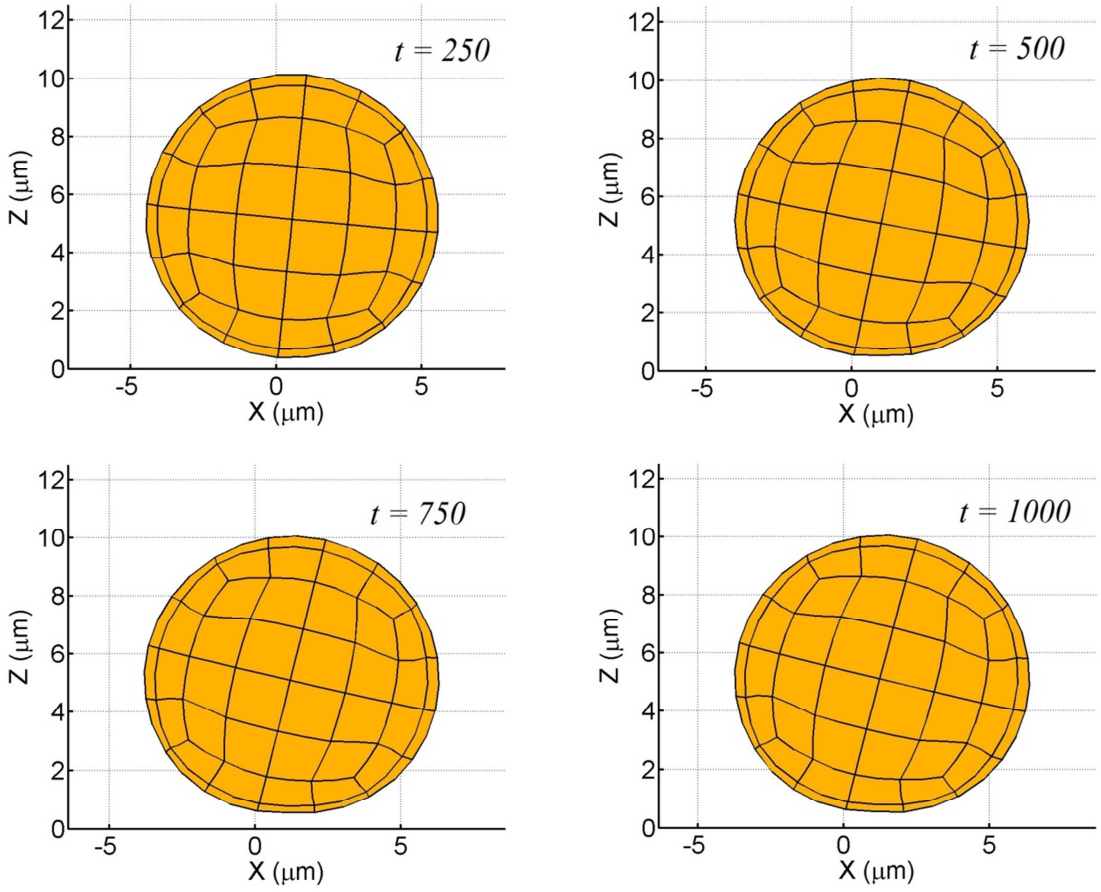

Fig. 4.7 Rolling sequence of a moderately compliant cell (η = 4 kPa, v = 0.33, σ = 0.5 dyne/cm, a = 5 μm).

The progressive increase in contact area with time is observed from the rolling sequences indicated in Figure 4.7-4.8. As compared to the negligible compression observed at t = 250, the cell appears to be more compressed at t = 1000, thereby indicating the effect of the wall reaction.

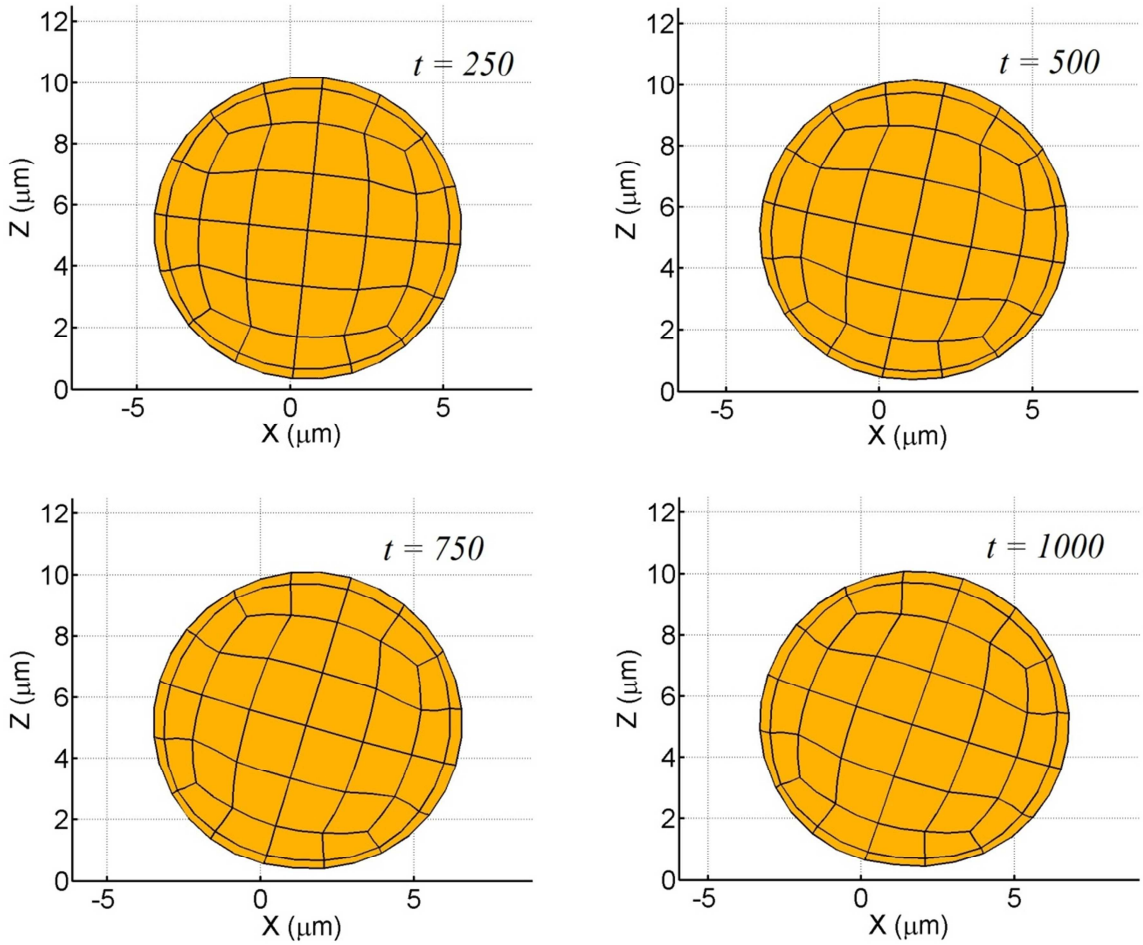

Fig. 4.8 Rolling sequence of a relatively stiff cell (η = 10 kPa, ν = 0.33, σ = 0.5 dyne/cm, a = 5 μm).

Figure 4.9 compares the drop in the rolling velocity of two cells with identical dimensions and varying compliances. The same dropped from a free-stream velocity of 350 μm/s to 13 μm/s and 45 μm/s, for the compliant and stiff cells respectively (Fig. 4.9). This implies that the adhesion subroutine is consistent irrespective of material parameters. Moreover, the translational velocities decreased to a value observed for either in vivo or in vitro cell rolling experiments.

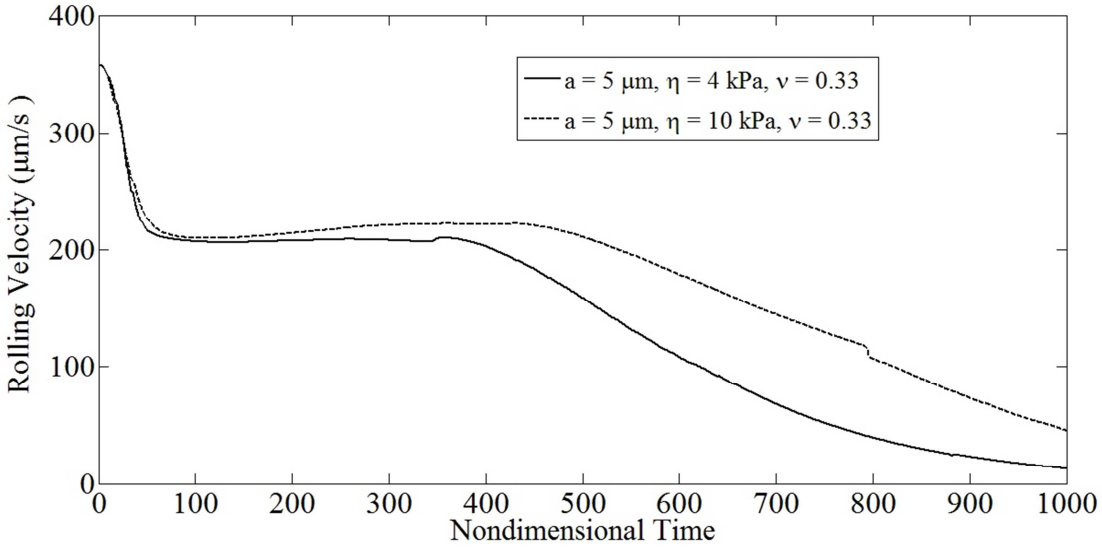

Fig. 4.9 Drop in the translational velocities of cells of identical dimensions and varying compliance with time. For both simulations a = 5 μm, $\dot{\gamma}$ = 100 s^{-1}, v = 0.33: cell compliance η = 4, 10 kPa.

Figure 4.10 compares the drop in the rolling velocities of cells with varying dimensions and identical compliance. For a cell with 4 μm radius, the velocity dropped to 7.5 μm/s,

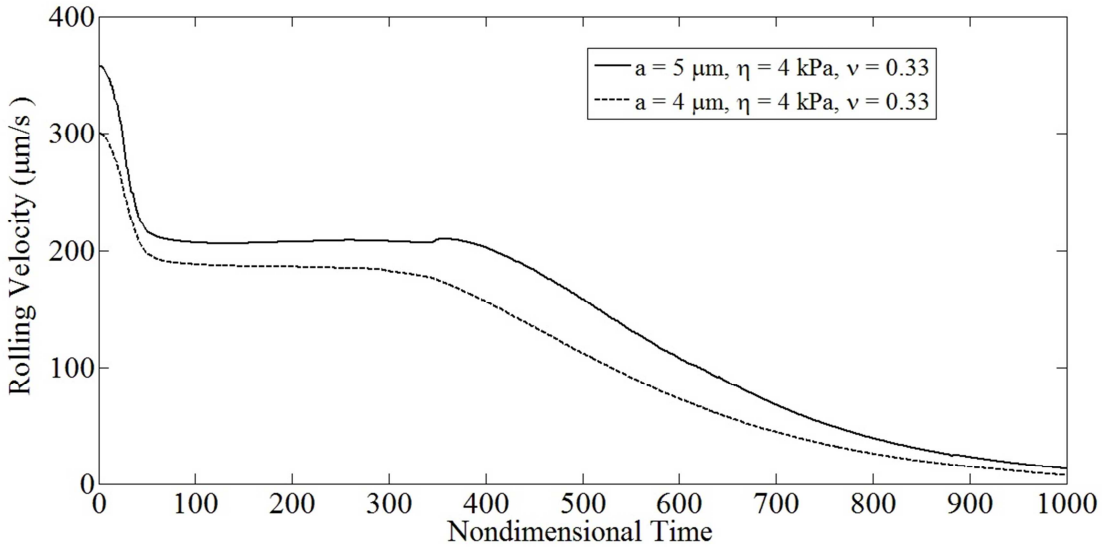

Fig. 4.10 Drop in the translational velocities of cells of identical compliance and varying dimensions with time. For both simulations η = 4 kPa, $\dot{\gamma}$ = 100 s^{-1}, v = 0.33: cell characteristic radius a = 4, 5 μm.

compared to 13 μm/s for a 5 μm radius cell. This implies that smaller cells could potentially roll slower than their larger counterparts, primarily because their free-stream velocity is lower.

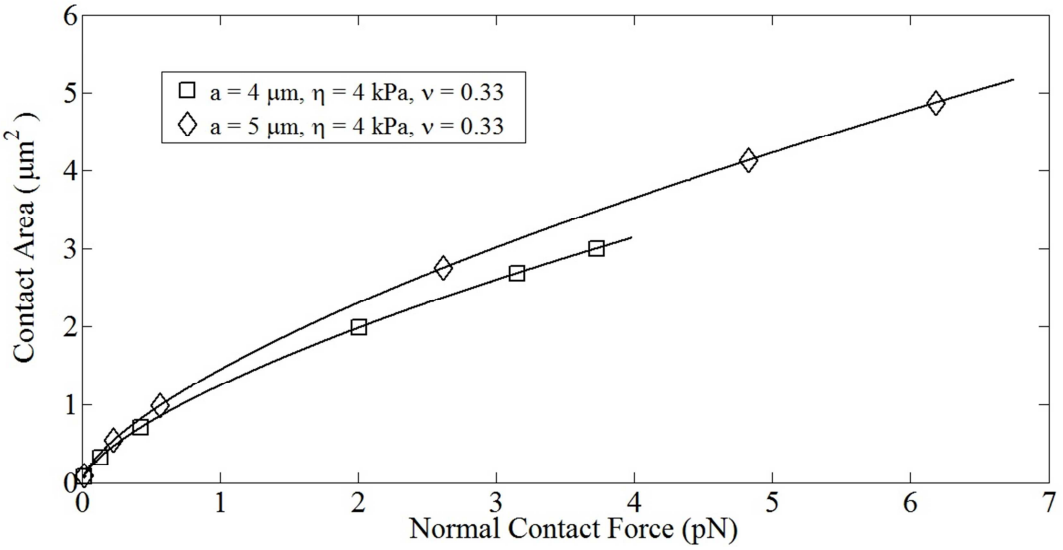

Fig. 4.11 Variation in contact area for cells with identical compliance and different sizes: a = 4 μm (□), a = 5 μm (◊) with normal contact force. For both simulations η = 4 kPa, $\dot{\gamma}$ = 100 s^{-1}, ν = 0.33.

The direct proportionality between the contact radius and the cell radius is indicated in Figure 4.11. Although the higher contact area for the larger cell resulted in more bonds (39 surviving bonds) as compared to the smaller cell (33 surviving bonds), the paradox that smaller cells could potentially roll slower prevails (Patil et al. (2001)). Besides, the average contact area recorded over the entire length of the simulation for the 4 μm and 5 μm cells was 1.87 and 3.19 μm^2, respectively. The contact angle ω is determined using the relation

$$\omega = \sin^{-1}\left(\frac{a_s}{a}\right) \qquad (4.10)$$

For the two cases considered, the same was determined to be approximately 11 degrees, implying that the small angle approximation was reasonable.

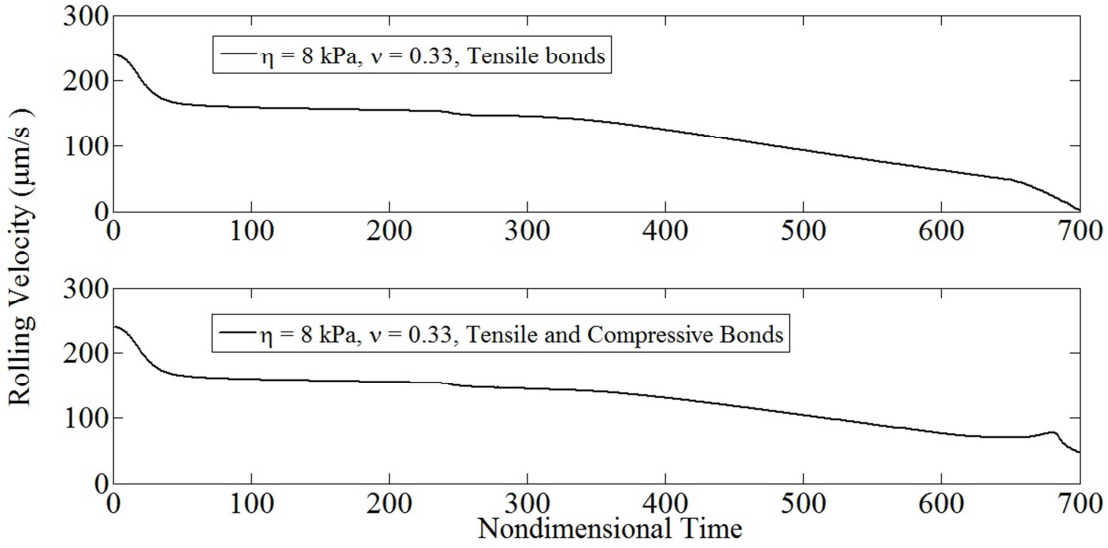

Fig. 4.12 Drop in translational velocities for a compliant cell with adhesive bonds loaded in tension or compression. For both simulations η = 8 kPa, $\dot{\gamma}$ = 100 s^{-1}, ν = 0.33: upper panel – tensile bond forces, lower panel - tensile and compressive bond forces.

In order to portray the noisy nature of leukocyte rolling described earlier, a final set of solitary rolling results involving cells with a radius of 3 μm, shear modulus 8 kPa and Poisson's ratio of 0.33 were run for a total of 10000 time steps. An upper limit of 40 bonds was imposed on the adhesion loop. In all the aforementioned cases, the adhesive interactions were modeled considering tensile bond forces only. Bond compression was included in these simulations to illustrate its effect on the translational velocity of the cell. Figure 4.12 compares the drop in the translational velocities for the 2 cases as the number of bonds grew from 0 to 40. It was observed that for the test case involving only tensile bonds, the velocity dropped to 1 μm/s, compared to 48 μm/s for the second case involving both tensile and compressive bonds (for the same number of time steps). This result implies that bonds under compression negate the effect of tensile bonds to retard the cell rolling velocity.

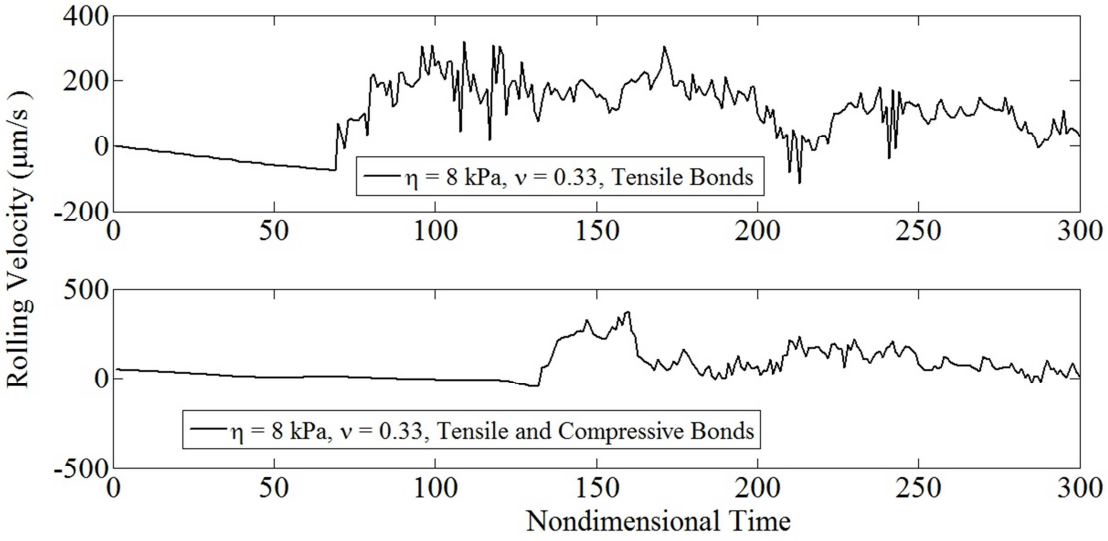

Fig. 4.13 Noisy rolling for a compliant cell with adhesive bonds loaded in tension or compression. For both simulations η = 8 kPa, $\dot{\gamma}$ = 100 s^{-1}, ν = 0.33: upper panel – tensile forces, lower panel - tensile and compressive bond forces.

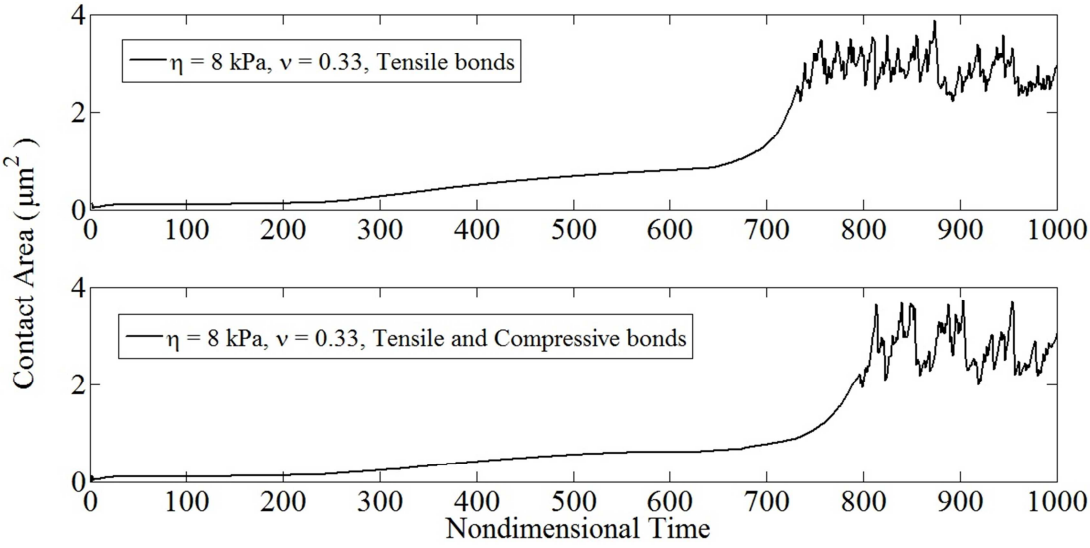

Fig. 4.14 Time varying contact area for a compliant cell with adhesive bonds loaded in tension or compression. For both simulations η = 8 kPa, $\dot{\gamma}$ = 100 s^{-1}, ν = 0.33: upper panel – tensile forces, lower panel - tensile and compressive bond forces.

Since the limit on the number of bonds was set to 40, the algorithm mathematically 'broke' any additional bonds that attempted to form in the remaining time steps. The effect of this artificially induced bond rupture on the rolling velocity and the contact area is indicated in Fig.

4.13-14. The ‘stop-and-go’ motion is quantified in terms of the noisy rolling predicted by the transient formation and breakage of the bonds. Moreover, the average rolling velocity (RMS) predicted during this period was reported as 135 μm/s for the test case involving tensile bonds, and 123 μm/s for the case involving tensile and compressive bonds. The forced breakage of bonds also led to a noisy plot for the contact area that originally appeared to continuously increase with time. This noise in the trends for rolling velocity and contact area has been simulated and observed previously by Hammer and Apte (1992), Jadhav et al. (2005), and Pappu and Bagchi (2008). Moreover, the observation that the rolling velocity of adherent leukocytes is many times smaller than the free-stream velocity is crucial to the simulations conducted in the forthcoming chapter on cell recruitment.

5 RECRUITMENT OF IMMUNE CELLS

5.1 Overview of Physiological Problem

Cell trafficking is integral to inflammatory response. For example, numerous in vivo experiments have revealed large accumulations of leukocytes at the site of tissue injury or infection. For instance, Zymosan-Activated Serum (ZAS) induced adhesion of leukocytes occurred within 2 minutes of exposure in rabbits (Argenbright et al. (1991)) and by the end of 10 minutes following exposure, most of the endothelial cells were covered with white blood cells. In another trial, acute inflammation in hamster cheek pouches resulted from a 5 minute topical challenge with ovalbumin (Raud et al. (1988)). After approximately 5 minutes, an increase in marginating and adhering leukocytes was observed in venules of all sizes. Moreover, the accumulation was sustained and even after 40 minutes, the number of leukocytes making adhesive interactions with the inflamed substrate remained elevated.

A possible contribution for this cell accumulation is through a phenomenon termed "hydrodynamic recruitment" which is defined by King and Hammer (2003) as the downstream attachment of a previous free-stream cell resulting from the binary collision with an adherent or rolling cell. It is presumed to occur due to a vertical displacement of the free-stream cell induced by hydrodynamic interactions with the adherent or rolling cell, and the probability of cell-substrate interactions is enhanced due to the cell being displaced towards the reactive substrate. The flow chamber assay has been employed to observe this phenomenon in vitro. King and Hammer (2001b) coated polystyrene micro-spheres with Sialyl-Lewis^x (a tetrasacccharide expressed on the surface of circulating leukocytes and known to mediate dynamic adhesive

interactions with P-selectin) (Rodgers et al. (2000)) and suspended them in 1% BSA* solution. Polystyrene slides were coated with P-selectin and then washed with 2% BSA solution. The substrate was assembled into a parallel plate flow chamber and the microspheres were perfused through the flow chamber using a syringe pump. The coated beads appeared to attach 3 to 4 diameters downstream of an adherent reference cell for all shear rates employed in the experiments.

King et al. (2003) also reported that adherent leukocytes in post-capillary venules in cheek pouches of anesthetized hamsters appeared to provide a small nucleation site for recruitment of additional circulatory cells. Moreover, only a small percentage of secondary attachments appeared to stem from cell-cell adhesion (that is, the formation of adhesive bonds between pairs of colliding leukocytes, mediated by L-selectin) while a majority of these events were attributed to the phenomenon of hydrodynamic recruitment. St. Hill et al. (2003) hypothesized that although binary collisions with erythrocytes aided secondary recruitment, some of these adhesion events could also be attributed to hydrodynamic interactions between adherent cells and free-stream cells.

5.2 Past Numerical Studies; Modeling Deformable Cells

Numerical simulations involving a series of in-plane and glancing collisions between rigid model cells were conducted by King and Hammer (2001b) to determine the most favorable circumstances for secondary recruitment. They found that collisions associated with glancing

* BSA was introduced into solution to block non-specific cell-cell adhesion resulting in neutrophil stringing – an alternate form of secondary recruitment described by Kadash, K.E., Lawrence, M.B., Diamond, S.L., 2004. Neutrophil String Formation: Hydrodynamic Thresholding and Cellular Deformation during Cell Collisions. Biophys J 86, 4030-4039.

distances (separation between the centroids of the interacting cells in the lateral direction) of 5 μm or lower resulted in the lifting of the free-stream cell off the surface resulting in little or no possibility of capture. However, for glancing distances greater than 7.5 μm, the probability of downstream attachment appeared to be greatest. It was also reported that a stationary or firmly adherent cell could generate a similar effect.

Numerical studies with deformable cells presents several challenges including variability in leukocyte characteristic diameter (Patil et al. (2001)) and cell compliances (Rosenbluth et al. (2006)), and, subsequently, variability in the rolling velocities for solitary rolling cells (Section 4.3). Besides, dynamic deformations of the rolling cell alter the flow field continuously, resulting in higher computational time arising out of the complex nature of the updating process (Jadhav et al. (2005), Pappu et al. (2008), Pappu and Bagchi (2008)). This problem has been circumvented by simplifying the numerical code discussed in the previous chapters to one involving particle mobility. A computational strategy proposed by Hoskins et al. (2009) suggested holding the shape of a pre-deformed, rigid adherent polymorphonuclear (PMN) leukocyte while simulating interactions with a circulating cancer cell. A similar strategy has been adopted in this thesis by applying known fluid and chemistry induced external stresses and holding the resulting deformed cell shape over the entire length of the simulation. Gram-Schmidt orthogonalization for non-spherical particles (Section 2.2) has been utilized to determine the disturbance in the flow field arising out of arbitrary shaped particles.

Such a simplification of the problem permits comparison with fundamental flow problems and the adoption of computational strategies necessary to solve them. In this case, the problem reduces to that of a shear flow over bluff bodies protruding from a plane horizontal wall. Previously, two-dimensional finite difference procedures have been formulated to study the

disturbances in the flow-field around semi-circular and semi-elliptical bodies (Kiya and Arie (1975)). This strategy was extended by Brooks and Tozeren (1996) to adherent cells of a variety of shapes including circular and cone-shaped cells. They based their computations on the assumption that the flow-field around stationary cells could be representative of one that dynamically varies (due to cell deformation and movement) since rolling velocities are orders of magnitude smaller than free-stream velocities. Besides, analytical solutions for velocity fields have been derived for hemispherical protruberances by method of Legendre polynomials (Sugiyama and Sbragaglia (2008)) and spherical obstructions (O'Neill (1968)) using Bessel functions.

The boundary element method has been employed to solve similar problems involving axisymmetric protruberances (Pozrikidis (1997), Pozrikidis (2000), Blyth and Pozrikidis (2006)). The free-space Green's function for the fluid domain was appropriately modified to account for no-slip boundary conditions at the plane wall (Section 2.2). A similar problem involving the force distribution on raised endothelial cells was studied by Hazel and Pedley (2000).

5.3 Results

The strategy of holding the shape constant for the adherent cell in a binary interaction over the entire length of the simulation enabled results to be generated for multiple cells at time steps as large as 10^{-5} s. Although deformable cells with low viscous number have been simulated, the numerical code is capable of simulating cells with a range of viscous numbers (Section 2.3). In the simulations, cell radius was fixed at 5 μm and three different adherent cells were modeled: spherical, moderately deformed or "dome-shaped", and highly deformed or "box-shaped" (Fig.

5.1). A slight bulge is observed in the meshes for the deformed cases owing to the compression of the cell.

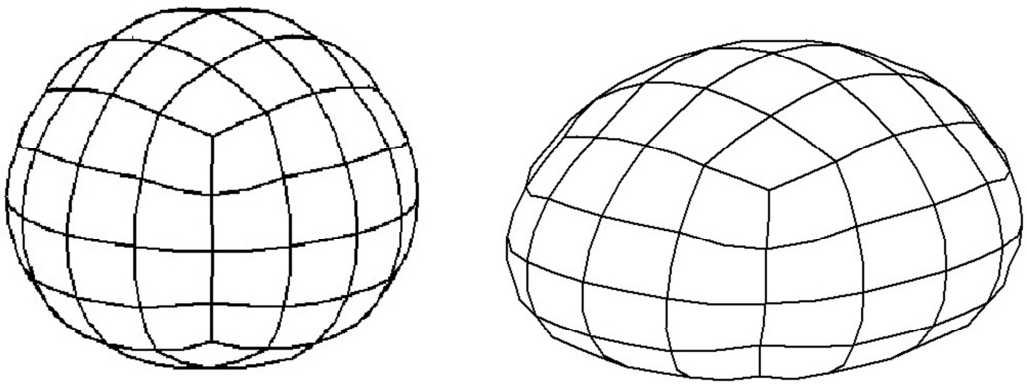

(a) **(b)**

Fig. 5.1 96 element discretization of (a) moderately deformed (b) highly deformed cells.

Moreover, the deformed cell-shapes (Fig. 5.1a,b) are representative of those observed by Tözeren and Ley (1992). The following sections discuss the results obtained for binary collision events involving one or more firmly adherent cells interacting with a free-stream cell.

5.3.1. Binary collisions (free-stream cell at least one cell diameter above substrate)

I. Binary interaction with adherent cell

A stationary, spherical, adherent cell was maintained with center of gravity at 5.25 μm above the substrate. The initial position of the free-stream cell was 13 μm above the substrate and 9 μm upstream of its adherent counterpart (centroidal separation distance ~ 12 μm). Simulations involving out of plane collisions at glancing distances (δy) of 2, 3.5, 5 and 6.5 μm were performed at a shear rate of 100 s^{-1}. The binary interaction for a glancing distance of 2 μm is shown in Figure 5.2 and Z(t) of the free-stream cell for all glancing distances considered is

plotted in Figure 5.3. Figure 5.2 demonstrates that the electrostatic repulsion forces are sufficient to prevent membrane overlap during such interactions.

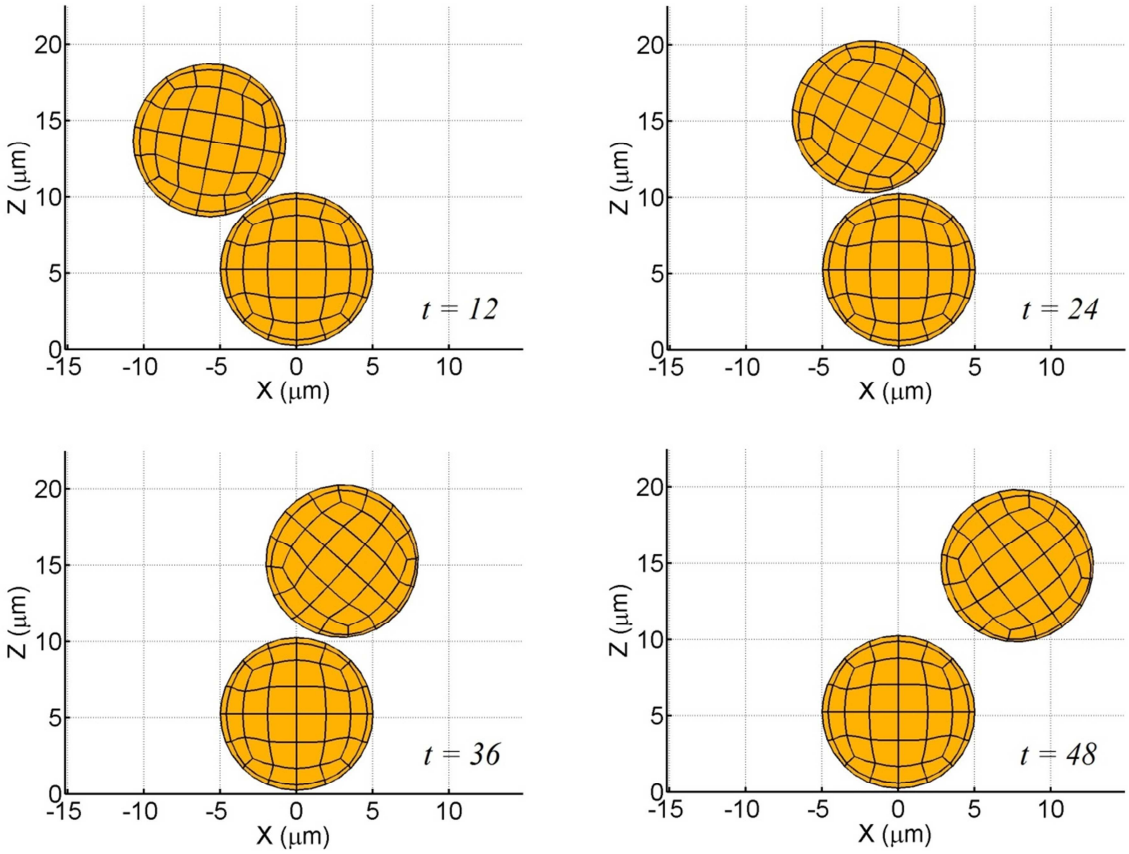

Fig. 5.2 Binary interaction between a firmly adherent, spherical cell and a spherical free-stream cell (δx = -9 μm, δy = 2 μm, δz = 7.75 μm, a = 5 μm, $\dot{\gamma}$ = 100 s^{-1}).

As indicated in Figure 5.3, the apparent "roughness" in the trajectories for glancing distances of 2, 3.5 and 5 μm arises from the repulsion force being non-negligible due to proximity of the cell surfaces. Moreover, for the simulation time considered the vertical displacement of the cells for these cases was greater than its initial position which indicates that such collisions would not be suitable for recruitment. On the other hand, the case involving a 6.5 μm offset revealed a lower influence of the repulsive forces due to minimal surface-surface interference. At the end of the simulation, cell vertical displacement was lower than its initial vertical position above the

wall. These results suggest that binary interactions at glancing distances of ≥ 6.5 μm is suitable for recruitment and are consistent with those predicted by King and Hammer (2001b).

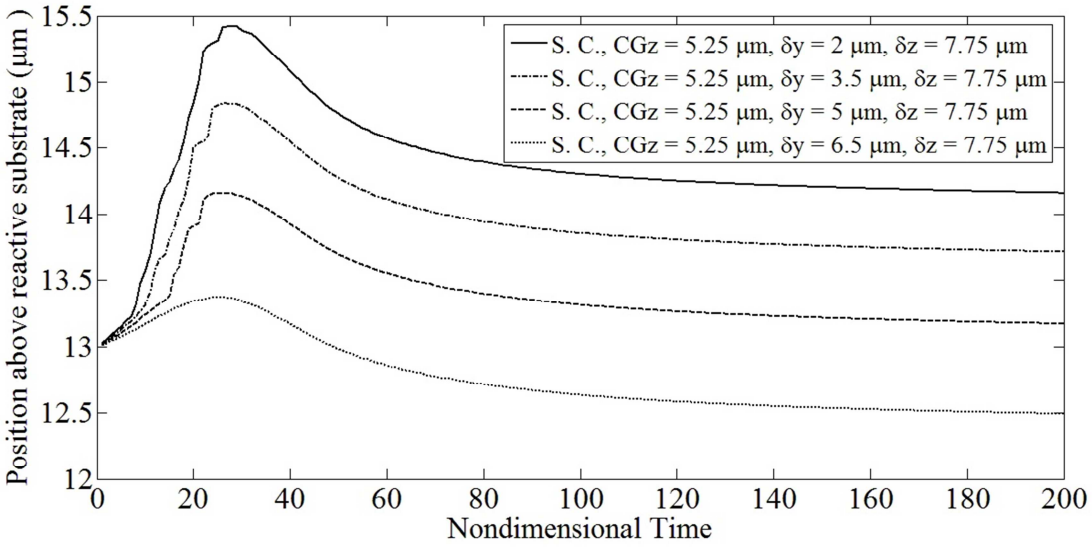

Fig. 5.3 Cell trajectories for binary interactions involving a firmly adherent spherical cell and a spherical free-stream cell with increasing glancing offsets.

In order to facilitate a comparison between rigid and deformable adherent cells, simulations involving moderately and highly deformed adherent cells were performed at glancing distances of 2 and 3.5 μm. The center of gravity for the adherent cells was located at 4.5 and 3.25 μm above the wall for the moderately and highly deformed cells, respectively. The shear rate and the starting position of the free-stream cell were identical to the test cases considered previously. The comparison between the resulting trajectories of the free-stream cells for the 2 μm glance is indicated in Figure 5.4, while that for the 3.5 μm glance is shown in Figure 5.5. For either offset distance, the free-stream cell smoothly passed over the highly deformed cell and descended closer to the reactive substrate. In case of the moderately deformed cell, for an offset of 2 μm the free-stream cell was displaced further away from the reactive substrate. On the

other hand, for a 3.5 μm glance, the free-stream cell eventually descended closer to the reactive substrate.

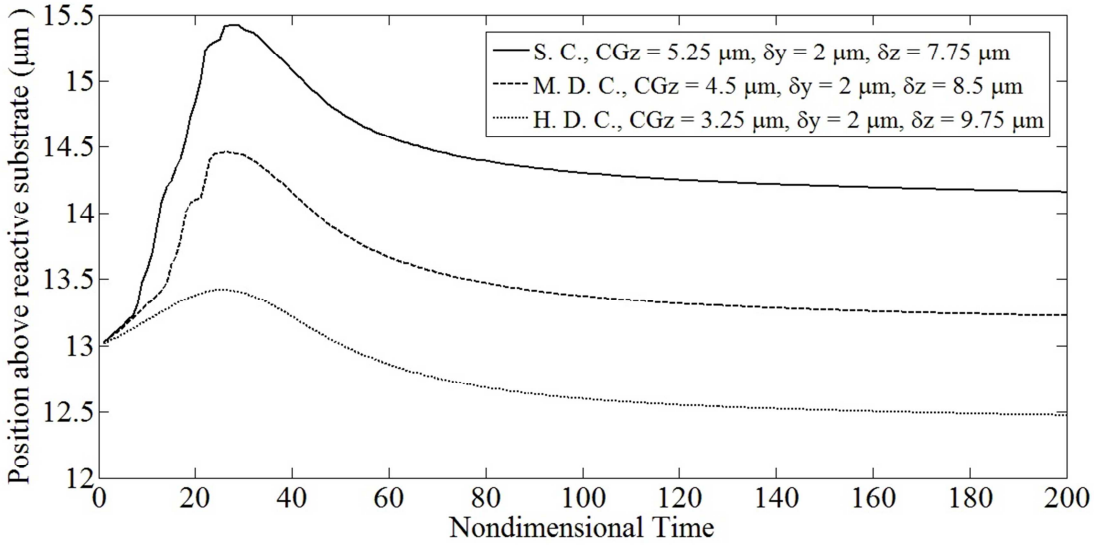

Fig. 5.4 Cell trajectories for binary interactions involving a firmly adherent spherical, moderately or highly deformed adherent cell and a spherical free-stream cell for a fixed CGz (13 μm) & fixed δ*y* (2 μm).

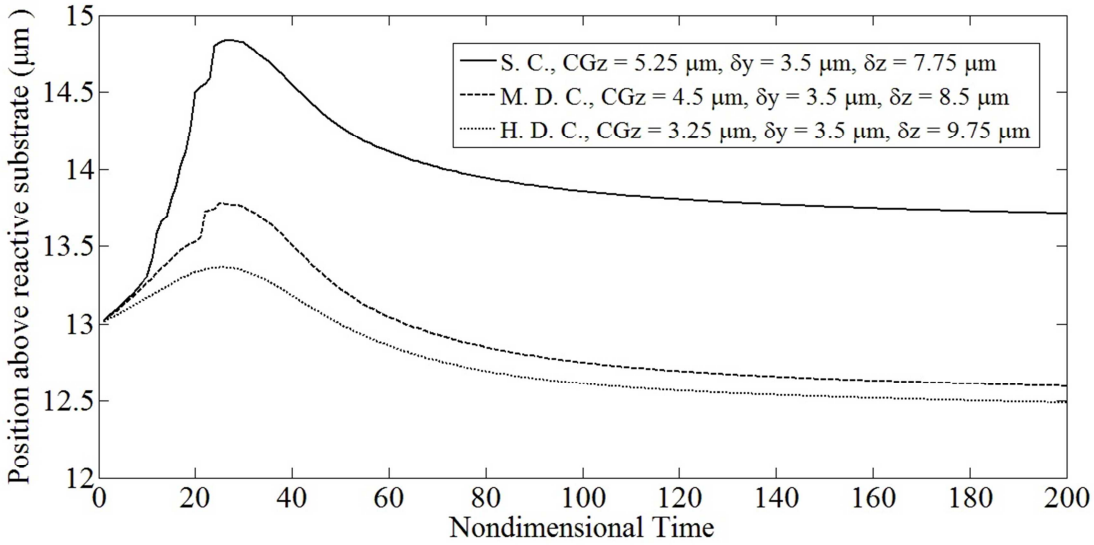

Fig. 5.5 Cell trajectories for binary interactions involving a firmly adherent spherical, moderately or highly deformed adherent cell and a spherical free-stream cell for a fixed CGz (13 μm) & fixed δ*y* (3.5 μm).

This indicates that for the same initial position of the free-stream cell, binary collisions with deformed adherent cells drives the free-stream cell closer to the substrate for small glancing distances. The shapes of these trajectories illustrate the domain of influence of adherent cells or obstructions whose shapes deviate from a spherical morphology.

II. Effect of membrane separation distance for moderately deformed adherent cell

Note that as the vertical CG of the free-stream cell is fixed and the adherent cell changes from spherical to moderately or highly deformed, the initial membrane separation distance increases, possibly affecting the simulation results.

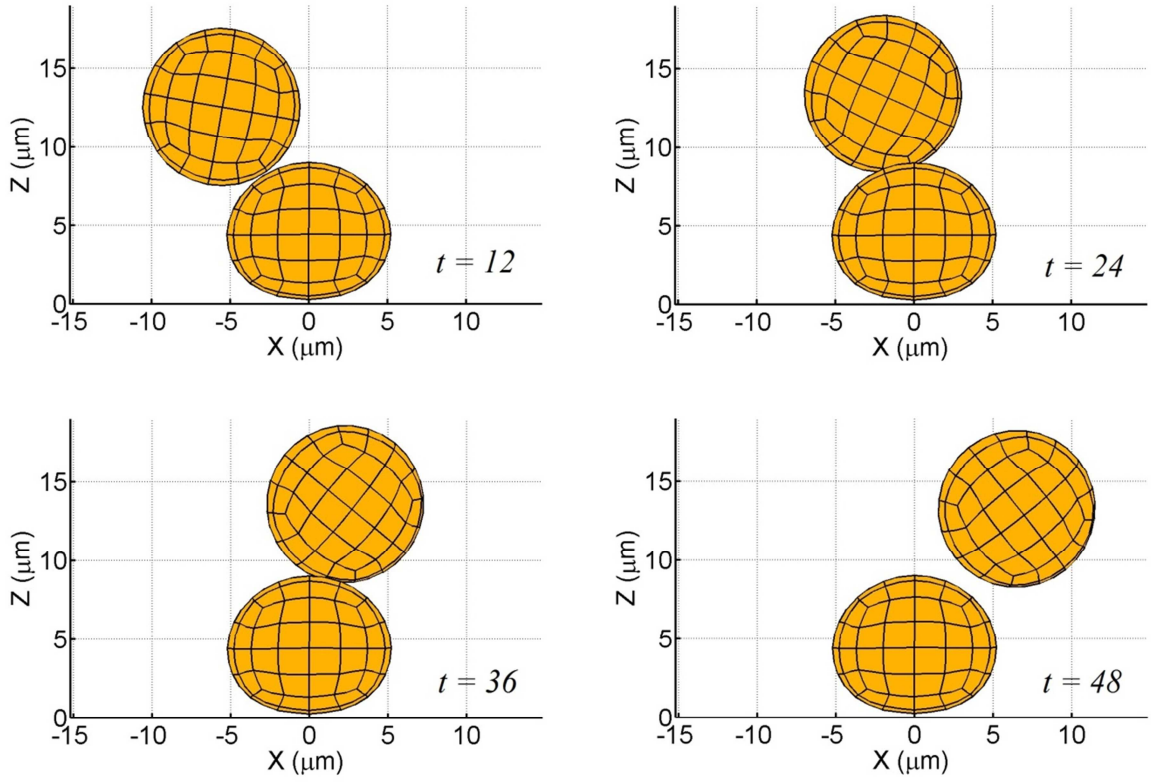

Fig. 5.6 Binary interactions between a firmly adherent, moderately deformed cell and a spherical free-stream cell (δx = -9 μm, δy = 3.5 μm, δz = 7.75 μm, a = 5 μm, $\dot{\gamma}$ = 100 s^{-1}).

In order to maintain similar membrane separations as for the spherical case, the initial displacement of the free-stream cell was brought down to 12.25 μm above the substrate. A stationary, adherent, moderately deformed cell was maintained at CGz = 4.5 μm and the frees-tream cell was located 9 μm upstream of the adherent cell. A series of simulations involving glancing collisions with δy = 3.5, 5 and 6.5 μm were performed at a shear rate of 100 s^{-1}. Note, for $\delta y \geq 10$ μm, there is no membrane overlap between the adherent and free-stream cells. The binary interaction for a glance of 3.5 μm is indicated in Figure 5.6 and the resulting trajectories of the free-stream cell are shown in Figure 5.7. In Figure 5.6, the apparent intersection of the cell membranes is observed at lateral (Y-direction) centroidal offsets of 3.5 and 5 μm. In actuality, no membrane overlap occurs as the free-stream cell is passing behind and over the adherent cell. As may be seen in Figure 5.7, the free-stream cell descended closer to the substrate for δy = 5, 6.5 μm as compared to the corresponding cases for binary interactions with a spherical adherent cell (Fig. 5.3).

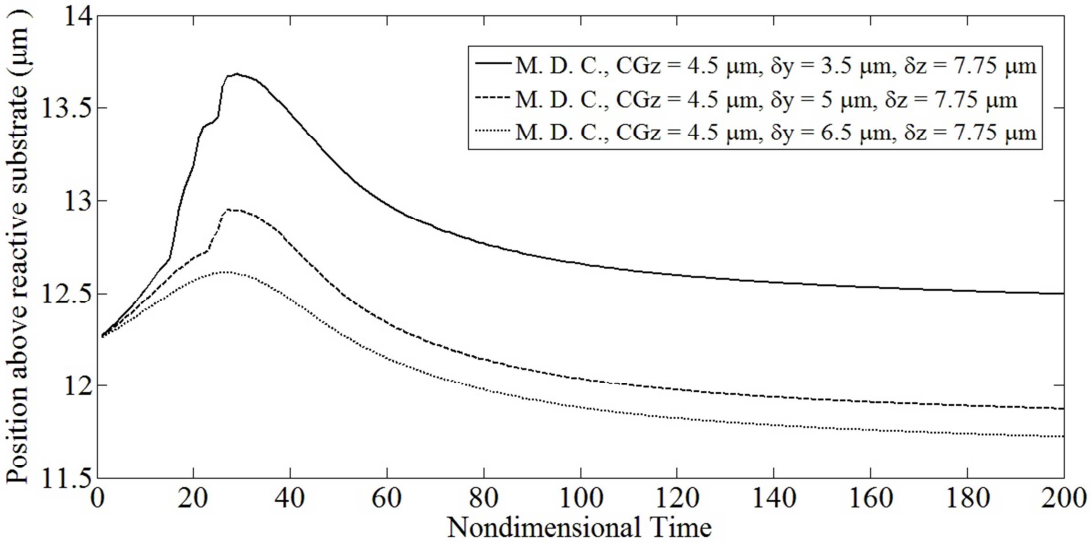

Fig. 5.7 Cell trajectories for binary interactions involving a firmly adherent moderately deformed cell and a spherical free-stream cell with increasing glancing offsets.

III. Effect of membrane separation distance for highly deformed adherent cell

For a highly deformed adherent cell (CGz = 3.25 μm), in order to maintain a similar membrane separation as the previous two cases, the initial displacement of the free-stream cell was brought down to 11 μm above the wall. As before, the free-stream cell was located 9 μm upstream of the adherent cell. A series of simulations involving glancing collisions with δy = 3.5, 5 and 6.5 μm were performed at a shear rate of 100 s^{-1}. The binary interaction for a glancing distance of 3.5 μm is indicated in Figure 5.8 and the resulting cell trajectories are illustrated in Figure 5.9.

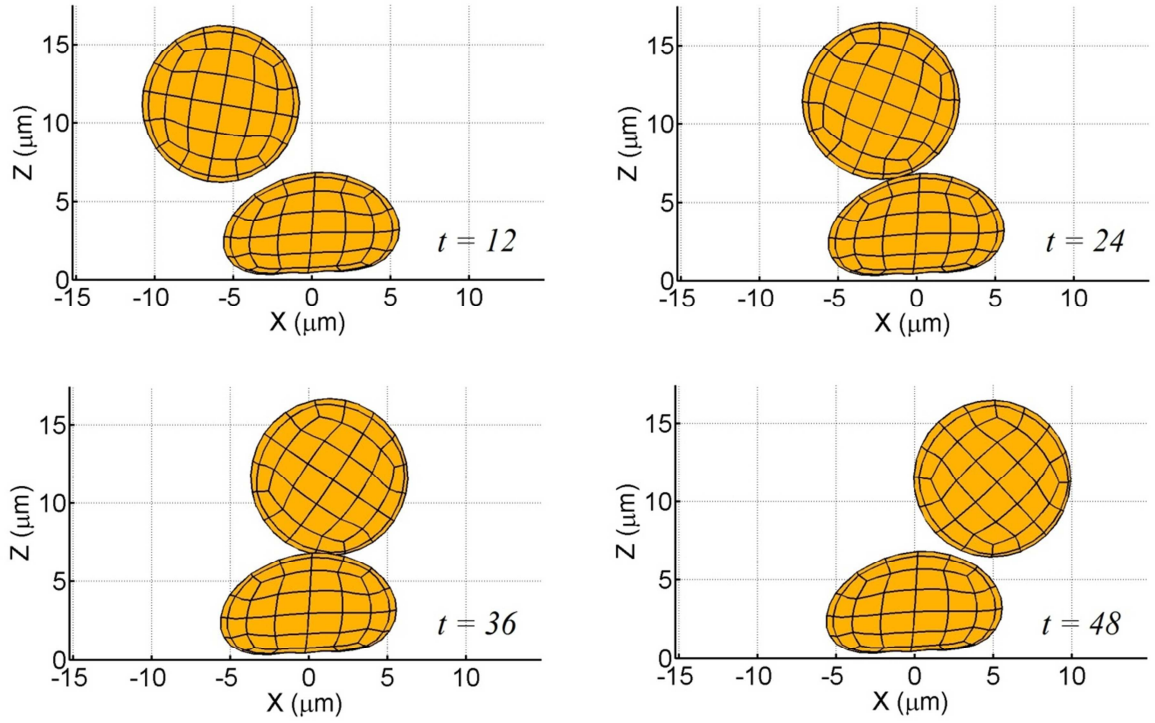

Fig. 5.8 Binary interactions between a firmly adherent, highly deformed cell and a spherical free-stream cell (δx = -9 μm, δy = 3.5 μm, δz = 7.75 μm, a = 5 μm, $\dot{\gamma}$ = 100 s^{-1}).

As compared to the previous two scenarios, the roughness in the trajectory plot is observed only for the simulation involving a δy = 3.5 μm offset. Note that the cell was displaced vertically (i.e., Z direction) by a smaller amount as compared to the scenario involving a spherical, adherent cell

and approached closer to the substrate following the interaction. For the cases involving 5 and 6.5 μm offsets, the observed trajectories were similar to the previous scenario involving moderately deformed cells. Moreover, the trajectories of a cell undergoing binary collisions with a highly deformed cell at various offset distances appear to be favorable, from the point of secondary recruitment, since the free-stream cell, post collision, descends closer to the substrate.

Furthermore, glancing collisions at a 6.5 μm offset resulted in a nearly identical reduction in the Z position (i.e., ~500 nm) for the scenarios involving spherical, moderately deformed and highly deformed adherent cells. This indicates that with increasing offset in the lateral direction, the profile of the streamlines around a spherical obstruction nearly coincided with ones corresponding to an arbitrary shape. In the absence of repulsion, the trajectory of an infinitesimal free-stream cell would coincide with streamlines around the obstruction (King and Hammer (2001b)).

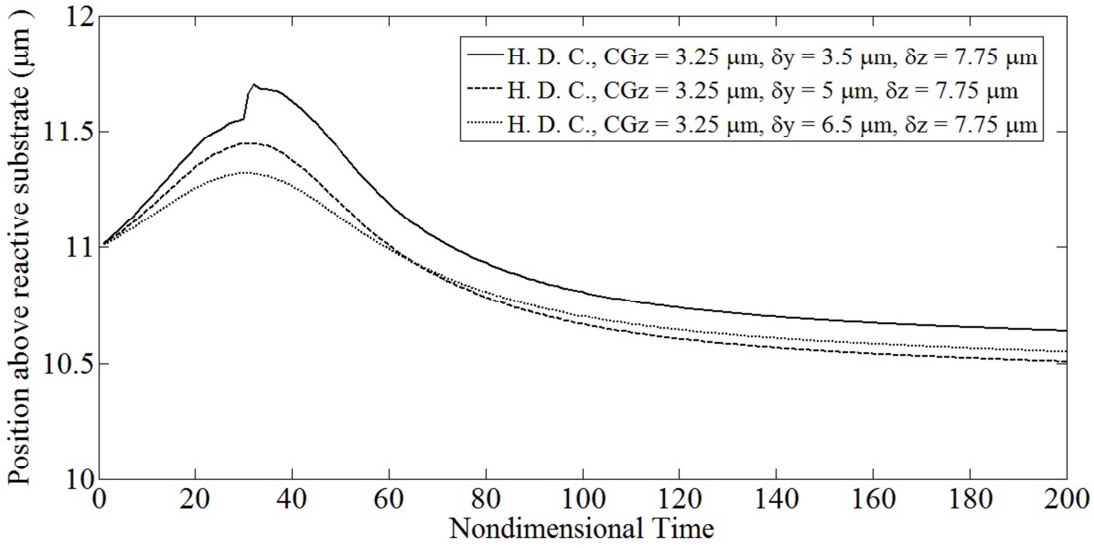

Fig. 5.9 Cell trajectories for binary collisions involving a firmly adherent highly deformed cell and a spherical free-stream cell with increasing glancing offsets.

The primary goal of running these simulations was to predict glancing distances and cell morphologies that were most favorable for an alternative form of secondary recruitment involving 'rolling over' of the free-stream cell as described by Paschall and Lawrence (2008). These simulations indicate that for the same membrane separation, binary interactions occurring at a glancing distance (i.e., δy) of $\geq$ 6.5 μm is most favorable for recruitment. With increasing deformation of adherent cells, collisions occurring at lower glancing distances resulted in the free-stream cells to be driven towards the reactive substrate.

5.3.2. Effect of multiple binary collisions with two moderately deformed adherent cells (free-stream cell at least one cell diameter above substrate)

During inflammatory response, a free-stream cell is likely to interact with many rolling or adherent cells. In order to study the influence of a recruited cell (predecessor) on a free-stream cell (successor) undergoing binary collisions with the recruiting cell, a second deformed cell was fixed to the substrate 30 μm downstream and the effect of 2 obstructions on the trajectory of the free-stream cell was observed.

I. Collisions with two moderately deformed adherent cells

Two in-plane, moderately deformed cells were spaced 30 μm apart with CGz = 4.5 μm for both adherent cells. The initial X-displacement of the free-stream cell was 9 μm upstream of the first adherent cell (i.e. CGx = -9 μm) with CGz = 12.25 μm.

Two simulations involving glancing distances of 3.5 and 6.5 μm were performed. A snapshot from the simulation involving an offset of 3.5 μm is shown in Figure 5.10 and the corresponding trajectories of the free-stream cell are illustrated in Figure 5.11.

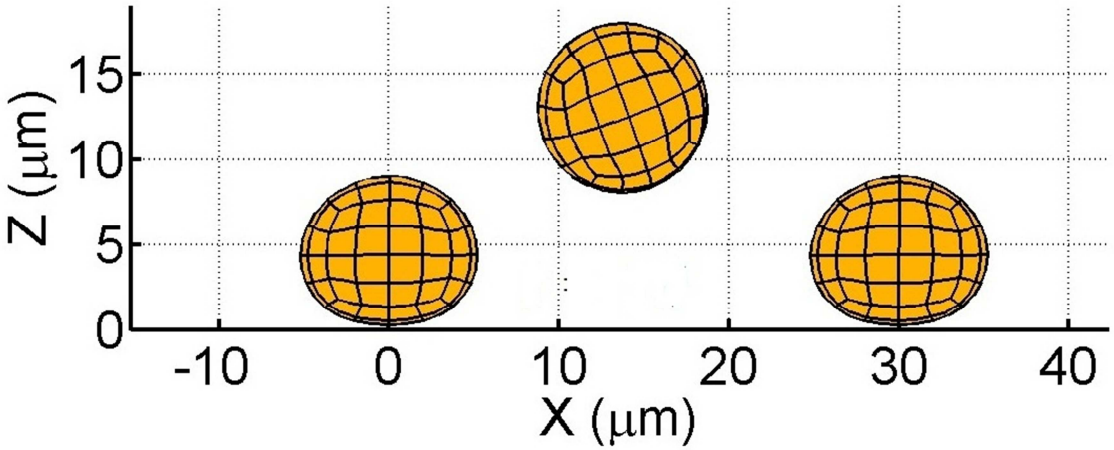

Fig. 5.10 Collisions involving two firmly adherent, moderately deformed cells and a spherical free-stream cell (δy = -9 μm, δz = 7.75 μm, a = 5 μm, $\dot{\gamma}$ = 100 s^{-1}).

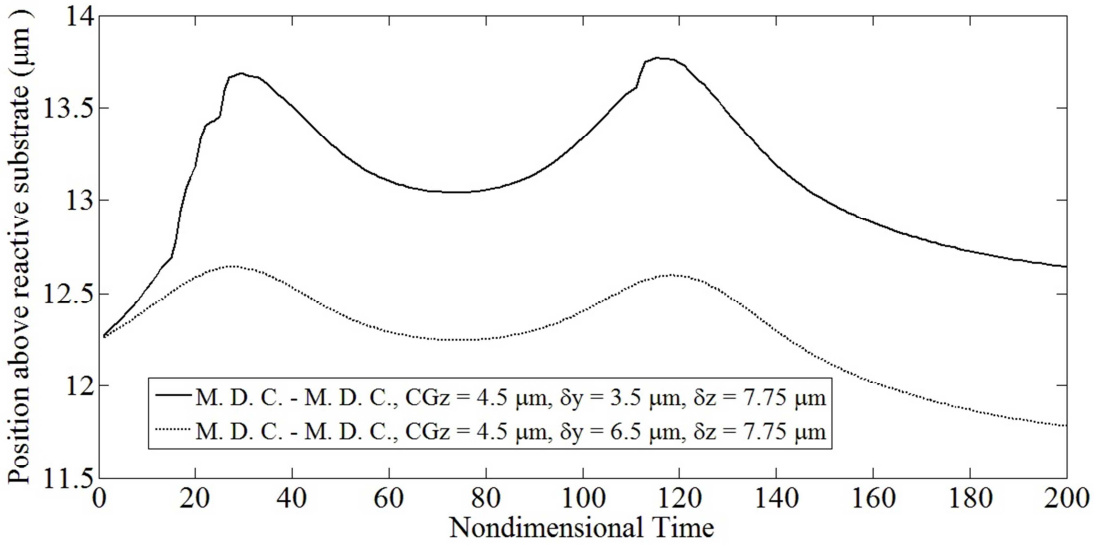

Fig. 5.11 Cell trajectories for binary interactions involving two firmly adherent, moderately deformed cells and a spherical free-stream cell for various glances.

The two "peaks" indicate instances of repulsion in the trajectory. Upon comparison with the trajectory for a binary collision with a single adherent cell, it was observed that the final particle elevation for the free-stream cell for a sequence of binary collisions was slightly higher, by 60 - 150 nm, at the end of the simulation. The slope of the trajectory (i.e., dZ/dt) for δy = 6.5 μm is non-zero unlike the corresponding trajectory for binary interactions involving a single

moderately deformed adherent cell (Fig. 5.7). This suggests that the free-stream cell would continue to descend towards the reactive substrate downstream of the second cell.

II. Collisions with two highly deformed adherent cells

Two in-plane, highly deformed, adherent cells were spaced 30 μm apart with CGz = 3.25 μm for both adherent cells. The initial X-displacement of the free-stream cell was 11 μm above the substrate and 9 μm upstream of the first adherent cell. Simulations similar to the previous scenario for two moderately deformed adherent cells were performed and the trajectories of the free-stream cell are plotted in Figure 5.12.

Upon comparison with the trajectory for a binary collision with a single adherent cell, it was observed that the final particle elevation for a sequence of binary collisions was slightly higher, by 90 - 170 nm, at the end of the simulation. Unlike the nearly asymptotic trajectories for binary interactions involving a single highly deformed adherent cell (Fig. 5.9), the trajectories in

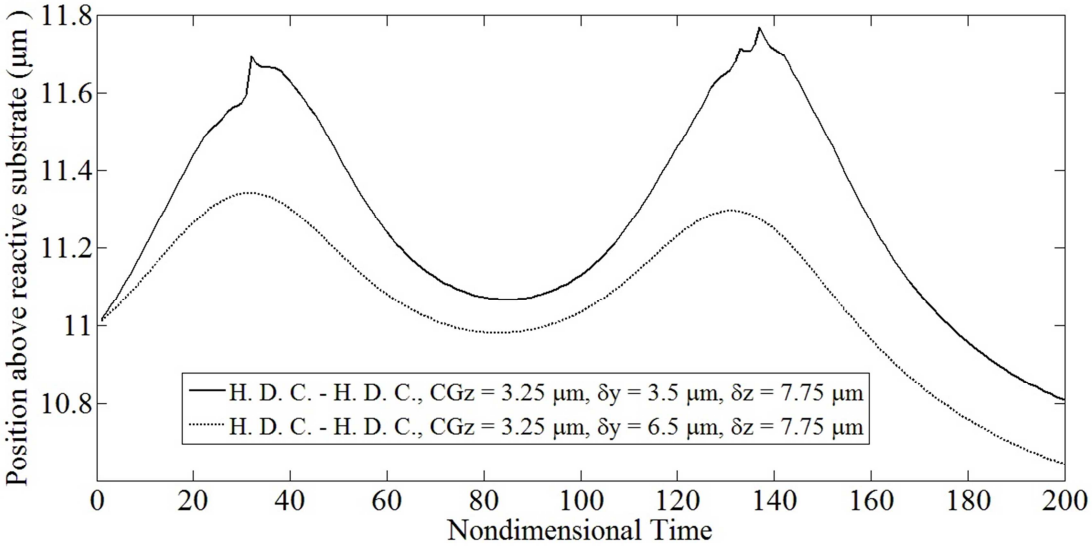

Fig. 5.12 Cell trajectories for binary interactions involving two firmly adherent, highly deformed cells and a spherical free-stream cell for various glances.

the present scenario suggest that the cell would continue its descent towards the reactive substrate. The trajectory plots from the preceding two scenarios indicate that the presence of a second cell attached three diameters downstream of the primary cell drives the free-stream cell towards the substrate.

One of the motives for simulating test cases away from the wall was to assess the ability of the code to generate a disturbed flow field around protruberances of arbitrary shapes. Besides, the effectiveness of the Gram-Schmidt orthonormalization is illustrated from the shapes of the trajectories of cells flowing in the vicinity of the obstruction. The results from the simulations in Section 5.3.1 suggests that with increasing levels of deformation and glancing distances, free-stream cells are driven towards the reactive substrate. A sequence of binary interactions results in the free-stream cells to be driven closer to the reactive substrate as compared to collisions involving a single adherent cell.

5.3.3. Binary collisions (free-stream cell less than a diameter above substrate)

In Sections 5.3.1 and 5.3.2, the glancing distance that is most favorable for recruitment was assessed where it was found that for $\delta y \geq 6.5$ μm, the free-stream cell descended towards the substrate. In the present and subsequent sections, we will present and discuss results for free-stream cells initially closer to the substrate (while the offset distance between the free-stream and adherent cell is fixed).

Two sets of simulations for free-stream cell elevations of 7.5 and 6 μm were performed at shear rates of 100 s^{-1}. A glancing distance of 10.5 μm was maintained in all the simulations in order to negate the effects of trajectory changes stemming from cell-cell repulsion and thereby assess the effect of streamlines around the adherent cell on the trajectory of the free-stream cell.

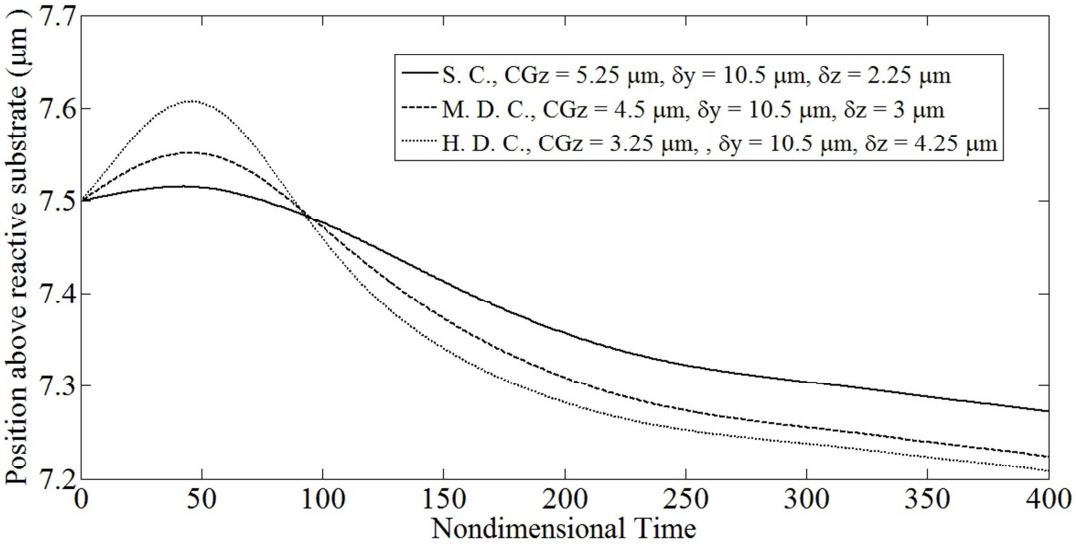

Fig. 5.13 Cell trajectories for binary interactions involving a firmly adherent spherical, moderately or highly deformed adherent cell and a spherical free-stream cell (CGx = -9 μm, CGy = 10.5 μm, CGz = 7.5 μm, a = 5 μm, $\dot{\gamma}$ = 100 s^{-1}).

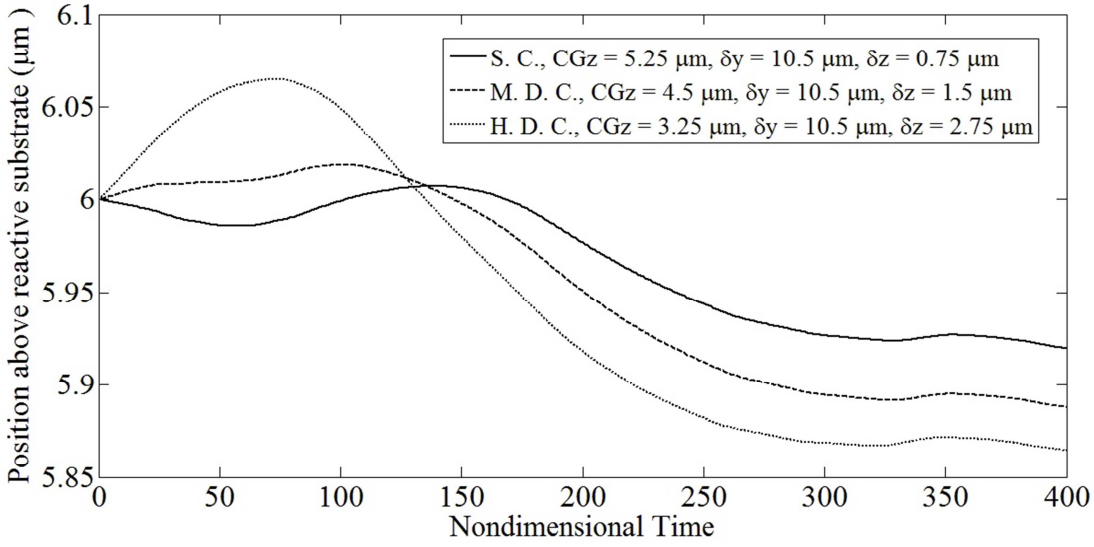

Fig. 5.14 Cell trajectories for binary interactions involving a firmly adherent spherical, moderately or highly deformed adherent cell and a spherical free-stream cell (CGx = -9 μm, CGy = 10.5 μm, CGz = 6 μm, a = 5 μm, $\dot{\gamma}$ = 100 s^{-1}).

The free-stream cell was maintained 9 μm upstream of the adherent cell and simulations involving spherical, moderately and highly deformed cells were studied. The resulting particle

trajectories are illustrated in Figure 5.13 for an initial elevation of 7.5 μm, and Figure 5.14 for an initial elevation of 6 μm. Figure 5.13 indicates that for binary interactions with a moderately deformed cell, the free-stream cell was lifted off by 50 nm following which it descended to an elevation that was 275 nm lower than its starting height. The corresponding values for interactions with a highly deformed cell were 100 and 290 nm, respectively. On the other hand, for collisions with the spherical cell, the upward movement experienced by the free-stream cell was negligible and it subsequently descended to a height that was lower by 230 nm. Figure 5.14 indicates that for the highly deformed case, the free-stream cell was lifted off by 70 nm while the same for the spherical and moderately deformed cell was almost negligible. The cell eventually dropped by heights of 90, 120 and 140 nm for binary interactions with a spherical, moderately deformed, and highly deformed adherent cells, respectively. Although these displacements are small, they are indicative of the effectiveness of an adherent cell to drive a free-stream cell closer to the reactive substrate. The final elevations also suggest that binary collisions with deformed cells could potentially cause the free-stream cell to contact the endothelium nearer to the adherent cell.

The streamlines around a protruberance in the lateral or Y direction are influenced by the shape of the obstruction. In order to illustrate this, the lateral displacement of the free-stream cell i.e. Y(t) is plotted for binary collisions of a free-stream cell (initial CGz = 6 μm) with spherical, moderately and highly deformed adherent cells (Fig. 5.15). These plots are representative of the flow field as observed in the top view or X-Y plane. For a deformed adherent cell, the interfacial compression arising out of adhesion (Section 4.2), results in cell spreading in the Y direction. As observed in Figure 5.15, at nondimensional time ~ 50, the free-stream cell is displaced to a larger

extent in the lateral direction while interacting with deformed adherent cells as compared to binary collisions involving spherical adherent cells.

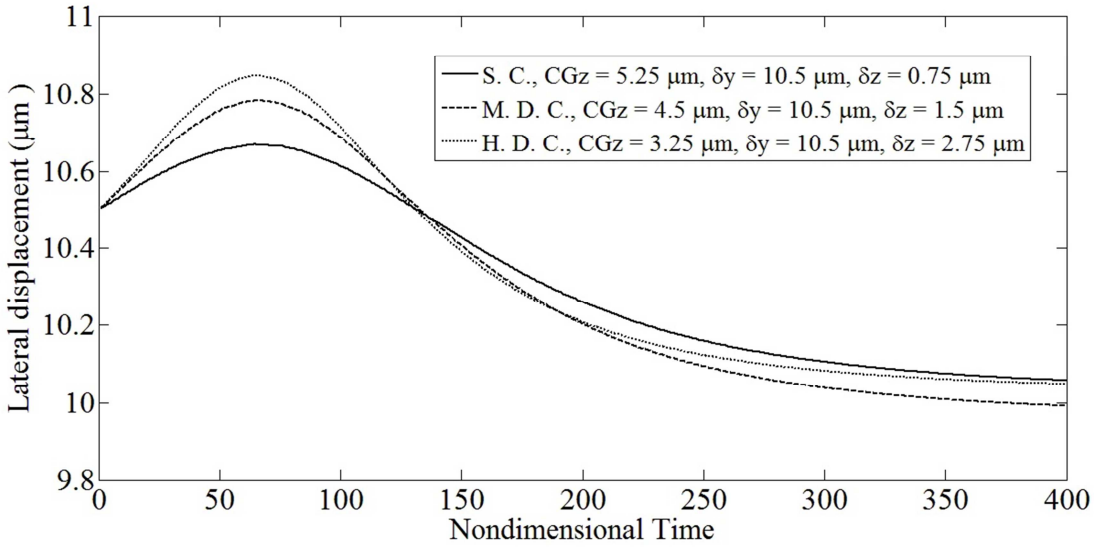

Fig. 5.15 Lateral displacement of cells for binary interactions involving a firmly adherent spherical, moderately or highly deformed adherent cell and a spherical free-stream cell (CGx = -9 μm, CGy = 10.5 μm, CGz = 6 μm, a = 5 μm, $\dot{\gamma}$ = 100 s^{-1}).

In order to test the validity of the claim that effectiveness of secondary capture was profile dependant, some additional simulations were performed. While most of the setup was retained from the previous test case, the shear rate was varied and the cells were made neutrally buoyant.

I. Influence of Shear Rate

All other things being equal, with increasing shear rate, particle deformation increases, and vice versa. Subsequently, the particle shape is altered and its center of gravity is either lowered (for higher shear rates) or raised (for lower shear rates) (Dong et al. (1999)). Meshes for moderate and highly deformed cells were generated for shear rates of 80 s^{-1} and 120 s^{-1}. Simulations for a

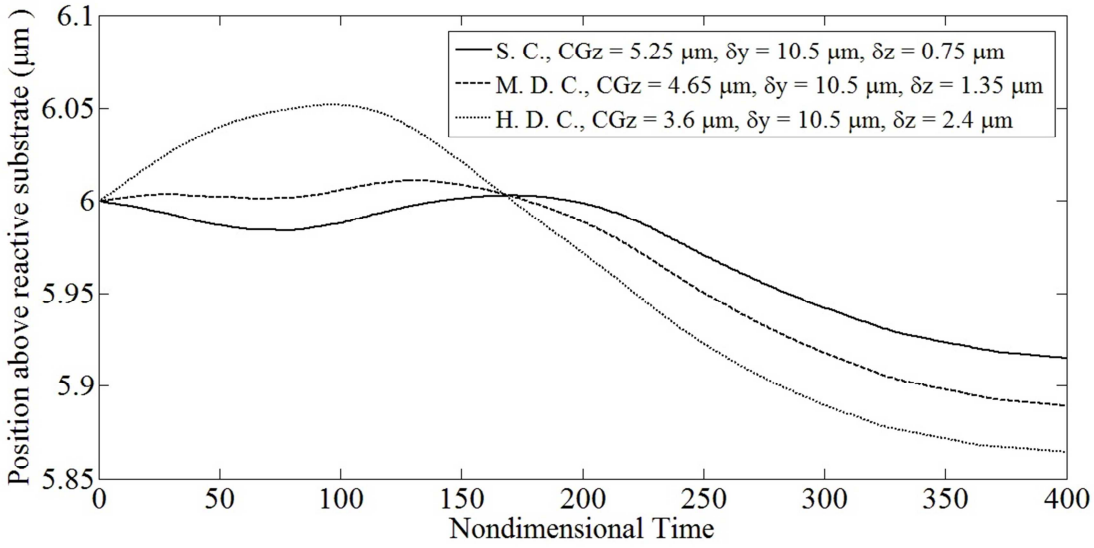

Fig. 5.16 Cell trajectories for binary interactions involving a firmly adherent spherical, moderately or highly deformed adherent cell and a spherical free-stream cell (CGx = -9 μm, CGy = 10.5 μm, CGz = 6 μm, a = 5 μm, $\dot{\gamma}$ = 80 s^{-1}).

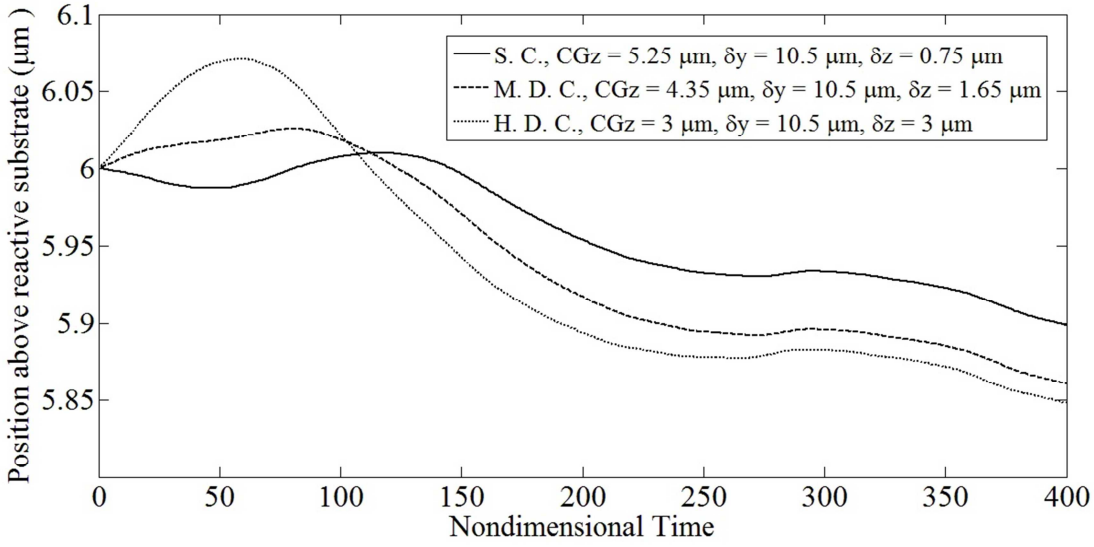

Fig. 5.17 Cell trajectories for binary interactions involving a firmly adherent spherical, moderately or highly deformed adherent cell and a spherical free-stream cell (CGx = -9 μm, CGy = 10.5 μm, CGz = 6 μm, a = 5 μm, $\dot{\gamma}$ = 120 s^{-1}).

free-stream cell elevation of 6 μm were performed and the resulting free-stream cell trajectories are illustrated in Figure 5.16-17 for shear rates of 80 s^{-1} and 120 s^{-1}, respectively.

It was observed that at lower shear rates, the free-stream cell was displaced by a smaller value as compared to the corresponding displacement at higher shear rates. With the above exception, the trends were more or less similar to the baseline case involving a free-stream cell with initial CGx = -9 μm, CGz = 6 μm at a shear rate of 100 s^{-1} and δy = 10.5 μm (Fig. 5.14). In both cases, the highly deformed cell was the most effective "recruiter". Thus, the deformed cell shape continued to significantly impact recruitment, irrespective of shear rate.

II. Influence of Buoyancy

In order to assess the role of gravity in driving the cell towards the wall, the cell density was made equivalent to the surrounding plasma density and test cases were studied at a shear rate of 100 s^{-1}, while retaining the rest of the setup. The resulting trajectories of a free-stream cell flowing at a height of 6 μm are indicated in Figure 5.18. The cell descended by 40, 65 and 90 nm

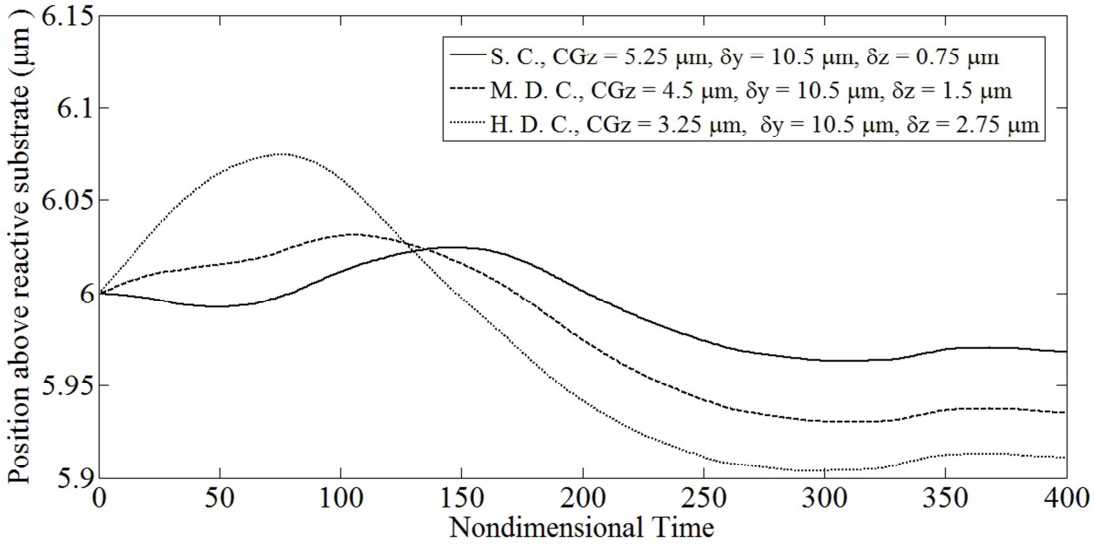

Fig. 5.18 Cell trajectories for binary interactions involving a firmly adherent spherical, moderately or highly deformed adherent cell and a neutrally buoyant spherical free-stream cell (CGx = -9 μm, CGy = 10.5 μm, CGz = 6 μm, a = 5 μm, $\dot{\gamma}$ = 100 s^{-1}).

following collisions with spherical, moderately deformed and highly deformed cells, respectively. This indicates that although gravity assists sedimentation, the cell trajectory following binary collision is more significantly influenced by the shape of the obstruction. Moreover, the similarity in the trends enables one to conclude that the highly-deformed cell continues to be the most effective recruiter, even under conditions of neutral buoyancy.

The domain of influence of the adherent cells was assessed by increasing the glancing distances to 15 and 25 μm, while retaining the initial position of the free-stream cell (shear rate = 100 s^{-1}). Figure 5.19-20 indicate the resulting trajectories of the free-stream cell. For a glancing distance of 15 μm (Fig. 5.19), while the trajectories corresponding to binary collisions with spherical and moderately deformed adherent cells followed a trend similar to that for a 10.5 μm glance (Fig. 5.14), the cells descended by only 80-100 nm. For binary collisions with a

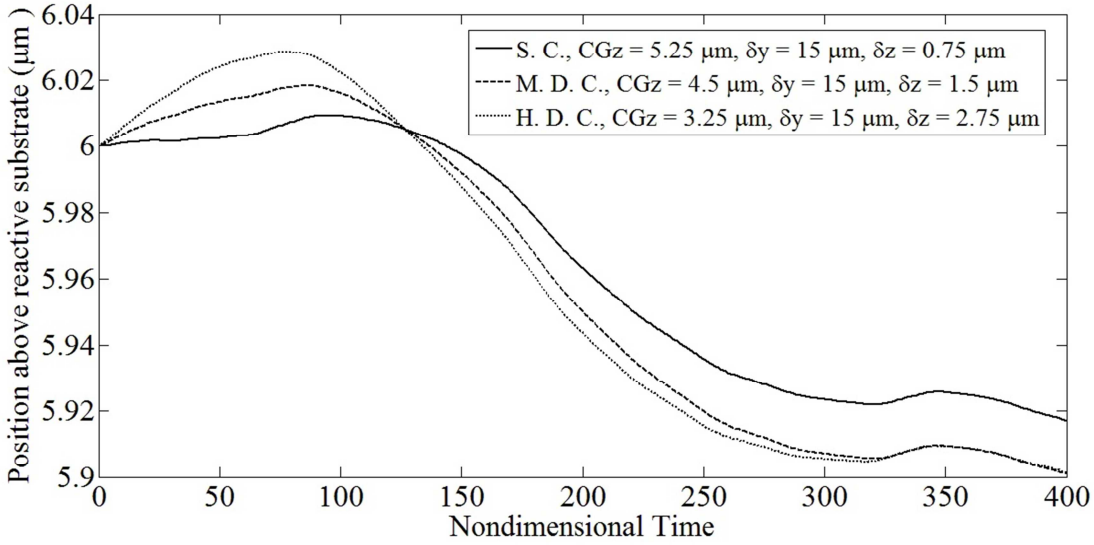

Fig. 5.19 Cell trajectories for binary interactions involving a firmly adherent spherical, moderately or highly deformed adherent cell and a spherical free-stream cell (CGx = -9 μm, CGy = 15 μm, CGz = 6 μm, a = 5 μm, $\dot{\gamma}$ = 100 s^{-1}).

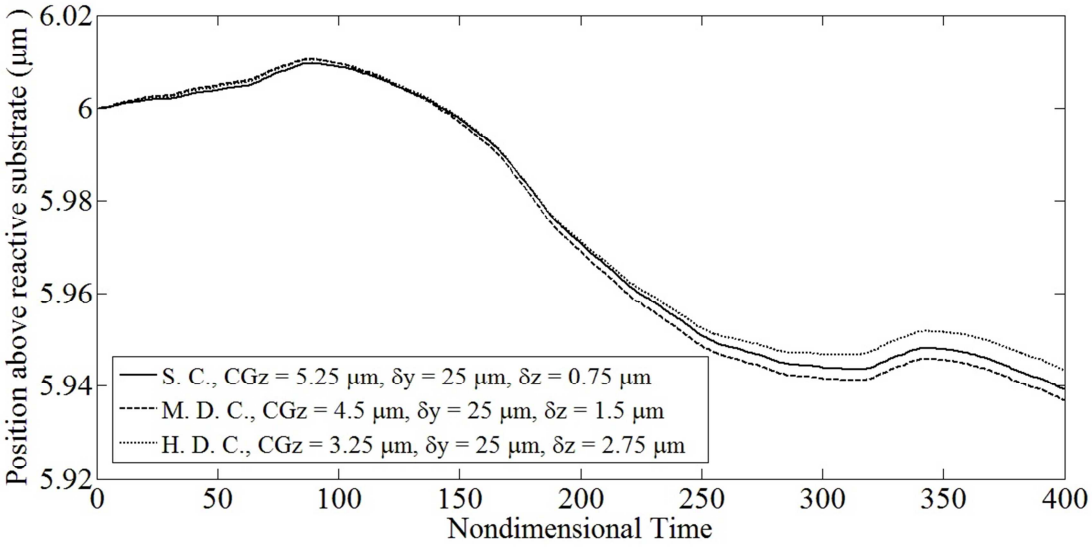

Fig. 5.20 Cell trajectories for binary interactions involving a firmly adherent spherical, moderately or highly deformed adherent cell and a spherical free-stream cell (CGx = -9 μm, CGy = 25 μm, CGz = 6 μm, a = 5 μm, $\dot{\gamma}$ = 100 s^{-1}).

highly deformed adherent cell, the descent of the free-stream cell nearly coincided with that for a moderately deformed cell. For an offset distance of 25 μm, the trajectory of the free-stream cell was nearly independent of the shape of the adherent cell (Fig. 5.20) implying that with an increasing glance, the adherent cell morphology has little impact on the trajectory of free-stream cells. Moreover, the free-stream cell descended by 55-65 nm indicating that the strength of the disturbance flow-field decreases with increasing distance from the source.

The results from the test cases discussed in this section suggest that for a fixed glancing distance, binary interactions involving highly deformed adherent cells present the most favorable scenario for recruitment of free-stream cells. Although variations in the shear rate and cell buoyancy are found to affect the free-stream cell trajectories, adherent cell deformation significantly impacts the process of secondary recruitment. Moreover, for offset distances ≥ 5

times the cell radius, the trajectories of the free-stream cells is independent of adherent cell shapes.

6 CONCLUSIONS AND FUTURE DIRECTIONS

This thesis presented a different perspective in computational biology through boundary element techniques. Results of the treading simulation reinforced the validity of the kernel functions for the relevant computational domains and were in good agreement with similar studies conducted in the field of emulsions and biorheology. While neutrally buoyant particles translated almost parallel to the wall, dense particles appeared to drift towards the wall. Besides, the Jeffrey's orbit for spheroid inclusions was slightly modified as compared to an unbounded shear flow. Deformable and initially spherical particles were found to exhibit a tank treading motion (Section 2.3) while initially spheroid particles were shown to portray either a tumbling motion or a trembling motion that was dependant on the aspect ratio and the viscous number (Section 2.3, Appendix B). When the hydrodynamic forces were much smaller compared to the elastic restoring forces, the transition to the breathing mode occurred at higher aspect ratio. Conversely the swinging mode was observed at lower aspect ratios when the viscous number was doubled. Moreover, a linear elastic constitutive model was sufficient to represent the infinitesimal deformations stemming from weak hydrodynamic forces and the transition from tumbling to trembling appeared to be independent of the constitutive model.

Binary collisions between free-stream leukocytes resulted in the free-stream cells being driven closer to the substrate. Moreover, the slight modulation in the contact area offered insights into neutrophil string formations through L-selectin mediated cell-cell adhesion (Section 3.3).

Solitary cell rolling studies indicated that the membrane compliance should be comparable to the bond stiffness in order to be consistent with the theory of linear elasticity and the theory for Hertzian contact. Small deformations resulted in more bonds and potentially

slower rolling amongst compliant cells, as compared to their rigid counterparts (Section 4.3.2). Moreover, cells with smaller diameter were observed to roll slowly, while the inclusion of bonds under compression increased the rolling velocity (Section 4.3.2). These results are particularly significant in the context of the large variability in cell sizes, as well as material properties of the membrane. The drop in translational velocity was observed to be deterministic, albeit for a small fraction of time. Once the upper limit on the bonds (here set to 40) was reached, the variations in rolling velocities and contact area became noisy. Moreover, the number of receptors on the cell could certainly limit the number of bonds formed in an actual physiological scenario. Although these results seem quite feasible, additional test cases would have to be run in order to validate this claim.

Binary collisions between spherical, moderately, or highly deformed, adherent cells and free-stream cells located away from the reactive zone were simulated for several glancing or out of plane offset distances. With increasing offset, the collisions became smoother and the free-stream cell displaced closer to the substrate. The results for the highly deformed adherent cell indicated that the free-stream cell descended closer to the substrate as compared to the moderately deformed or spherical adherent cell, irrespective of the glancing distance (Section 5.3.1). A sequence of binary collisions involving multiple deformable cells showed that although the presence of the second cell altered the final elevation of the free-stream cell, the difference was of the order of nanometers. Although the presence of the second cell appears to be detrimental to recruitment, the slope of the trajectory of the free-stream cell indicates an enhanced descent towards the wall, as compared to single binary interactions (Section 5.3.2). Test cases involving more than two cells were specifically introduced to demonstrate the abilities

of the code. Significantly, one can introduce an infinite number of obstructions to predict the trajectories of free-stream cells.

Binary collisions between adherent and free-stream cells in the proximity of the reactive zone were conducted at a fixed glancing distance that was chosen to avoid the effect of repulsive forces and assess the domain of influence of the obstruction. It was observed that a slight deviation from the spherical morphology had a profound influence on the descent of the free-stream cell and the highly-deformed cell emerged as the most effective recruiter. Moreover, neither shear rate nor gravity was found to significantly impact this trend (Section 5.3.3). Besides, with an increasing glance, the cell trajectory was almost independent of the shape of the adherent cell. Furthermore, the reduced displacement of the free-stream cells implied a vanishing effect of the disturbance flow-field with increasing distance from the source (Section 5.3.3).

Although hydrodynamic recruitment appears to be an important mode of secondary recruitment of leukocytes, it does not correspond to all secondary attachment events. Binary collisions with red blood cells and leukocyte-leukocyte adhesion have also been found to contribute to cell accumulation on activated endothelium. Therefore, one could conclude by stating that although multiple modes of secondary recruitment have been identified, it is difficult to quantify the relative importance of a single mode without inhibiting the other two possibilities. Moreover, the inherent difficulties in measuring the glancing distances either in vivo or in vitro presents an interesting challenge to experimentalists in the field of cell adhesion, thereby necessitating more research in this direction.

Bibliography

Ainley, J., Durkin, S., Embid, R., Boindala, P., Cortez, R., 2008. The method of images for regularized Stokeslets. J Comput Phys 227, 4600-4616.

Alon, R., Hammer, D.A., Springer, T.A., 1995. Lifetime of the P-selectin-carbohydrate bond and its response to tensile force in hydrodynamic flow. Nature 374, 539-542.

Argenbright, L.W., Letts, L.G., Rothlein, R., 1991. Monoclonal antibodies to the leukocyte membrane CD18 glycoprotein complex and to intercellular adhesion molecule-1 inhibit leukocyte-endothelial adhesion in rabbits. J Leukocyte Biol 49, 253-257.

Bell, G., 1978. Models for the specific adhesion of cells to cells. Science 200, 618-627.

Blake, J., Chwang, A., 1974. Fundamental singularities of viscous flow. J Eng Math 8, 23-29.

Blake, J.R., 1971. A note on the image system for a stokeslet in a no-slip boundary. Math Proc Cambridge 70, 303-310.

Blyth, M.G., Pozrikidis, C., 2006. Film flow down an inclined plane over a three-dimensional obstacle. Phys Fluids 18, 052104.

Bretherton, F.P., 1962. The motion of rigid particles in a shear flow at low Reynolds number. J Fluid Mech 14, 284-304.

Brooks, S.B., Tozeren, A., 1996. Flow past an array of cells that are adherent to the bottom plate of a flow channel. Comput Fluids 25, 741-757.

Chang, Y.-I., Wang, Y.-F., 1998. A preliminary study on the initial elastic adhesion behavior of leucocytes. Colloid Surface A 140, 395-401.

Chen, S., Springer, T.A., 1999. An Automatic Braking System That Stabilizes Leukocyte Rolling by an Increase in Selectin Bond Number with Shear. J Cell Biol 144, 185-200.

Cozens-Roberts, C., Quinn, J.A., Lauffenberger, D.A., 1990. Receptor-mediated adhesion phenomena. Model studies with the Radical-Flow Detachment Assay. Biophys J 58, 107-125.

Davis, R.H., Serayssol, J.-M., Hinch, E.J., 1986. The elastohydrodynamic collision of two spheres. J Fluid Mech 163, 479-497.

Decuzzi, P., Ferrari, M., 2006. The adhesive strength of non-spherical particles mediated by specific interactions. Biomaterials 27, 5307-5314.

Dong, C., Cao, J., Struble, E.J., Lipowsky, H.H., 1999. Mechanics of leukocyte deformation and adhesion to endothelium in shear flow. Ann Biomed Eng 27, 298-312.

Dong, C., Lei, X., 2000. Biomechanics of cell rolling: shear flow, cell-surface adhesion, and cell deformability. J Biomech 33, 35–43.

Evans, E., Heinrich, V., Leung, A., Kinoshita, K., 2005. Nano- to microscale dynamics of P-selectin detachment from leukocyte interfaces. I. Membrane separation from the cytoskeleton. Biophys J 88, 2288-2298.

Fröhlich, H., Sack, R., 1946. Theory of the Rheological Properties of Dispersions. P Roy Soc Lond A Mat 185, 415-430.

Gao, T., Hu, H.H., 2009. Deformation of elastic particles in viscous shear flow. J Comput Phys 228, 2132-2151.

Gao, T., Hu, H.H., Castañeda, P.P., 2012. Shape Dynamics and Rheology of Soft Elastic Particles in a Shear Flow. Phys Rev Lett 108, 058302.

Gee, D.J., King, M.R., 2010. Molecular to Multicellular Deformation during Adhesion of Immune Cells Under Flow, Multiscale Modeling of Particle Interactions. John Wiley & Sons, Inc., pp. 341-368.

Goddard, J.D., 1977. An elastohydrodynamic theory for the rheology of concentrated suspensions of deformable particles. J Non-Newton Fluid 2, 169-189.

Goldman, A.J., Cox, R.G., Brenner, H., 1967a. Slow viscous motion of a sphere parallel to a plane wall—I Motion through a quiescent fluid. Chem Eng Sci 22, 637-651.

Goldman, A.J., Cox, R.G., Brenner, H., 1967b. Slow viscous motion of a sphere parallel to a plane wall—II Couette flow. Chem Eng Sci 22, 653-660.

Hammer, D.A., Apte, S.M., 1992. Simulation of cell rolling and adhesion on surfaces in shear flow: general results and analysis of selectin-mediated neutrophil adhesion. Biophys J 63, 35-57.

Hazel, A.L., Pedley, T.J., 2000. Vascular Endothelial Cells Minimize the Total Force on Their Nuclei. Biophys J 78, 47-54.

Hoskins, M.H., Kunz, R.F., Bistline, J.E., Dong, C., 2009. Coupled flow–structure–biochemistry simulations of dynamic systems of blood cells using an adaptive surface tracking method. J Fluid Struct 25, 936-953.

Jadhav, S., Chan, K.Y., Konstantopoulos, K., Eggleton, C.D., 2007. Shear modulation of intercellular contact area between two deformable cells colliding under flow. J Biomech 40, 2891-2897.

Jadhav, S., Eggleton, C.D., Konstantopoulos, K., 2005. A 3-D Computational Model Predicts that Cell Deformation Affects Selectin-Mediated Leukocyte Rolling. Biophys J 88, 96-104.

Jeffery, G.B., 1922. The Motion of Ellipsoidal Particles Immersed in a Viscous Fluid. P Roy Soc Lond A Mat 102, 161-179.

Kadash, K.E., Lawrence, M.B., Diamond, S.L., 2004. Neutrophil String Formation: Hydrodynamic Thresholding and Cellular Deformation during Cell Collisions. Biophys J 86, 4030-4039.

Kantsler, V., Steinberg, V., 2006. Transition to Tumbling and Two Regimes of Tumbling Motion of a Vesicle in Shear Flow. Phys Rev Lett 96, 036001.

Khismatullin, Damir B., Truskey, George A., 2012. Leukocyte Rolling on P-Selectin: A Three-Dimensional Numerical Study of the Effect of Cytoplasmic Viscosity. Biophys J 102, 1757-1766.

Kim, M.B., Sarelius, I.H., 2004. Role of shear forces and adhesion molecule distribution on P-selectin-mediated leukocyte rolling in postcapillary venules. Am J Physiol-Heart C 287, H2705-H2711.

Kinashi, T., Aker, M., Sokolovsky-Eisenberg, M., Grabovsky, V., Tanaka, C., Shamri, R., Feigelson, S., Etzioni, A., Alon, R., 2004. LAD-III, a leukocyte adhesion deficiency syndrome associated with defective Rap1 activation and impaired stabilization of integrin bonds. Blood 103, 1033-1036.

King, M.R., Hammer, D.A., 2001a. Multiparticle Adhesive Dynamics. Interactions between Stably Rolling Cells. Biophys J 81, 799-813.

King, M.R., Hammer, D.A., 2001b. Multiparticle adhesive dynamics: hydrodynamic recruitment of rolling leukocytes. P Natl Acad Sci USA 98, 14919-14924.

King, M.R., Hammer, D.A., 2003. Hydrodynamic Recruitment of Rolling Leukocytes In Vitro. Biophys J 84, 4182.

King, M.R., Heinrich, V., Evans, E., Hammer, D.A., 2005. Nano-to-Micro Scale Dynamics of P-Selectin Detachment from Leukocyte Interfaces. III. Numerical Simulation of Tethering under Flow. Biophys J 88, 1676-1683.

King, M.R., Kim, M.B., Sarelius, I.H., Hammer, D.A., 2003. Hydrodynamic Interactions Between Rolling Leukocytes In Vivo. Microcirculation 10, 401-409.

King, M.R., Rodgers, S.D., Hammer, D.A., 2001. Hydrodynamic Collisions Suppress Fluctuations in the Rolling Velocity of Adhesive Blood Cells. Langmuir 17, 4139-4143.

Kiya, M., Arie, M., 1975. Viscous shear flow past small bluff bodies attached to a plane wall. J Fluid Mech 69, 803-823.

Kunkel, E.J., Ley, K., 1996. Distinct Phenotype of E-Selectin Deficient Mice: E-Selectin Is Required for Slow Leukocyte Rolling In Vivo. Circ Res 79, 1196-1204.

Lebedev, V.V., Turitsyn, K.S., Vergeles, S.S., 2007. Dynamics of Nearly Spherical Vesicles in an External Flow. Phys Rev Lett 99, 218101.

Lee, D., King, M.R., 2006. 12 - Hydrodynamic interactions between cells on reactive surfaces, in: Michael, R.K. (Ed.), Principles of Cellular Engineering. Academic Press, Burlington, pp. 255-IX.

Lee, S.-Y., Ferrari, M., Decuzzi, P., 2009. Design of bio-mimetic particles with enhanced vascular interaction. J Biomech 42, 1885-1890.

Ley, K., Laudanna, C., Cybulsky, M.I., Nourshargh, S., 2007. Getting to the site of inflammation: the leukocyte adhesion cascade updated. Nat Rev Immunol 7, 678-689.

Lim, C.T., Zhou, E.H., Quek, S.T., 2006. Mechanical models for living cells--a review. J Biomech 39, 195-216.

Loewenberg, M., Hinch, E.J., 1997. Collision of two deformable drops in shear flow. J Fluid Mech 338, 299-315.

Melder, R.J., Munn, L.L., Yamada, S., Ohkubo, C., Jain, R.K., 1995. Selectin- and integrin-mediated T-lymphocyte rolling and arrest on TNF-alpha-activated endothelium: augmentation by erythrocytes. Biophys J 69, 2131-2138.

Melder, R.J., Yuan, J., Munn, L.L., Jain, R.K., 2000. Erythrocytes enhance lymphocyte rolling and arrest in vivo. Microvasc Res 59, 316-322.

Misbah, C., 2006. Vacillating Breathing and Tumbling of Vesicles under Shear Flow. Phys Rev Lett 96, 028104.

Mody, N.A., King, M.R., 2005. Three-dimensional simulations of a platelet-shaped spheroid near a wall in shear flow. Phys Fluids 17, 113302.

N'Dri, N.A., Shyy, W., Tran-Son-Tay, R., 2003. Computational Modeling of Cell Adhesion and Movement Using a Continuum-Kinetics Approach. Biophys J 85, 2273-2286.

Nasseri, S., Phan-Thien, N., Fan, X.J., 2000. Lubrication approximation in completed double layer boundary element method. Comput Mech 26, 388-397.

Noguchi, H., Gompper, G., 2007. Swinging and Tumbling of Fluid Vesicles in Shear Flow. Phys Rev Lett 98, 128103.

O'Neill, M.E., 1968. A sphere in contact with a plane wall in a slow linear shear flow. Chem Eng Sci 23, 1293-1298.

Pappu, V., Bagchi, P., 2008. 3D computational modeling and simulation of leukocyte rolling adhesion and deformation. Comput Biol Med 38, 738-753.

Pappu, V., Doddi, S.K., Bagchi, P., 2008. A computational study of leukocyte adhesion and its effect on flow pattern in microvessels. J Theor Biol 254, 483-498.

Paschall, C., Lawrence, M., 2008. L-Selectin Shear Thresholding Modulates Leukocyte Secondary Capture. Ann Biomed Eng 36, 622-631.

Patil, V.R.S., Campbell, C.J., Yun, Y.H., Slack, S.M., Goetz, D.J., 2001. Particle Diameter Influences Adhesion under Flow. Biophys J 80, 1733-1743.

Phan-Thien, N., Fan, X.J., 1995. Traction-based Completed Adjoint Double Layer Boundary Element Method in elasticity. Comput Mech 16, 360-367.

Phan-Thien, N., Fan, X.J., 1996. A boundary integral formulation for elastically deformable particles in a viscous fluid. Z Angew Math Phys 47, 672-694.

Phan-Thien, N., Kim, S., 1994. On the elastic double layer: Some exact solutions and the spectrum on the sphere. J Mech Phys Solids 42, 1177-1197.

Phan-Thien, N., Tullock, D., 1993. Completed double layer boundary element method in elasticity. J Mech Phys Solids 41, 1067-1086.

Phan-Thien, N., Tullock, D., Kim, S., 1992. Completed double layer in half-space: a boundary element method. Comput Mech 9, 121-135.

Power, H., Miranda, G., 1987. Second Kind Integral Equation Formulation of Stokes' Flows Past a Particle of Arbitrary Shape. SIAM J Appl Math 47, 689-698.

Pozrikidis, C., 1995. Finite deformation of liquid capsules enclosed by elastic membranes in simple shear flow. J Fluid Mech 297, 123-152.

Pozrikidis, C., 1997. Shear flow over a protuberance on a plane wall. J Eng Math 31, 29-42.

Pozrikidis, C., 2000. Effect of pressure gradient on viscous shear flow past an axisymmetric depression or protuberance on a plane wall. Comput Fluids 29, 617-637.

Raud, J., Dahlén, S.E., Sydbom, A., Lindbom, L., Hedqvist, P., 1988. Enhancement of acute allergic inflammation by indomethacin is reversed by prostaglandin E2: apparent correlation with in vivo modulation of mediator release. P Natl Acad Sci USA 85, 2315-2319.

Rodgers, S.D., Camphausen, R.T., Hammer, D.A., 2000. Sialyl LewisX-Mediated, PSGL-1-Independent Rolling Adhesion on P-selectin. Biophys J 79, 694-706.

Rognon, P., Gay, C., 2008. Soft Dynamics simulation. 1. Normal approach of two deformable particles in a viscous fluid and optimal-approach strategy. Eur Phys J E Soft Matter 27, 253-260.

Rognon, P., Gay, C., 2009. Soft Dynamics simulation. 2. Elastic spheres undergoing a T1 process in a viscous fluid. Eur Phys J E Soft Matter 30, 291-301.

Rosenbluth, M.J., Lam, W.A., Fletcher, D.A., 2006. Force Microscopy of Nonadherent Cells: A Comparison of Leukemia Cell Deformability. Biophys J 90, 2994-3003.

Schmidtke, D.W., Diamond, S.L., 2000. Direct Observation of Membrane Tethers Formed during Neutrophil Attachment to Platelets or P-Selectin under Physiological Flow. J Cell Biol 149, 719-730.

Smith, M.J., Berg, E.L., Lawrence, M.B., 1999. A Direct Comparison of Selectin-Mediated Transient, Adhesive Events Using High Temporal Resolution. Biophys J 77, 3371-3383.

St. Hill, C.A., Alexander, S.R., Walcheck, B., 2003. Indirect capture augments leukocyte accumulation on P-selectin in flowing whole blood. J Leukocyte Biol 73, 464-471.

Subramaniam, D.R., Gee, D.J., King, M.R., 2012. Deformable cell-cell and cell-substrate interactions in semi-infinite domain. Submitted.

Sugiyama, K., Sbragaglia, M., 2008. Linear shear flow past a hemispherical droplet adhering to a solid surface. J Eng Math 62, 35-50.

Tözeren, A., Ley, K., 1992. How do selectins mediate leukocyte rolling in venules? Biophys J 63, 700-709.

Tran-Cong, T., Phan-Thien, N., 1986. Boundary element solution for half-space elasticity or stokes problem with a no-slip boundary. Comput Mech 1, 259-268.

Villaggio, P., 1996. The Rebound of an Elastic Sphere Against a Rigid Wall. J Appl Mech-T ASME 63, 259-263.

Wankhede, S.P., Du, Z., Berg, J.M., Vaughn, M.W., Dallas, T., Cheng, K.H., Gollahon, L., 2006. Cell detachment model for an antibody-based microfluidic cancer screening system. Biotechnol Prog 22, 1426-1433.

Ward, M.D., Dembo, M., Hammer, D.A., 1994. Kinetics of cell detachment: peeling of discrete receptor clusters. Biophys J 67, 2522-2534.

Yago, T., Leppänen, A., Qiu, H., Marcus, W.D., Nollert, M.U., Zhu, C., Cummings, R.D., McEver, R.P., 2002. Distinct molecular and cellular contributions to stabilizing selectin-mediated rolling under flow. J Cell Biol 158, 787-799.

Appendix A: Half Space Green's Functions

A. NO SLIP BOUNDARY CONDITIONS

STOKESLET:

$$G_{ij}(\boldsymbol{x},\boldsymbol{X}) = G_{ij}(\boldsymbol{x},\boldsymbol{X}) - G^{*}_{ij}(\boldsymbol{x},\boldsymbol{X}) + G^{E}_{ij}(\boldsymbol{x},\boldsymbol{X})$$

Where

$$G_{ij}(\boldsymbol{x},\boldsymbol{X}) = \frac{1}{8\pi}\left(\frac{\delta_{ij}}{r} + \frac{r_i r_j}{r^3}\right)$$

$$G^{*}_{ij}(\boldsymbol{x},\boldsymbol{X}) = \frac{1}{8\pi}\left(\frac{\delta_{ij}}{R} + \frac{R_i R_j}{R^3}\right)$$

$$G^{E}_{ij}(\boldsymbol{x},\boldsymbol{X}) = \frac{2X_3}{R^3}\left[\delta_{j3}R_i + \delta_{i3}R_j - 2\delta_{i3}\delta_{j3}R_3 + x_3\left\{2\delta_{i3}\delta_{j3} - \delta_{ij} + \frac{3R_i}{R^2}\left(R_j - 2\delta_{j3}R_3\right)\right\}\right]$$

ASSOCIATED STRESS TENSOR:

$$\Sigma_{ijk}(\boldsymbol{x},\boldsymbol{X}) = \Sigma_{ijk}(\boldsymbol{x},\boldsymbol{X}) - \Sigma^{*}_{ijk}(\boldsymbol{x},\boldsymbol{X}) + \Sigma^{E}_{ijk}(\boldsymbol{x},\boldsymbol{X})$$

Where

$$\Sigma_{ijk}(\boldsymbol{x},\boldsymbol{X}) = -\frac{3r_i r_j r_k}{4\pi r^5}$$

$$\Sigma^{*}_{ijk}(\boldsymbol{x},\boldsymbol{X}) = -\frac{3R_i R_j R_k}{4\pi R^5}$$

$$\Sigma^{E}_{ijk}(\boldsymbol{x},\boldsymbol{X}) = \frac{3X_3}{2\pi R^5}\{-\delta_{j3}R_i R_k + R_3\delta_{ik}\left(2\delta_{j3}R_3 - R_j\right) + x_3[\delta_{ij}R_k + \delta_{jk}R_i - 2\delta_{j3}\left(\delta_{i3}R_k + \delta_{k3}R_i\right) + \left(\frac{5R_iR_k}{R^2} - \delta_{ik}\right)\left(2\delta_{j3}R_3 - R_j\right)]\}$$

B. NO DISPLACEMENT BOUNDARY CONDITIONS

KELVINLET:

$$G_{ij}(\boldsymbol{x},\boldsymbol{X}) = G_{ij}(\boldsymbol{x},\boldsymbol{X}) - G^{*}_{ij}(\boldsymbol{x},\boldsymbol{X}) + G^{E}_{ij}(\boldsymbol{x},\boldsymbol{X})$$

Where

$$G_{ij}(\boldsymbol{x},\boldsymbol{X}) = \frac{1}{16\pi\eta(1-\nu)}\left\{\left(3-4\nu\right)\frac{\delta_{ij}}{r} + \frac{r_i r_j}{r^3}\right\}$$

$$G^{*}_{ij}(\boldsymbol{x},\boldsymbol{X}) = \frac{1}{16\pi\eta(1-\nu)}\left\{\left(3-4\nu\right)\frac{\delta_{ij}}{R} + \frac{R_i R_j}{R^3}\right\}$$

$$G^{E}_{ij}(\boldsymbol{x},\boldsymbol{X}) = \frac{2X_3}{16\pi\eta(1-\nu)R^3}\left[\delta_{j3}R_i + \delta_{i3}R_j - 2\delta_{i3}\delta_{j3}R_3 + \frac{\boldsymbol{x}_3}{(3-4\nu)}\left\{2\delta_{i3}\delta_{j3} - \delta_{ij} + \frac{3R_i}{R^2}\left(R_j - 2\delta_{j3}R_3\right)\right\}\right]$$

ASSOCIATED STRESS TENSOR:

$$\Sigma_{ijk}(\boldsymbol{x},\boldsymbol{X}) = \Sigma_{ijk}(\boldsymbol{x},\boldsymbol{X}) - \Sigma^{*}_{ijk}(\boldsymbol{x},\boldsymbol{X}) + \Sigma^{E}_{ijk}(\boldsymbol{x},\boldsymbol{X})$$

Where

$$\Sigma_{ijk}(\boldsymbol{x},\boldsymbol{X}) = -\frac{1}{8\pi(1-\nu)r^3}\left[\left(1-2\nu\right)\left(\delta_{ij}r_k + \delta_{jk}r_i - \delta_{ik}r_j\right) + \frac{3r_i r_j r_k}{r^2}\right]$$

$$\Sigma^{*}_{ijk}(\boldsymbol{x},\boldsymbol{X}) = -\frac{1}{8\pi(1-\nu)R^3}\left[(1-2\nu)\left(\delta_{ij}R_k + \delta_{jk}R_i - \delta_{ik}R_j\right) + \frac{3R_iR_jR_k}{R^2}\right]$$

$$\Sigma^{E}_{ijk}(\boldsymbol{x},\boldsymbol{X}) = \frac{X_3}{4\pi(1-\nu)R^3}\{\left(\frac{1-2\nu}{3-4\nu}\right)[3\delta_{j3}\delta_{ik} + \delta_{i3}\delta_{jk} + \delta_{k3}\delta_{ij} - 4\delta_{i3}\delta_{j3}\delta_{k3} + \frac{3}{R^2}(\delta_{i3}R_k + \delta_{k3}R_i)(2\delta_{j3}R_3 - R_j)]$$
$$-3\delta_{j3}\frac{R_iR_k}{R^2} + \frac{6\nu R_3\delta_{ik}}{(3-4\nu)R^2}\left(2\delta_{j3}R_3 - R_j\right) + \frac{3x_3}{(3-4\nu)R^2}[\delta_{ij}R_k + \delta_{jk}R_i - 2\delta_{j3}\left(\delta_{i3}R_k + \delta_{k3}R_i\right)$$
$$+\left(\frac{5R_iR_k}{R^2} - \delta_{ik}\right)\left(2\delta_{j3}R_3 - R_j\right)]\}$$

The vectors $\boldsymbol{r}$ and $\boldsymbol{R}$ are defined as $\boldsymbol{r} = \boldsymbol{x} - \boldsymbol{X}$ and $\boldsymbol{R} = \boldsymbol{x} - \boldsymbol{X}^*$ where $\boldsymbol{x}$ – integration variable of particle surface, $\boldsymbol{X}$ - source point, $\boldsymbol{X}^*$ - image source point, $r = |\boldsymbol{r}|$, $R = |\boldsymbol{R}|$ and δ_{ij} - Kronecker delta (Fig. 2.2).

Appendix B: Supplementary Trembling Results

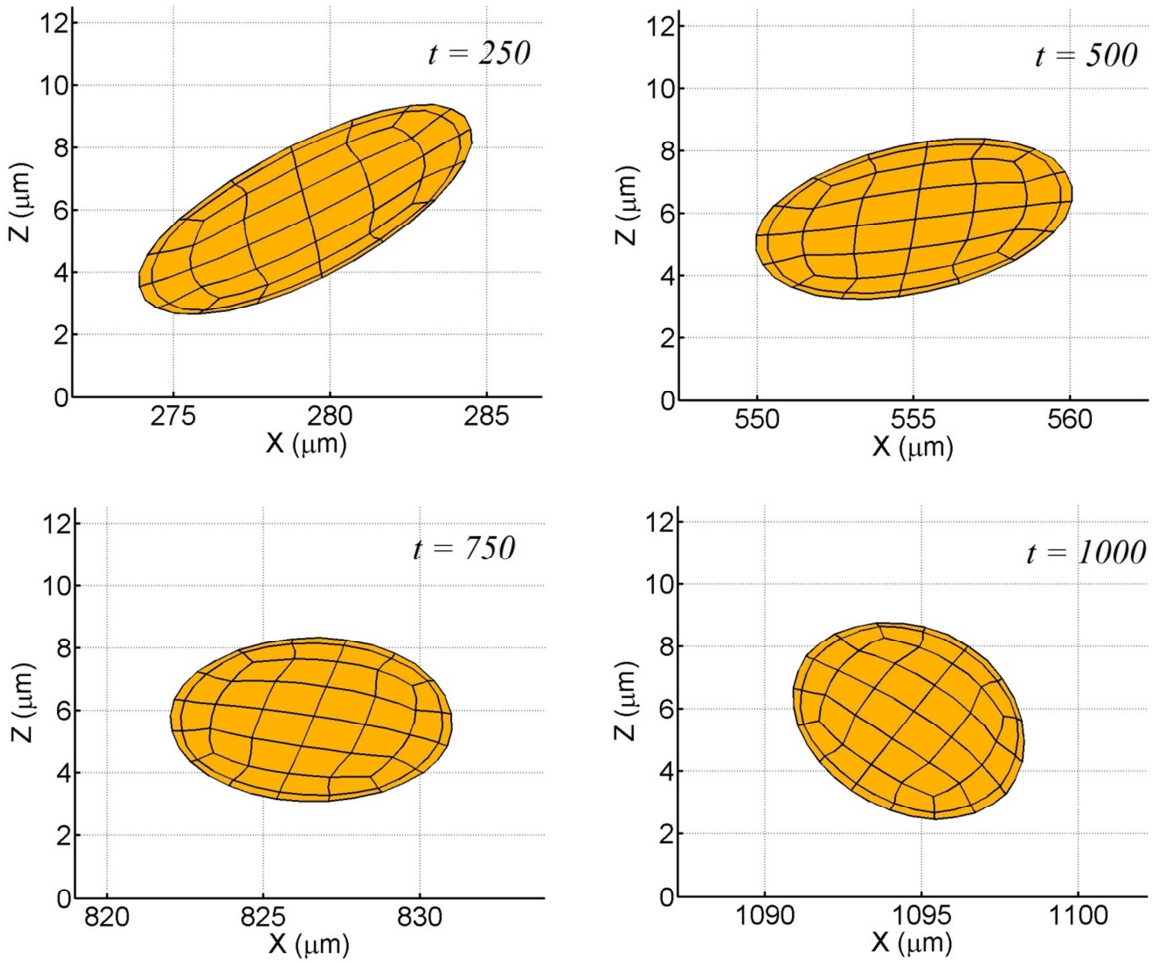

Fig. B-1 Tumbling sequence of a deformable oblate spheroid in the proximity of a rigid wall (a = 5 μm, η = 1 Pa, ν = 0.33, $\alpha = \pi/2$, κ = 0.5, $\dot{\gamma}$ = 200 s^{-1}).

…..contd

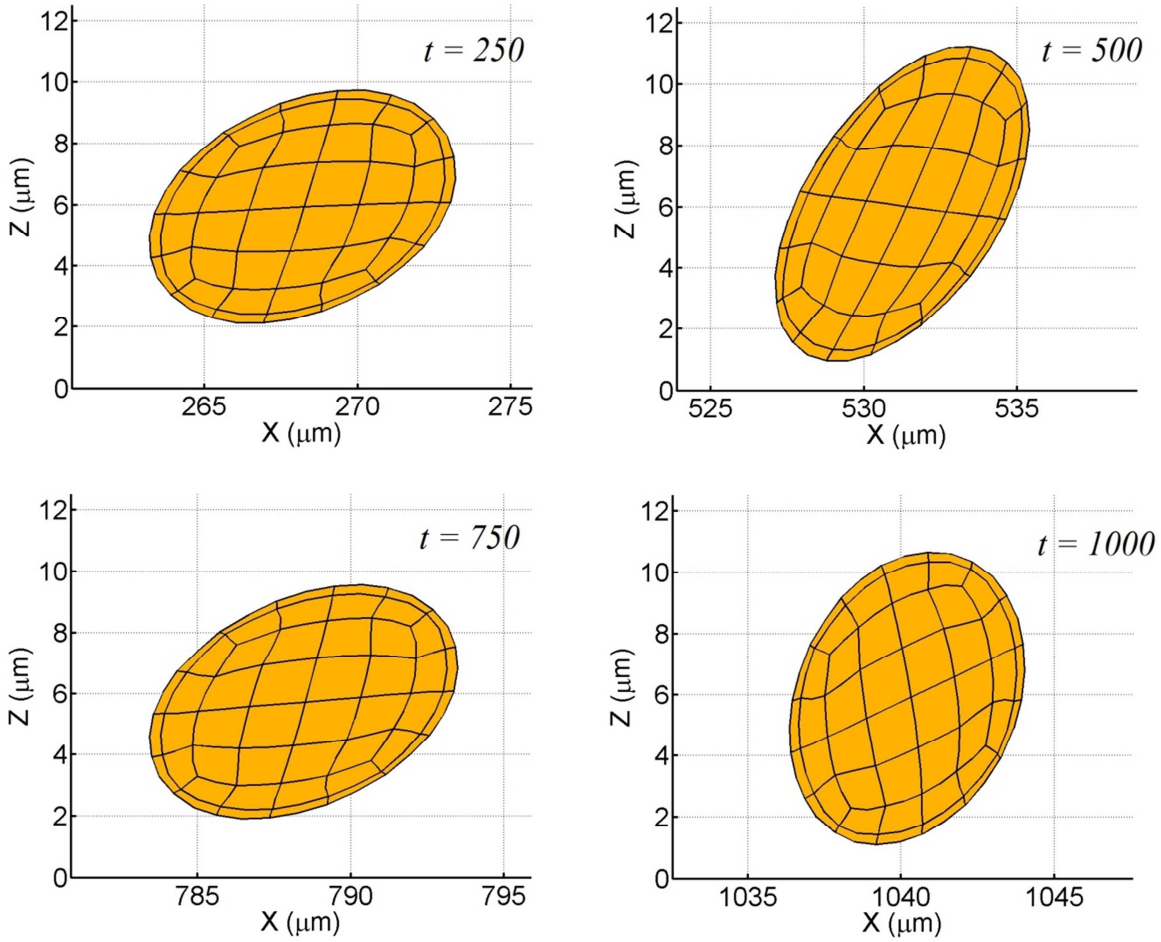

Fig. B-2 Trembling sequence of a deformable oblate spheroid in the proximity of a rigid wall (a = 5 μm, η = 1 Pa, ν = 0.33, $\alpha = \pi/2$, κ = 0.75, $\dot{\gamma}$ = 200 s^{-1}).

Appendix C: Binary Collisions Front Views

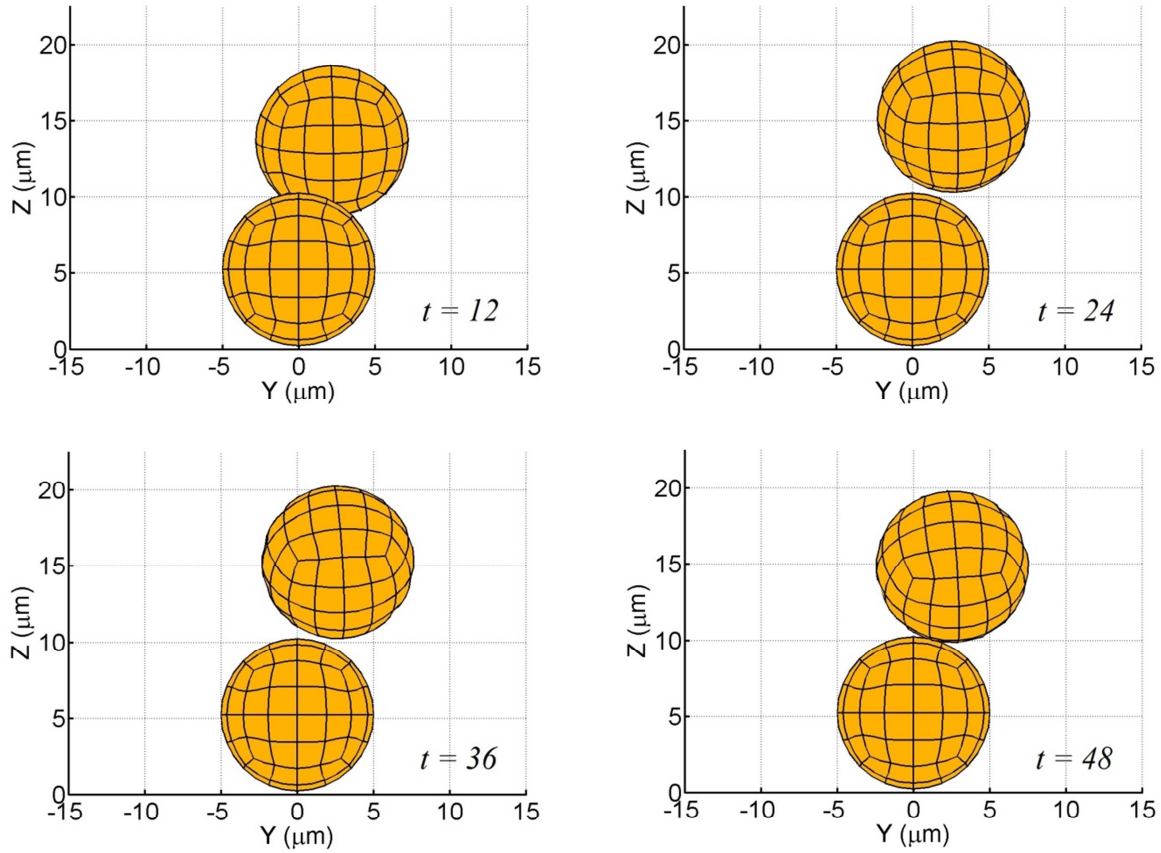

Fig. C-1 Binary interactions between a firmly adherent, spherical cell and a spherical free-stream cell (δx = -9 μm, δy = 2 μm, δz = 7.75 μm, a = 5 μm, $\dot{\gamma}$ = 100 s^{-1}).

…..contd

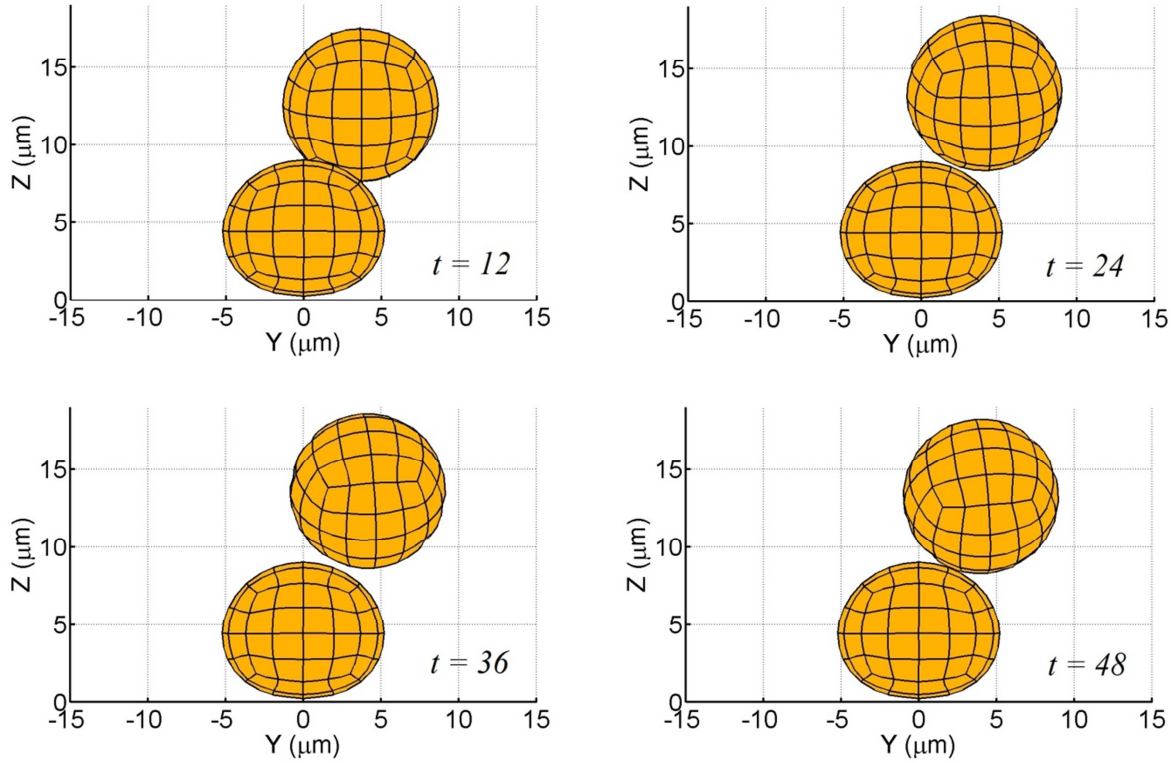

Fig. C-2 Binary interactions between a firmly adherent, moderately deformed cell and a spherical free-stream cell (δx = -9 μm, δy = 3.5 μm, δz = 7.75 μm, a = 5 μm, $\dot{\gamma}$ = 100 s^{-1}).

…..contd

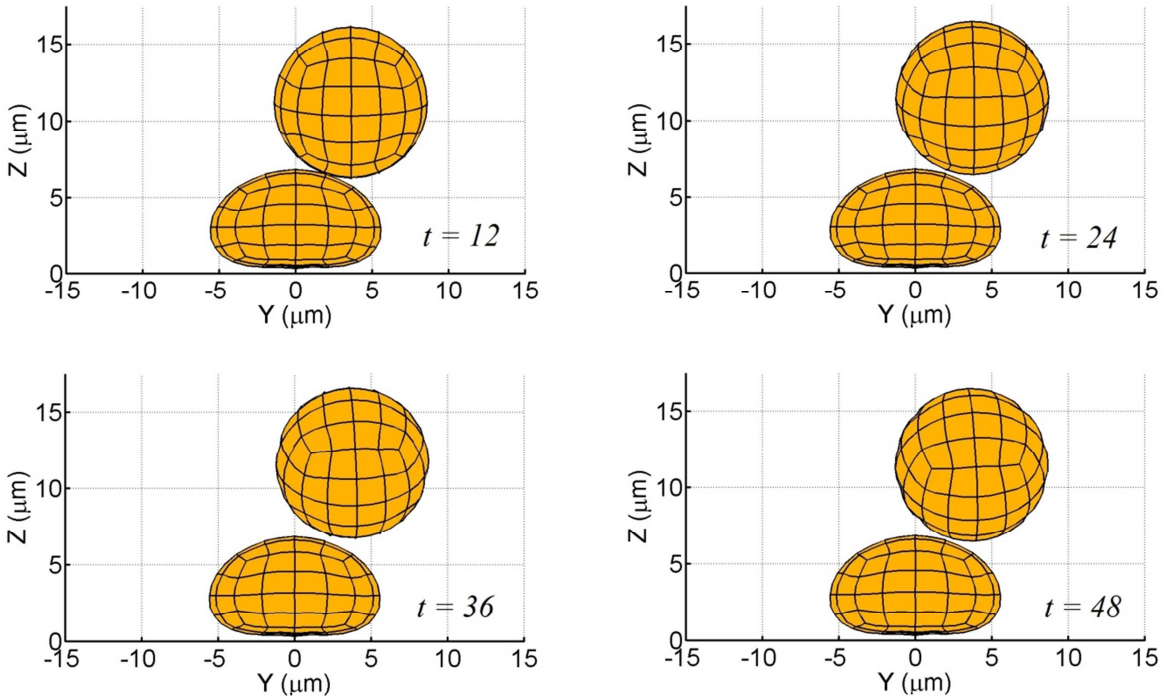

Fig. C-3 Binary interactions between a firmly adherent, highly deformed cell and a spherical free-stream cell (δx = -9 μm, δy = 3.5 μm, δz = 7.75 μm, a = 5 μm, $\dot{\gamma}$ = 100 s^{-1}).